The Physics of Fracture in an Unstable Polymeric Liquid

Okpeafoh Stephen Agimelen

School of Physics and Astronomy

University of Leeds

Submitted in accordance with the requirements for the degree of

Doctor of Philosophy

January 2013

The candidate confirms that the work submitted is his own, except where work which has formed part of jointly authored publications has been included. The contribution of the candidate and the other authors to this work has been explicitly indicated below. The candidate confirms that appropriate credit has been given within the thesis where reference has been made to the work of others.

Some of the data and discussions in Chapters 6 and 7 are contained in the jointly authored article with my PhD supervisor Professor Peter Olmsted. The article titled 'Apparent Fracture in Polymeric Fluids under Step Shear' which has been submitted to the physics archives arXiv:1204.4169v2 is currently under review.

Acknowledgements

The work presented here falls under Work Package 1 (WP1) 'Testing assumptions of the fundamental model' and Work Package 2 (WP2) 'Linear and branched polymers in strong flows' of the DYNACOP (Dynamics of Architecturally Complex Polymers) project. The author is highly indebted to Professor Tom McLeish who initiated the DYNACOP project. The author also wishes to thank Professor Peter Olmsted and Dr Daniel Read who are the principal investigators of this project in Leeds for the opportunity to participate in it. The DYNACOP project would not have been possible without the generous funding from the European Commission. The DYNACOP project falls under the Marie Curie Initial Training Network (ITN) in the Seventh Framework (FP7) program of the European Commission with grant agreement 214627. The author wishes to thank especially Professor Peter Olmsted who was the advisor for this work. The work would not have been completed without his invaluable insights. The author also wishes to acknowledge useful discussions with Scott Milner, Suzanne Fielding and Robyn Moorcroft.

Abstract

Entangled polymer solutions and melts show a variety of behaviours under different flow conditions. Recent step strain experiments [Macromolecules 42, 6261 (2009)] demonstrated a fracture-like behaviour that was interpreted in terms of a massive loss of entanglements after yielding. This was taken to violate the Doi-Edwards tube model [The Theory of Polymer Dynamics (Oxford University Press, New York, United States, 1986)]. Here this phenomenon is investigated using the Rolie-Poly model, which approximates a successful version of the DE theory. The results give close quantitative agreement with the experiments, as well as with the proposal by Marrucci and Grizzuti in 1983 that entangled polymer liquids possess an elastic instability. The 'fracture' is a transient manifestation of this elastic instability that relies on the amplification of spatially inhomogeneous fluctuations. Linear stability analysis of the fluid shows that there is also a viscous contribution to this instability so that this fracture-like behaviour is possible before the elastic limit is reached.

Contents

1 Motivation and Objective **13**

1.1 Motivation 13

1.2 Objective 13

1.3 Remarks 14

2 Theoretical Background **16**

2.1 The Stress Tensor 16

2.2 Shear Deformation 18

2.3 Steady Shear and Step Shear 20

2.4 Viscoelastic Models 21

2.4.1 Maxwell Model 22

2.4.2 Tube model and Reptation 24

2.4.3 Doi Edwards (DE) Theory 25

2.5 Instability in Polymeric Fluids 28

2.5.1 Spinodal Decomposition 29

2.5.2 Elastic Instability 30

2.5.3 Viscous Instability 32

2.6 GLaMM Model 34

2.7 Remarks 35

3 Experimental Background **36**

3.1 Rheometers 36

3.2 Step Strains with no Slip Hydrodynamic Boundary Condition (HBC) . 38

3.2.1 Experiment I: 'Fracture' at Room Temperature 39
3.2.2 Experiment II: 'Fracture' at High Temperature 41
3.3 Remarks 42

4 Theoretical Model **43**
4.1 Flow Field 43
4.2 The Rolie-Poly (RP) Model 44
4.3 Stress Diffusivity 48
4.4 Coupled System of Equations in Different Geometries 49
4.4.1 Flat Plates 49
4.4.2 Concentric Cylinders 53
4.5 Effects of Stress Diffusivity 61
4.6 Remarks 63

5 Numerical Scheme **65**
5.1 Steady State Solutions 65
5.1.1 Newton algorithm 66
5.2 Dynamics For a Spatially Homogeneous System 69
5.2.1 4th Order Runge-Kutta Scheme (RK4) 69
5.3 Spatially Inhomogeneous System 71
5.3.1 Backward Implicit Scheme (BIS) 71
5.3.2 Calculating Stress Using BIS 73
5.3.3 Calculating the Velocity Field Using BIS 75
5.4 Choice of Parameters 77
5.5 Test For Convergence 78
5.6 Remarks 82

6 Modelling Fracture **83**
6.1 Case I: Intermediate Shear Rate, High Strain 86
6.2 Case II: High Shear Rate, Low Strain 93
6.3 Case III: Low Shear Rate, Low Strain: 95

6.4 Characterisation of Fracture 96
6.4.1 CCR, Strain and Number of Entanglements per Chain 98
6.4.2 Fracture Width 100
6.4.3 Type C Behaviour 100
6.4.4 Induction Time 101
6.5 Curvature Effects 107
6.6 Remarks 108

7 Analysis of Perturbations **110**
7.1 I: Perturbing Each Quantity Separately 111
7.2 II: Perturbing All Quantities Simultaneously 114
7.3 Instability 115
7.4 Elastic Instability 116
7.4.1 Deformed Chains 120
7.4.2 Validity of the Relaxation Function 121
7.5 Linear Stability Analysis 124
7.5.1 Linearized Equations 125
7.5.2 Dispersion Relation 133
7.6 Spinodal 135
7.7 Viscous contribution to instability 136
7.8 Eigenvectors 138
7.9 Growth of Perturbations 139
7.10 Mechanism of Fracture 142
7.10.1 Elastic Contribution 142
7.10.2 Viscous Contribution 144
7.11 Remarks 145

8 Discussions **147**
8.1 Summary of Key Findings 147
8.2 Further Considerations 149
8.2.1 Stress Maximum? 149

8.2.2 Hydrodynamic Boundary Condition (HBC) 152
8.2.3 State of Chain Entanglement 156
8.2.4 Non Bonded Interactions 157
8.3 Approximations/Assumptions 158

References **166**

List of Tables

6.1 Data for variable Z 103

7.1 Components of most unstable eigenvector. 139

List of Figures

2.1 Pictorial representation of the stress tensor. 17

2.2 Schematic representation of the parallel plate configuration. 19

2.3 Responses of different kinds of liquids to step strain. 20

2.4 Storage and Loss moduli for the simple Maxwellian fluid. 24

2.5 Tube picture. 24

2.6 Stress maximum. 26

2.7 Tube dynamics in step strain. 27

2.8 Damping functions. 28

2.9 Spinodal decomposition. 30

2.10 Nonlinear relaxation modulus for different strains. 31

2.11 Nonmonotonic constitutive relation and shear banding. 32

2.12 Shear banding velocity profiles. 33

2.13 Constraint release event. 35

3.1 Parallel plate rheometer. 37

3.2 Concentric cylindrical Couette Cell. 38

3.3 Shear stress and velocity profiles from [4]. 39

3.4 Shear stress and particle displacements from [40]. 41

4.1 Tube conformation and stress. 45

4.2 Cylindrical coordinate system. 54

4.3 Plateau stress selection by stress diffusivity. 62

5.1 Steady state constitutive curves for the RP model. 68

5.2 Flow curve for the DRP model. 76

5.3 Shear stress during startup and relaxation for 600 grid points. 79
5.4 Velocity profiles for 600 grid points. 80
5.5 Same as Figures 5.3 with 800 grid points 80
5.6 Same as Figures 5.3 with 1000 grid points 81
5.7 Convergence of calculations with decreasing time steps. 81

6.1 Calculated shear stress and other quantities. 84
6.2 Calculated velocity profiles and other quantities. 87
6.3 Particle displacements for SBR250K from [4]. 88
6.4 Shear rate and strain during 'fracture'. 88
6.5 Chain stretch and orientation during 'fracture'. 89
6.6 Calculated and experimentally measured [4] shear stresses. 90
6.7 Shear stress and other quantities during 'fracture'. 91
6.8 Calculated and experimentally measured [4] shear stresses for Case II. . 94
6.9 Calculated and experimentally measured [4] velocity profiles for Case II. 94
6.10 Calculated and experimentally measured [4] shear stresses for Case III. 96
6.11 Calculated and experimentally measured [4] velocity profiles for Case III. 97
6.12 Parameter values for 'fracture'. 99
6.13 'Fracture width'. 100
6.14 Calculated and experimentally measured relaxation moduli. 101
6.15 Variation of 'induction time' with Z. 102
6.16 Variation of 'induction time' with strain. 103
6.17 Shear rate profile after stretch relaxation. 104
6.18 Overshoot strains at different shear rates. 105
6.19 Variation of 'induction time' with shear rate. 106
6.20 'Fracture' with curved plates. 107

7.1 Perturbing Δ_{xx} 112
7.2 Perturbing Δ_{yy} 113
7.3 Perturbing Δ_{xy} 114
7.4 Perturbing $\hat{\dot{\gamma}}$ 115

7.5 Perturbing all quantities simultaneously. 116
7.6 Free energy and its curvature. 117
7.7 Parameters for 'fracture'. 119
7.8 Approximate representation of entangled chains by an ellipsoidal blob. . 121
7.9 Relaxation function and strain. 122
7.10 Relaxation function and modulus. 122
7.11 Spatial profiles of Relaxation function. 123
7.12 Profiles of strain and velocity during 'fracture'. 123
7.13 Eigenvalues at different shear rates. 134
7.14 ω_{max} with strains 135
7.15 Spinodal and other quantities. 136
7.16 Shear stress and eigenvalues. 137
7.17 Strain, effective curvature and eigenvalues. 138
7.18 Growth of perturbations. 140
7.19 Spatial profiles of the stress components. 140
7.20 Shear stress evolution for different scales of perturbation. 141
7.21 Same as Figure 7.19 for $\nu = 0.005$. 141
7.22 Same as Figure 7.19 for different values of Z. 141
7.23 Stress relaxation after step shear for different values of Z. 142

8.1 Different behaviours of stress plateau. 151
8.2 Delayed slip in polystyrene. 154
8.3 Similar to Figure 8.2 for $\gamma = 2$. 154
8.4 Similar to Figure 8.2 for $\gamma = 5$. 155

Chapter 1

Motivation and Objective

1.1 Motivation

In a series of experiments, Wang and his co workers reported [1, 2, 3, 4] some unexpected relaxation behaviours of polybutadiene solutions and melts. In the experiments, the materials were subjected to strong flows, and the movement of the fluid particles were tracked using particle tracking techniques. Surprisingly, the fluid seemed to have undergone a fracture with particles distributed on both sides of a so-called failure plane. The 'failure plane' was located in the bulk of the fluid, but not necessarily at the same position in different runs of the experiment. This observation is quite strange, and for this reason it became necessary to get some understanding of the possible cause of this unusual event.

1.2 Objective

In a polymeric liquid of sufficient concentration the long molecules (referred to as polymer chains or simply chains) of the polymer adopt a conformation such that the lateral motion of a chain is strongly inhibited by its neighbouring chains. While this random conformation maximizes entropy, it leads to a situation whereby the chains

appear to be confined to some imaginary tube-like regions (the tube model). The tube represents the constraints imposed on the motion of a chain by its neighbours. In this entangled state the tubes form a network, which is deformed when the fluid is made to flow.

The most successful theory for polymeric liquids, namely the Doi-Edwards (DE) theory [5], predicts that the fluid could become unstable when subjected to strong shearing forces. Although there has been no direct observation of this instability in experiments, its signatures have been observed. Notable among them is the phenomenon of shear banding, a situation whereby the fluid suddenly separates into regions flowing at different viscosities.

Recently, Wang and his coworkers [4] reported a fracture like behaviour in concentrated solutions of styrene butadiene (SBR) when subjected to strong flows. They interpreted this to mean a complete breakdown of the entanglement network and that this was a violation of the tube model, and they posited that a new theoretical model would be required to explain this behaviour.

This then raises the question **do we need a new theoretical model to explain this phenomenon?** One objective of this project is to check if the tube model (both the original tube model and its variants) is capable of capturing this behaviour. If this is possible, then the second objective will be to examine the underlying physics of this strange behaviour.

1.3 Remarks

The brief description given here serves to give the reader the objective for the calculations presented in the remaining parts of this thesis. The treatise shall proceed in Chapter 2 with a review of the basic theoretical concepts involved in the study of polymeric liquids. Chapter 3 will give more detailed description of the experiments that motivated the calculations to be presented in subsequent Chapters.

The theoretical model employed in the calculations shall be described in Chapter 4. Which will then be followed in Chapter 5 by a description of the numerical schemes used in the calculations. Modelling of this fracture-like phenomenon as seen in the experiments will be given in Chapter 6, and a comparison of the calculations with experimental data shall be given as well. In Chapter 7, there will be a more general analysis of the perturbations leading to this 'fracture' phenomenon. The thesis will finally conclude in Chapter 8 with a discussion of results from the calculations and suggestions for future work.

Chapter 2

Theoretical Background

The objectives and motivation for this work were stated in the previous chapter, however to make the discussion clearer, it will be necessary to give a brief overview of relevant theories for this work. It begins with the a description of the state of stress in a fluid and then some theories that describe the stress tensor.

2.1 The Stress Tensor

The theories that shall be applied in this study are those that are based on the continuum hypothesis [6] in which properties of the fluid are assumed to vary smoothly over a small volume of the fluid but large enough as to capture the macroscopic properties of the fluid. This small volume of fluid is called a fluid element. A fluid element is a small volume of fluid that contains sufficient molecules such that the average values of fluid properties in this volume are not affected by variations due to molecular fluctuations. This approach is sufficient since the properties of interest here occur on a macroscopic scale much larger than the distance between molecules. The forces acting on a fluid consist of the long-range body forces (notably gravity or electromagnetic force for a fluid with charged particles) and surface forces. The surface forces are short ranged, and they decrease rapidly as distance

between molecules increase. The short-range forces only become important when there is direct mechanical contact (as much as their repulsive forces will allow) between fluid elements. The surface forces are described by the stress tensor.

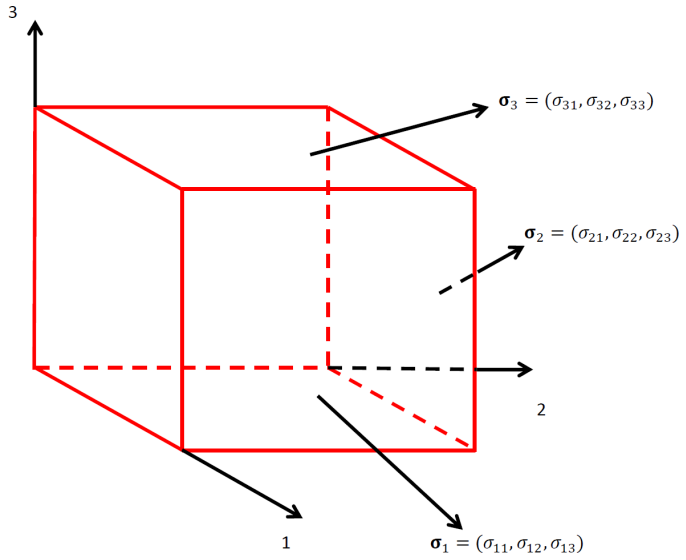

Figure 2.1: Pictorial representation of the stress tensor.

The stress tensor contains information on the force per unit area that material exterior to a fluid element exerts on it. The stress tensor is a second order tensor that can be represented in matrix form as

$$\boldsymbol{\sigma} = \begin{pmatrix} \sigma_{11} & \sigma_{12} & \sigma_{13} \\ \sigma_{21} & \sigma_{22} & \sigma_{23} \\ \sigma_{31} & \sigma_{32} & \sigma_{33} \end{pmatrix}. \tag{2.1}$$

Consider the cubic fluid element shown in Figure 2.1. The force per unit area $\boldsymbol{\sigma}$ on each of the surfaces of the fluid element is represented by the stress tensor, which can be put in matrix form as in Equation (2.1). The force per unit area acting on a surface perpendicular to an arbitrary unit vector $\hat{\mathbf{n}}$ is given as [7]

$$\sigma_j = \hat{n}_i \sigma_{ij}. \tag{2.2}$$

Equation (2.2) implies that the force $\boldsymbol{\sigma}_1$ acting on the surface perpendicular to the unit vector $\hat{\mathbf{n}}_1 = (1, 0, 0)$ is given as $\boldsymbol{\sigma}_1 = (\sigma_{11}, \sigma_{12}, \sigma_{13})$. Similarly, the forces $\boldsymbol{\sigma}_2$ and $\boldsymbol{\sigma}_3$ acting on the surfaces perpendicular to the unit vectors $\hat{\mathbf{n}}_2 = (0, 1, 0)$ and $\hat{\mathbf{n}}_1 = (0, 0, 1)$ are given as $\boldsymbol{\sigma}_2 = (\sigma_{21}, \sigma_{22}, \sigma_{23})$ and $\boldsymbol{\sigma}_3 = (\sigma_{31}, \sigma_{32}, \sigma_{33})$ respectively. This implies that the ith row of the stress tensor $\boldsymbol{\sigma}$ is the force per unit area that material exterior to the fluid element exert on a surface perpendicular to the ith coordinate axis. This concept is illustrated in Figure 2.1.

While the rows describe the orientations of the surfaces on which the forces act, the columns give the components of the forces on these surfaces. Hence, the component σ_{11} is the force per unit area in the direction 1 on the surface perpendicular to direction 1. Similarly, the component σ_{12} is the force per unit area in the direction 2 on the surface perpendicular to direction 1 and σ_{13} is the force per unit area in the direction 3 on the surface perpendicular to direction 1. The components $\sigma_{ij}, i \neq j$ are referred to as shear components or shear stresses while the components $\sigma_{ij}, i = j$ are referred to as the normal components or normal stresses. When the flow is in direction 1, then the quantity $\sigma_{11} - \sigma_{22}$ is known as the first normal stress difference, while the quantity $\sigma_{22} - \sigma_{33}$ is the second normal stress difference. The total stress $\mathbf{T}$ is decomposed into an isotropic stress $-p\boldsymbol{\delta}$ and a deviatoric stress $\boldsymbol{\sigma}$ as

$$\mathbf{T} = \boldsymbol{\sigma} - p\boldsymbol{\delta}, \tag{2.3}$$

where the isotropic pressure p maintains incompressibility.

2.2 Shear Deformation

The phenomena of interest in this study arise during shear deformation of polymeric fluids. In this type of deformation, the fluid is placed between two plates and one or both plates is moved at some velocity while the fluid response is observed.

Different kinds of plate configurations exist depending on the nature of the fluid and the material property of interest. Each of these configurations is referred to as a rheometer and each rheometer can be operated in different modes. More details of these kinds of apparatus will be given in the next chapter.

For simplicity, consider a fluid placed between two parallel plates as depicted in Figure 2.2. The lower plate is fixed, while the upper plate is moved with a uniform velocity V. The spatially averaged shear rate $\langle\dot{\gamma}\rangle$ is given by V/H, where H is the gap between the plates. The local shear rate is a function of space y and time t. It is the spatial derivative of the fluid velocity given by

$$\dot{\gamma}(y,t) = \frac{\partial v_x(y,t)}{\partial y}, \tag{2.4}$$

where $v_x(y,t)$ is the local fluid velocity. This type of deformation leads to a strain $\gamma(y,t)$ in the fluid. The accumulated strain at every point in the fluid from a time t' to the current time t is given by

$$\gamma(t,t') = \int_{t'}^{t} \dot{\gamma}(t'')dt''. \tag{2.5}$$

This strain causes a shear stress σ_{xy} to be generated in the fluid which is related to the shear rate (or strain rate) in some way.

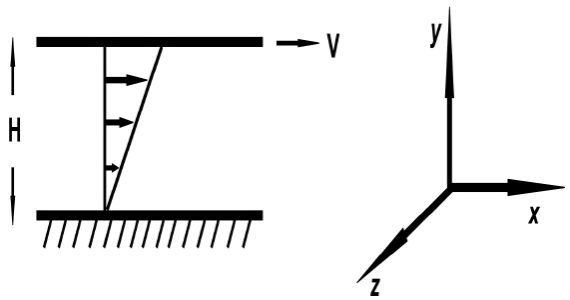

Figure 2.2: Schematic representation of the parallel plate configuration. The fluid is placed between two parallel plates and sheared in the x-direction, a velocity gradient exists in the y-direction, H is the distance between the plates.

2.3 Steady Shear and Step Shear

Under the shear deformation depicted in Figure 2.2, the moving plate could be moved at a constant velocity until a steady shear stress is reached, in which case the protocol is referred to as steady shear. Otherwise a sudden strain γ_0 could be imposed on the fluid by moving one of the plates for a duration t_0 at some rate V; the bulk fluid deforms at an average rate $\langle\dot{\gamma}\rangle$, so that $\gamma_0 = \langle\dot{\gamma}\rangle t_0$. This protocol is referred to as step strain. In the ideal case, the strain is imposed instantaneously as

$$\gamma(t) = \gamma_0 H(t), \tag{2.6}$$

where H is the Heaviside step function. The shear stress developed then decays to zero (stress relaxation) in time. In experiments however, the strain takes some finite time to reach γ_0, hence the shear stress takes some time to grow as in Figure 2.3.

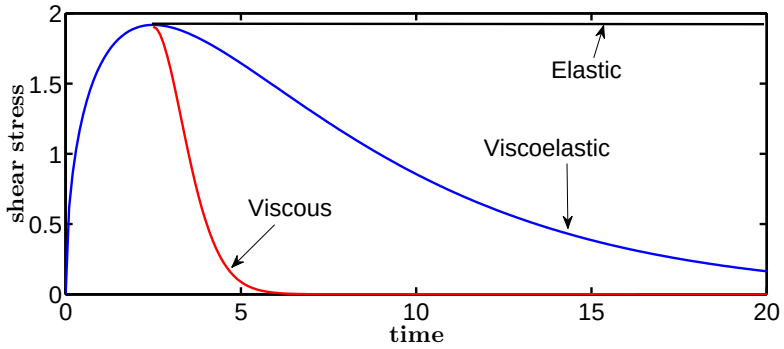

Figure 2.3: Different responses of Newtonian liquids (viscous), polymeric liquids (viscoelastic) and solids (elastic) to a step strain.

However, the response of a polymeric liquid to step strains is distinct from those of solids (elastic materials) and Newtonian liquids (viscous liquids). In a solid the stress generated will remain constant after the step strain, while in a Newtonian liquid, the stress will relax almost instantaneously. The deviation from the ideal situation of an instantaneous relaxation is just due to constraints in experiments and inertia effects. However, for a polymeric liquid, the stress will relax in a finite measurable time, known as the terminal relaxation time τ. This is illustrated in

Figure 2.3. The behaviour of polymeric liquids thus lies between those of elastic materials and viscous liquids, and it is known as **viscoelasticity**.

In Newtonian fluids, the relationship between the shear stress and the shear rate (constitutive relation) is given by the simple relation

$$\sigma_{xy} = \eta\dot{\gamma}, \tag{2.7}$$

where η is the viscosity. In this case, the fluid viscosity is constant; it is not a function of shear rate. In Newtonian fluids, the shear rate is uniform throughout the fluid; that is, the imposed shear rate is the same as the local shear rate. However, for non Newtonian fluids (otherwise referred to as complex fluids), the viscosity is not independent of shear rate. Also, when the fluid is placed between two parallel plates as depicted in Figure 2.2, the shear rate is not necessarily uniform, that is, the local shear rate is not always equal to the average shear rate. The constitutive relations for complex fluids are much more involved and depend on the fluid being described.

For non Newtonian fluids, the normal stress differences are non zero in shear flow, unlike in Newtonian fluids where the normal stress differences are exactly zero [8]. The non zero stress differences in non Newtonian fluids are responsible for a number of interesting behaviours such as the rod climbing effect [8].

2.4 Viscoelastic Models

Theoretical models that try to capture both the elastic and viscous character of polymeric fluids are known as viscoelastic models. There have been various attempts to develop viscoelastic models for polymeric liquids, both from the phenomenological and molecular points of view.

2.4.1 Maxwell Model

The first attempt to capture the viscoelastic character led to the Maxwell model [8] which treats a polymeric fluid as being made of an elastic Hookean spring in series with a dissipative viscous fluid. The Maxwell model gives a viscoelastic equation of the form

$$\sigma_{xy} + \frac{\mu}{G}\frac{\partial \sigma_{xy}}{\partial t} = \mu\dot{\gamma}, \tag{2.8}$$

where μ is the fluid viscosity and G is the modulus of elasticity. The viscoelastic character of this equation can be easily seen by considering slow and fast deformations. For slow deformations σ_{xy} dominates the left hand side of Equation (2.8), giving

$$\sigma_{xy} = \mu\dot{\gamma}, \tag{2.9}$$

which is the Newtonian constitutive Equation (2.7) with μ replacing η. For fast deformations, the term $\partial\sigma_{xy}/\partial t$ dominates the left hand side of Equation (2.8), and integrating both sides of the resulting differential equation gives

$$\sigma_{xy} = G\int_{t'}^{t} \dot{\gamma}(t'')dt'' = G\gamma(t,t'), \tag{2.10}$$

which is Hooke's law for an elastic solid.

Equation (2.8) can be easily solved by integration by parts to give

$$\sigma_{xy} = \int_{-\infty}^{t} \frac{\mu}{\tau} e^{-(t-t')/\tau}\dot{\gamma}dt', \tag{2.11}$$

where $\tau = \mu/G$ is the relaxation time. The quantity

$$G(t,t') = \frac{\mu}{\tau} e^{-(t-t')/\tau}, \tag{2.12}$$

is the relaxation modulus which keeps a memory of the deformation history of the

fluid. The modulus can be written as a complex quantity as $G^* = G' + iG''$, where G', which contains elastic information is known as the storage modulus; and G'', which contains viscuous information, is known as the loss modulus. The complex modulus can be calculated by taking a Fourier transform of $i\omega G$ as

$$G^* = \int_0^\infty i\omega G(s) e^{-i\omega s} ds, \tag{2.13}$$

where $s = t - t'$. Using Equation (2.12) gives

$$G^* = \int_0^\infty i\omega \frac{\mu}{\tau} e^{-(i\omega + 1/\tau)s} ds, \tag{2.14}$$

which gives

$$G^* = \frac{i\omega\mu}{1 + i\omega\tau} e^{-(i\omega+1/\tau)s} \Big|_0^\infty, \tag{2.15}$$

from which

$$G^* = \frac{\mu\omega^2\tau}{1 + \omega^2\tau^2} + i\frac{\mu\omega}{1 + \omega^2\tau^2}. \tag{2.16}$$

It follows that

$$G' = \frac{\mu\omega^2\tau}{1 + \omega^2\tau^2} \tag{2.17}$$

and

$$G'' = \frac{\mu\omega}{1 + \omega^2\tau^2}. \tag{2.18}$$

The storage and loss moduli for the Maxwellian fluid for $\mu = \tau = 1$ is shown in Figure 2.4. The frequency at which $G' = G''$ is known as the cross over frequency and it is equal to the inverse of the relaxation time as indicated in Figure 2.4.

Although the Maxwell model shows a single relaxation time for the fluid, a real polymer solution shows a spectrum of relaxation times which covers more decades in frequency as the molecular weight of the polymer is increased. The spectrum of relaxation times is due to different parts of the polymer relaxing at different times.

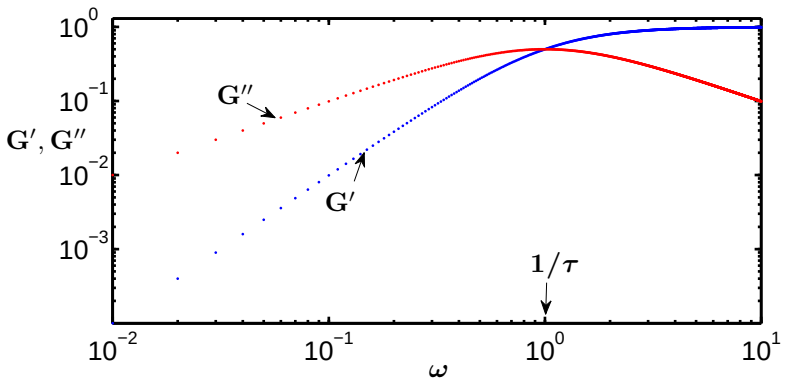

Figure 2.4: Storage and Loss moduli for the simple Maxwellian fluid, showing the crossover frequency (vertical arrow) where $G' = G''$.

At sufficient concentration and molecular weight the chains get entangled, and this entanglement also contributes to the spectrum of relaxation times.

2.4.2 Tube model and Reptation

The physics of polymers in melts is greatly simplified by the following two assumptions. The chains are ideal, which leads to a Gaussian distribution in equilibrium, and the drag on one part of a chain does not affect the drag on a remote part of the same chain. This implies that the hydrodynamic interactions are screened out [7].

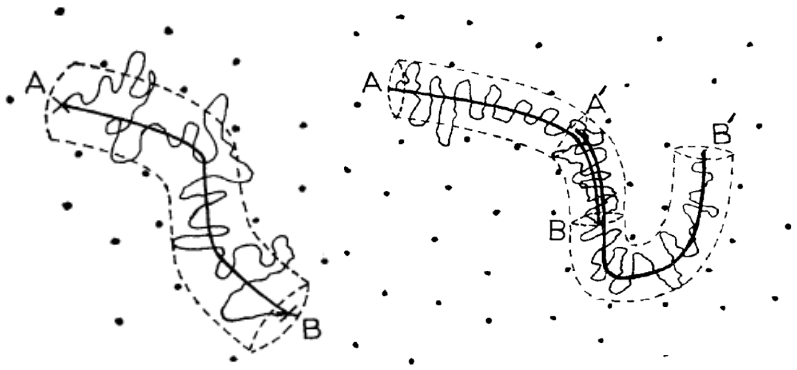

Figure 2.5: Cartoons of (left) a chain confined to a tube-like region due to constraints from other chains and (right) reptation event, Figures from [9].

Significant progress in understanding the physics of polymer chains in an entanglement network was made in 1971 by de Gennes [10] in his theory of reptation. In this formulation, the chain is trapped in the mist of fixed obstacles such as a

rubber network. The strands of rubber in the network are fixed but flexible, hence restricting the motion of the chain. The chain can only move between the strands but cannot move across them. Thus the chain diffuses back and forth along its length, and this motion is called **reptation**. As a result of the restrictions to its motion, the chain appears to be confined to tube-like regions as shown on the left of Figure 2.5.

The motion of the chain along the tube contour is known as the primitive path, and the conformation of the tube changes as the chain diffuses along its length. During reptation, when a chain AB confined in the tube shown on the right of Figure 2.5 moves to another position $A'B'$, the part of the tube AA' becomes empty and disappears, while another part of the tube BB' is formed. This new segment takes on any random conformation and becomes a constraint for the rest of the chain. Therefore the conformation of the tube is a random walk with a step length referred to as the 'tube diameter'. The molecular weight of the polymer between entanglements is called the entanglement molecular weight M_e. The time it takes for a chain to diffuse from its original tube completely is known as the terminal relaxation time or reptation time τ_d. Using scaling arguments de Gennes proposed a proportionality between the reptation time and molecular weight as $\tau_d \sim M^3$. However, experimental studies show that $\tau_d \sim M^{3.4}$ [5, 7].

While de Gennes considered the problem of a polymer chain in a fixed network, a real network of polymer chains is not fixed, as there are no chemical links between the polymer chains. Doi and Edwards extended the ideas of de Gennes to the problem of a polymer chain in a network of other polymer chains [5].

2.4.3 Doi Edwards (DE) Theory

Using the reptation model of De Gennes, Doi and Edwards [5, 9, 11, 12, 13] proposed a viscoelastic equation for polymers solutions of different concentration and

melts. For shear deformations, the equation gives the shear stress as [5]

$$\sigma_{xy} = G_0 \int_{\infty}^{t} dt' \mu(t-t') F_1(\gamma(t,t')), \tag{2.19}$$

where the dimensionless polymeric stress $F_1(\gamma)$ is given as

$$F_1(\gamma) = \frac{1}{2\gamma} \int_0^1 dx \left(1 + \frac{x^2\gamma^2 - 1}{\sqrt{x^4(\gamma^4 + 4\gamma^2) - 2\gamma^2 x^2 + 1}} \right). \tag{2.20}$$

The function $\mu(t-t')$ keeps a memory of deformation, while x is an arbitrary integration variable.

Equation (2.19) predicts a maximum in the shear stress as a function of shear rate when the shear rate exceeds the inverse reptation time as in Figure 2.6. Thus for $\dot{\gamma} > 1/\tau_d$ the condition $d\sigma_{xy}/d\dot{\gamma} < 0$ is satisfied, which implies that $dF_1/d\gamma < 0$ (since $\gamma = \dot{\gamma}t$) in this regime.

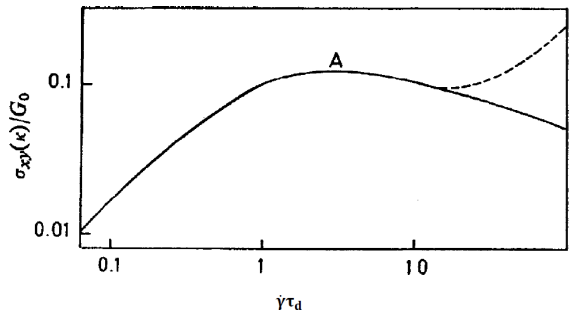

Figure 2.6: Shear stress (as a function of the shear rate) maximum predicted by the DE theory at the point A where the shear rate exceeds the inverse reptation time, from [13].

In the DE theory, the relaxation of the chain after a step strain occurs in two stages. Before the deformation, the chains are in equilibrium so that the tube conformation is random. During the deformation, the tube gets aligned in the flow direction and if the strain amplitude is large enough, the tube is also stretched. After the step strain, the tube relaxes stretch on a time scale τ_R known as the stretch relaxation time or Rouse time, and then after a time τ_d (known as the

reptation time) the chain escapes from its original tube and the tube alignment is lost. This concept is illustrated on the left of Figure 2.7. The processes of stretch relaxation and reptation are captured in the relexation modulus $G(t)$, which is the ratio of the shear stress to the applied strain as shown on the right of Figure 2.7.

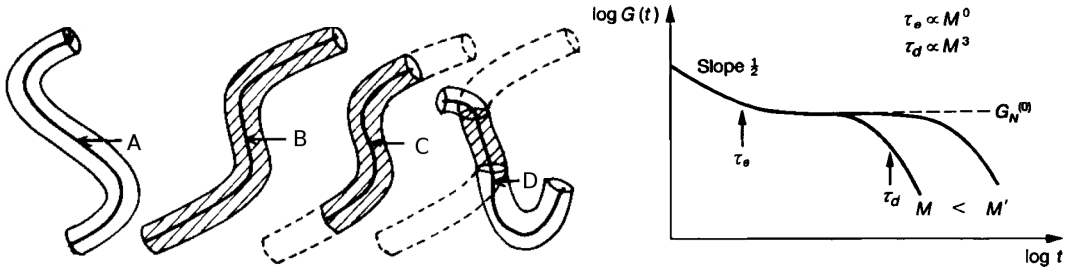

Figure 2.7: Left: Tube dynamics during stress relaxation before and after a step strain. A- isotropic conformation in equilibrium before the step strain. B- anisotropic orientation of the tube during flow. C- stretch relaxation following the step strain but still oriented anisotropically. D- tube returns to isotropic conformation as reptation sets in after stretch relaxation. Right: Relaxation modulus after a step strain, Figures from [5].

The relaxation of stretch after the step strain leads to a quick decay in the relaxation modulus, which is then followed by a very slow decay (as the chains are still trapped in their original tubes) during which the relaxation modulus forms a plateau. However, as reptation proceeds, at a time of the order of the reptation time the stress experiences a quick decay so that the material relaxes stress completely. Chain stretch becomes more significant at very fast strain rates, and this can lead to an increase in the shear stress at these strain rates as illustrated by the dashed lines in Figure 2.6. Although this mechanism for chain stretch was discussed in the DE theory, chain stretch was considered to relax too quickly for it to be of much significance and hence not included in the viscoelastic Equation (2.19). However, τ_R and τ_d are related to the number of entanglements per chain Z as $\tau_d/\tau_R = 3Z$.

In general, the relaxation modulus is both a function of time and strain, and then referred to as the nonlinear relaxation modulus $G(t, \gamma)$. Experiments [14] have shown that after stretch relaxation, the nonlinear relaxation modulus can be

separated into the linear part $G(t)$ and the strain dependent part $h(\gamma)$ as

$$G(t,\gamma) = h(\gamma)G(t). \tag{2.21}$$

The strain dependent part $h(\gamma)$ is known as the damping function, and it measures the amount of strain softening of the material, or equivalently the degree of deviation from linearity of the material.

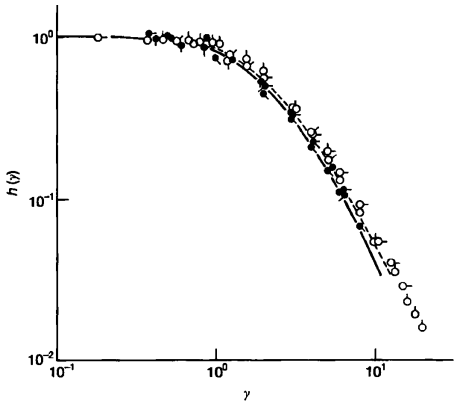

Figure 2.8: Damping functions from polystyrenes of molecular weight 8.42×10^6 (filled circles) and molecular weight 4.48×10^6 (open circles). Pip up: $0.08\,\mathrm{gcm}^{-3}$, successive $45\,^\circ$ rotations clockwise correspond to 0.07, 0.06, 0.05, 0.04, 0.03 and $0.02\,\mathrm{gcm}^{-3}$, Figure from [14].

The damping function predicted by the DE theory gave a very good match with many experimentally measured damping functions as shown in Figure 2.8. This was taken as a confirmation of success of the DE theory, and materials which showed this agreement with the DE theory were later classified as type I (or type A) materials [14, 15].

2.5 Instability in Polymeric Fluids

After the stress maximum predicted by the DE theory, the material begins to respond with a decreasing stress to continuous shearing. This situation which is a state of instability leads to the possibility that the fluid will undergo 'strain lo-

calisation'. That is, a situation whereby an initially applied strain becomes non uniformly distributed in the fluid with some regions bearing more strain than others. This instability has contributions from both elastic and viscous effects in the fluid. The elastic contribution was described by Marrucci and Grizzuti (MG) [16] in their calculation to explain the Type C 'anomaly' observed in polymeric liquids. The description of the elastic contribution given by MG bears resemblance to an instability in multicomponent systems, which leads to the phenomenon of 'spinodal decomposition' as described in the next subsection.

2.5.1 Spinodal Decomposition

In multicomponent systems such as a homogeneous composition c_0 in Figure 2.9 made from two different components, the composition c_0 which is homogeneous at temperature T_2 could phase separate into two different compositions c_1 and c_2 if the temperature of the system is suddenly dropped to T_1. This phase separation is possible because the formation of the two different compositions c_1 and c_2 is accompanied by a reduction in the free energy of the system F. What this means is that the new compositions c_1 and c_2 are more stable states of the system compared with the original composition c_0, so that this phase separation is not hindered by any thermodynamic barrier.

Once this process has started, the compositions may continue to evolve until the equilibrium compositions c_1^0 and c_2^0 are reached; this process is only limited by diffusion. This is the phenomenon of spinodal decomposition. The equilibrium composition is obtained by performing the equal tangent construction due to Gibbs [17].

The spinodal region is marked by a transition from a positive free energy curvature $d^2F/dc^2 > 0$ to a negative one $d^2F/dc^2 < 0$. Thus, the free energy curvature in the spinodal region (the area under curve C_2 in Figure 2.9) is negative, and this

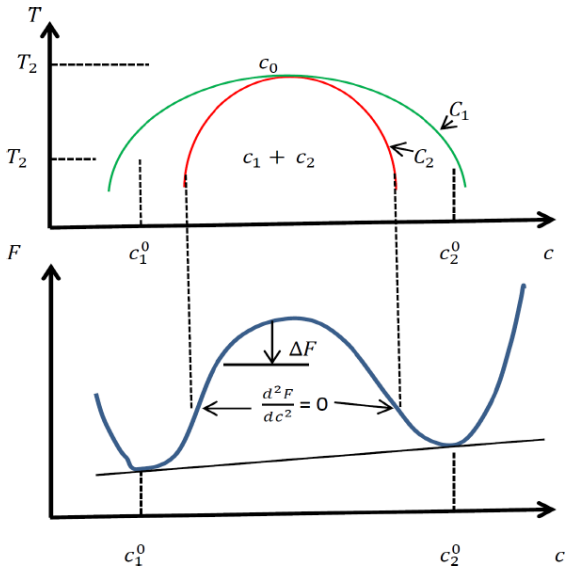

Figure 2.9: Schematic representation of the free energy profile of a multicomponent system capable of undergoing spinodal decomposition.

is the signature of linear instability in multicomponent systems. Hence, the stability of multicomponent systems can be investigated by calculating the free energy corresponding to these systems and thus the free energy curvature. In the region between curves C_1 and C_2 the free energy curvature is positive, although phase separation is still possible in this region, but it occurs by a different mechanism which will not be discussed here.

2.5.2 Elastic Instability

Marrucci and Grizzuti [16] calculated the elastic free energy consistent with the DE theory, which in shear deformations reduces to [16]

$$\mathcal{F}(\gamma) = \frac{1}{2}\int_0^1 \ln\left(\frac{1+\gamma^2\zeta^2+\left[\zeta^4(\gamma^4+4\gamma^2)-2\gamma^2\zeta^2+1\right]^{1/2}}{2}\right)d\zeta, \tag{2.22}$$

where ζ is an arbitrary integration variable and γ is the accumulated strain.

This free energy exhibits a negative curvature $d^2\mathcal{F}(\gamma)/d\gamma^2 < 0$ at certain values of γ, and this range of γ where $d^2\mathcal{F}(\gamma)/d\gamma^2 < 0$ plays the role of the spinodal

region described in the previous subsection and hence an indication of instability. Although, the initially imposed strain is homogeneous, fluctuations in the system could induce a nonuniform strain, such that the system behaves like a multicomponent system and undergoes 'phase separation'.

The free energy $\mathcal{F}$ is related to the DE constitutive equation through the function F_1 as $d\mathcal{F}(\gamma)/d\gamma = F_1(\gamma)$, so that a negative curvature of $\mathcal{F}$ implies $dF_1/d\gamma < 0$, that is, $d\sigma_{xy}/d\gamma < 0$. Hence elastic instability manifests itself during rapid startups where the applied shear rate $\dot{\gamma}$ exceeds the inverse reptation time of the fluid and the strain amplitude lies in the appropriate range [16, 18].

This leads to a much more strain softening of the nonlinear relaxation modulus than that predicted by the DE theory, a situation referred to as Type C 'anomaly' or Type C behaviour [14, 15, 16, 19], as shown in Figure 2.10

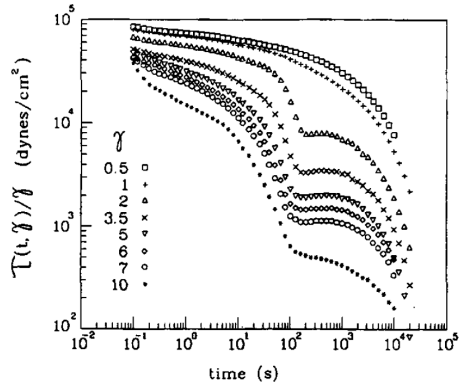

Figure 2.10: Nonlinear relaxation modulus for different strains γ showing Type C behaviour at high strains, Figure from [19].

Type C behaviour is one of the key signatures of elastic instability in polymeric liquids. It is characterised by the occurence of a 'kink' in the nonlinear relaxation modulus as shown in Figure 2.10 when the applied strain reaches a certain critical amount. It occurs in materials of sufficient molecular weight in which the number of entanglements per chain reaches a critical amount.

2.5.3 Viscous Instability

While the elastic instability manifests itself during rapid startups, the viscous instability may occur during startup or persist to steady state. It is characterised by the shear rate separating into two bands so that the fluid separates into regions flowing at different viscosities. This phenomenon is referred to as **shear banding** [20, 21, 22, 23].

Shear banding occurs when an entangled polymeric fluid with a nonmonotonic constitutive relation is sheared at high shear rates, such that the shear rate exceeds the inverse reptation time. In this regime, the total shear stress (the shear component of the total stress $\mathbf{T}$ in Equation (2.3)) satisfies $dT_{xy}/d\dot{\gamma} < 0$ as in Figure 2.11, which implies that the applied shear rate $\dot{\gamma}_2$ in Figure 2.11 is located beyond the point of stress maximum. In this case the local shear rate can undergo a 'phase separation'. This results in a coexistence of two different regions in the material where it flows at two different shear rates. This situation occurs because the constitutive relation is multivalued in this regime, such that three different shear rates correspond to the same total shear stress [22]. This is illustrated in Figure 2.11 where the three shear rates $\dot{\gamma}_1$, $\dot{\gamma}_2$ and $\dot{\gamma}_3$ all correspond to the same total shear stress T^0_{xy}. Since the shear rate $\dot{\gamma}_2$ lies in the unstable region of the constitutive relation, the fluid separates into two regions where the shear rates correspond to $\dot{\gamma}_1$ and $\dot{\gamma}_3$ which are in the stable region of the constitutive relation.

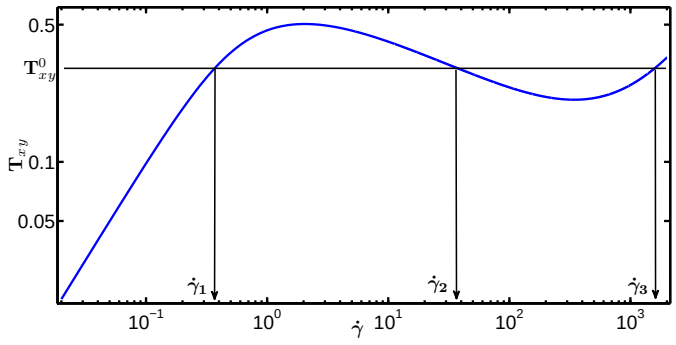

Figure 2.11: Illustration of the shear banding phenomenon for a fluid with nonmonotonic constitutive relation.

In experiments with polymer solutions, shear banding is inferred from the velocity profile of the fluid since the shear rate is related to the fluid velocity as in Equation(2.4). This has been captured in recent experiments with polymer solutions. An example is the report by Hu [24] of shear banding in an entangled polybutadiene solution of molecular weight $10^6\,\mathrm{g\,mol^{-1}}$. The measured velocity profiles of this sample at various times during shear banding are shown in Figure 2.12.

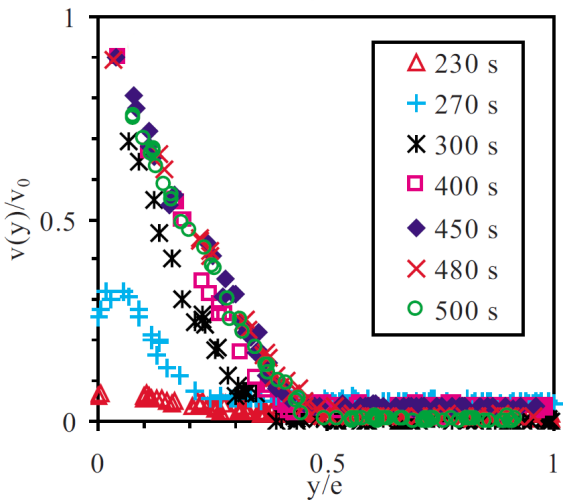

Figure 2.12: Velocity profiles during shear banding in a polybutadiene sample of molecular weight $10^6\,\mathrm{g\,mol^{-1}}$ with 64 entanglements per chain, Figure from [24].

The velocity profiles in Figure 2.12 have been scaled by the velocity of the plate v_0 and the spatial coordinate y by the gap between the plates e. The shear bands could be transient [25, 26] or persist until steady state. This shear banding phenomenon which has been captured in other experiments using micellar and polymer solutions [27, 28, 29, 30] is the key signature of viscous instability in polymeric liquids [18].

2.6 GLaMM Model

Apart from the mechanism of stretch which was neglected from the DE viscoelastic equation, another mechanism that was also discussed by DE is **constraint release**. This was considered to be insignificant and thus also neglected from the DE equation. Early experiments [31] to test the DE theory failed to capture the stress maximum predicted by the theory and this was considered to be a shortcoming of the DE theory. To remove the 'unphysical' stress maximum from subsequent tube based models, the mechanism of stretch and constraint release were included in later modifications of the DE theory [32, 33, 34], which led to viscoelastic models that could give either a monotonic or nonmonotonic constitutive relation, depending on the values of relevant parameters.

During reptation, the part of the tube previously occupied by the chain disappears while a new part is formed, as illustrated in Figure 2.5. When this occurs, the constraint that was imposed by that part of the chain on another chain is lost and the other chain gets an additional degree of freedom. This event is known as a constraint release event, this is illustrated in Figure 2.13. This constraint release event leads to a relaxation. In the linear regime (that is, applied shear rates $\dot{\gamma}$ such that $\dot{\gamma}\tau_d < 1$) it leads to a reduction of shear stress. However, in the nonlinear regime ($\dot{\gamma}\tau_d > 1$) it leads to an increase in shear stress, because the relaxed tube segment takes on a new conformation which can then be deformed by the background flow. Also, constraint release occurs due to reptation of surrounding chains in the linear regime, whereas chain retraction (reduction in chain length after stretch) contributes to constraint release in the nonlinear regime. The release rate grows with the convection rate in this regime, and becomes of the order of the shear rate at high shear rates [34]. This is known as **convective constraint release (CCR)**.

The most complete theory which includes the mechanisms of stretch and con-

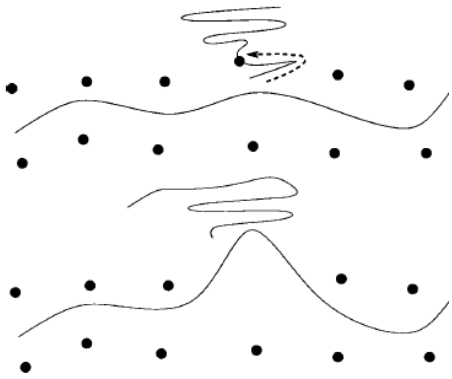

Figure 2.13: Schematic representation of a constraint release event, Figure from [34].

straint release in linear chains is due to Graham, Likhtman, McLeish and Milner otherwise referred to as the GLaMM model [34]. The GLaMM model also includes the mechanism of contour length fluctuations, in which the length of the tubes continuously fluctuates due to thermal noise. This is the most up to date theory for linear entangled polymers of different concentrations and in melt state in both linear and nonlinear regimes.

2.7 Remarks

The preceding discussion has been a general introduction of relevant theories involved in the calculations that shall follow in the later chapters. This study is purely theoretical in nature; there will be no presentation of experimental data except for comparison with calculations. Before proceeding with the calculations, it will be necessary to give more details of the experiments that motivated the calculations to be presented later and this will be taken care of in the next chapter.

Chapter 3

Experimental Background

The previous chapter was a review of key concepts commonly encountered in the theoretical study of polymeric liquids as well as theoretical models that shall be employed in the calculations that follow later. To proceed with this treatise, it is also necessary to give a quick review of concepts involved in the experimental study of polymeric fluids. Also, the key experiments that motivated the study described in the rest of this thesis will be presented in this chapter. The discussion in this chapter begins with a description of the apparatus used in typical experimental studies involving shear deformations and then continues to describe the key experiments of interest.

3.1 Rheometers

The principal apparatus for the experimental investigation of polymeric fluids is the rheometer. It could either be in the form of parallel plates or concentric cylinders. Another setup is the cone and plate configuration, but the calculations which will be presented in the later chapters of this discussion will be based on the first two configurations mentioned. A typical parallel plate arrangement is shown in Figure 3.1. The rheometer depicted in Figure 3.1 can be operated either in the

shear rate controlled mode or in stress controlled mode. These modes of operation are best understood from the relationship between stress and shear rate in simple Newtonian fluids, Equation (2.7).

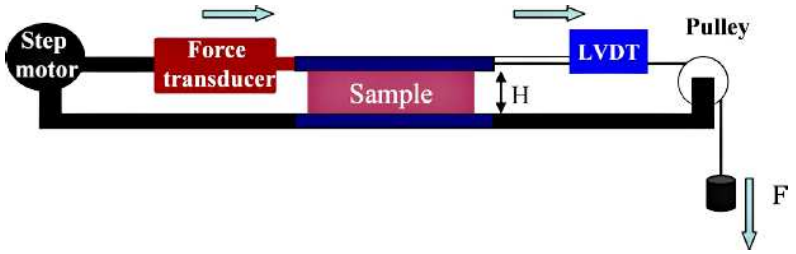

Figure 3.1: Typical setup of a parallel plate rheometer, Figure from [29].

In the shear rate controlled mode, the lower plate is fixed while the upper plate is moved by the step motor. The resulting force is measured by the force transducer, while the velocity of the plate is read from the linear variable differential transformer (LVDT). In this mode, the velocity of the upper plate is kept at a fixed value and the stress response is monitored. When the viscosity increases, the stress increases accordingly to keep the imposed shear rate (otherwise referred to as apparent shear rate) fixed. Otherwise, if the viscosity decreases, the stress decreases along with it. In the stress controlled mode, a constant force is imposed on the system by a weight attached to the pulley. In this case, the viscosity and shear rate respond accordingly to keep the imposed stress fixed at a particular value.

Another setup that is commonly used is concentric cylinders (also known as the cylindrical Couette configuration). In this case, the material is placed between two concentric cylinders. The outer cylinder is held fixed while the inner cylinder is free to rotate. A schematic representation of such an arrangement is shown in Figure 3.2. This rheometer works in either the shear rate controlled or stress controlled mode achieved with the torque transducer. In the stress controlled mode, a constant torque is imposed on the inner cylinder and the shear rate and viscosity are allowed to vary, while in the shear rate controlled mode a constant

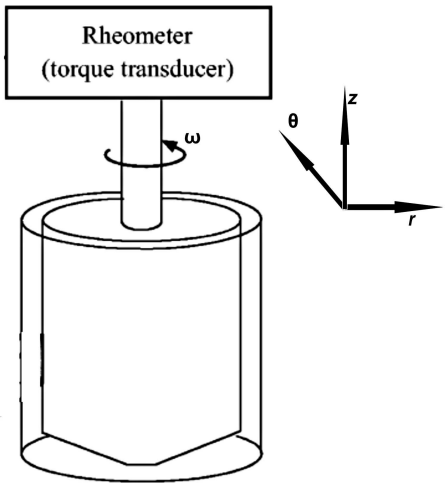

Figure 3.2: Basic arrangement of a Couette cell. The sample is placed between the two cylinders, while the inner cylinder rotates in the θ direction and the outer cylinder is stationary. The fluid flows in the θ direction while a velocity gradient exists in the r direction(adapted from [35]).

velocity is imposed on the inner cylinder while the stress and viscosity are allowed to vary. The cylindrical Couette configuration introduces stress gradients in the fluid contained between the cylinders due to curvature effects, as will be described in Chapter 4.

3.2 Step Strains with no Slip Hydrodynamic Boundary Condition (HBC)

In the experimental study of polymeric fluids using different plate configurations, it is not always possible to maintain a situation of zero slip between the material and the wall of the plates [36]. This is because of the possibility of polymer molecules attached to the wall to uncoil and disentangle from the bulk molecules [37]. There is also the possibility of polymers attached to the wall to detach and thus lead to slippage [38]. This is unlike the situation of Newtonian liquids where the fluid velocity at the fixed wall is zero and no slip exists at the moving wall. To overcome this difficulty of wall slip with polymeric fluids, some experimentalists [4, 39, 40]

have developed a gluing technique, where the material is glued to the surface of the walls. This allows them to maintaining zero slip at the walls, which is the case of no slip HBC.

This gluing technique allows the behaviour of the fluid under strong shear deformation in the absence of wall slip to be studied. The key experiments are described below.

3.2.1 Experiment I: 'Fracture' at Room Temperature

Using melts of styrene butadiene (SBR) whose number of tube entanglements ranged between 53-160, placed between flat plates, Boukany et al. [4] studied the stress relaxation behaviour after large step shears. The applied shear rates $\dot{\gamma}$ in the experiments were faster than the stretch relaxation times for the samples (that is, $\dot{\gamma}\tau_R > 1$). Thus the experiments approximated ideal step strains. Tiny silver coated particles were uniformly dispersed in the samples so that the movement of the fluid during and after shear cessation could be tracked, and all experiments were performed at room temperature.

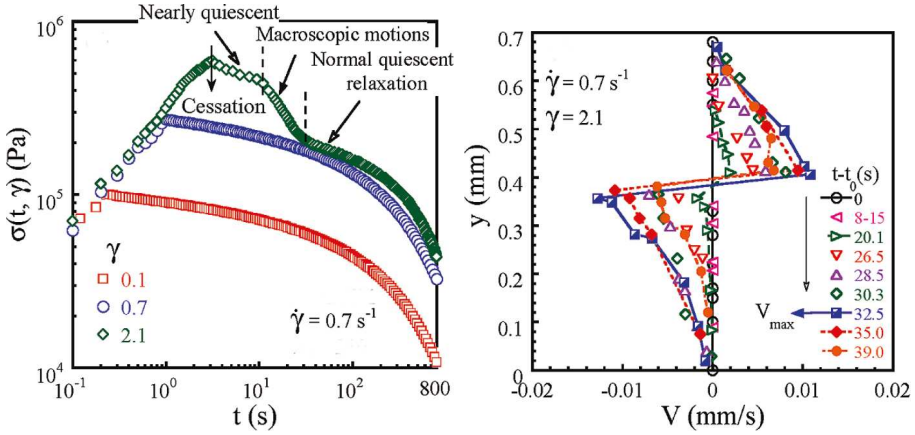

Figure 3.3: Left: Shear stress from startup to shear cessation and beyond for applied shear rate $\dot{\gamma} = 0.7\text{s}^{-1}$ and different strain amplitudes γ. Right: Velocity profile during 'fracture' at various times after shear cessation at t_0 for $\gamma = 2.1$, Figures from [4].

Different shear rates and strain amplitudes were applied. At sufficiently high

strain amplitude they noticed that the material appeared to break up after shear cessation. Upon cessation of shear at time t_0 the fluid appeared to come to a standstill, as shown on the right of Figure 3.3 where the strain amplitude $\gamma = 2.1$. The green diamonds on the left of Figure 3.3 show that the shear stress falls unto a plateau after shear cessation for this strain amplitude as indicated by 'nearly quiescent' in the Figure. After some seemingly delay or 'induction time', the shear stress begins to relax quickly in the region indicated as 'macroscopic motions' on the green diamonds on the left of Figure 3.3. These 'macroscopic motions' are fluid particles moving on opposite sides of a 'failure' plane, which is a plane perpendicular to the plane of Figure 3.3 which separates the two layers of fluid moving in opposite directions. The fluid appears to have broken up in two layers, with each layer moving in opposite directions. This phenomenon resembles fracture in a solid and was interpreted to be due to a complete breakdown of the entanglement network [4]. The fluid resumes the usual quiescent relaxation after the 'fracture' event as indicated by 'normal quiescent relaxation' on the left of Figure 3.3.

This fracture-like behaviour was not observed when the strain amplitude was insufficient, as in the case of $\gamma = 0.1$ and $\gamma = 0.7$ on the left of Figure 3.3. Also, the location of the failure plane was not fixed for different runs of the experiment but occurred in different positions within the bulk of the fluid. However, the stress relaxation profile was the same always [4].

Other features of this experiment are summarised below:

I The 'Fracture' phenomenon still occurred when shearing is stopped before 'elastic yielding' (the stress overshoot) of shear stress or when shearing is performed slowly.

II The Delay time during initial slow stress relaxation increases with molecular weight and shear rate, but decreases with increasing strain.

3.2.2 Experiment II: 'Fracture' at High Temperature

Using a similar gluing technique to maintain no slip HBC and particle tracking as in Experiment I, Fang et al. [40] reproduced fracture-like behaviour in poly(ethylene oxide) (PEO) melts whose number of chain entanglements was roughly 146. The experiments were performed in cone and plate configuration in an oven whose temperature varied between 303 K and 473 K.

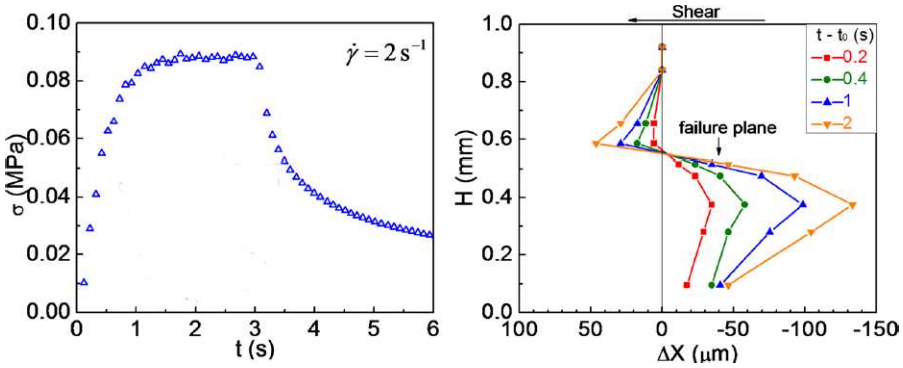

Figure 3.4: Left: Shear stress from startup to shear cessation and beyond for applied shear rate $\dot{\gamma} = 2s^{-1}$ and strain amplitude $\gamma = 6$ at a temperature of 353K. Right: Displacement of fluid particles during 'fracture' at various times after shear cessation at t_0. Figures from [40].

Similar to the case of Experiment I, fracture-like behaviour was observed in the samples after cessation of shear at sufficient strain amplitude. However, the shear stress does not show a clear 'induction' period as seen on the left of Figure 3.4, unlike the case of Experiment I. The reason for this is not clear but could be related to some difficulties in the measurements. However, the fluid particles show a clear 'failure plane' as seen on the right of Figure 3.4, just like in Experiment I. Also, for different runs of the experiments, the positions of the 'failure plane' was not fixed, but the stress profile was the same [40].

3.3 Remarks

The experiments with no slip HBC are quite revealing. Although different viscoelastic models have described the elastic and viscous nature of polymeric liquids to various extents, it is the first time this elastic character has been demonstrated clearly in an experiment. Also, no calculation has been carried out before now to demonstrate this phenomenon theoretically. While the experiments are interesting, they leave a puzzle, 'what is the mechanism behind this behaviour?' Otherwise, one can ask 'what is the origin of this fracture-like behaviour in a liquid?' There have been suggestions that this behaviour originates from a complete breakdown of the entanglement network which was supposed to be a violation of the tube model [4], so that new physics will be required to explain this phenomenon. Although tube models are not complete as they stand now [41] since they do not give an exact quantitative match to some experimental data. However, the qualitative agreement of tube model predictions with many experimental data is spectacular. Hence it may be possible to accommodate this phenomenon within the frame work of current tube models without new physics. This possibility will be examined in the remaining parts of this thesis. For the purpose of this study, one of the variants of the tube model shall be employed and it shall be described in the next chapter.

Chapter 4

Theoretical Model

Having described the experiments that motivated the calculations to be presented during the course of this thesis, the treatise now proceeds with a description of the theoretical model that shall be employed in the calculations. Different properties of a fluid can be calculated by solving the relevant hydrodynamic equations. For the case of Newtonian liquids, the calculation is straight forward since the representation of the stress tensor is known. But this is not the case for polymeric liquids, as they are non Newtonian. Hence, appropriate viscoelastic models have to be introduced to calculate the relevant stress components. The Rolie-Poly (RP) model [42], which simplifies the set of equations from the GLaMM [34] model, shall be employed here. A description of the relevant hydrodynamic equations and the RP model now follow.

4.1 Flow Field

The velocity vectors in space constitute the flow field. In the current study the velocity is treated as a function of one spatial dimension and time. The fluid

velocity is obtained from the momentum equation

$$\rho \frac{d\mathbf{v}}{dt} \equiv \rho \left[\partial_t \mathbf{v} + (\mathbf{v} \cdot \nabla)\, \mathbf{v}\right] = \nabla \cdot \mathbf{T}, \tag{4.1}$$

where ρ is the fluid density and $\mathbf{T}$ is the total stress tensor defined in Equation (4.2). The polymeric stress $\boldsymbol{\sigma}$ is obtained from an appropriate viscoelastic model suitable for the system under study. In some situations the polymer is dissolved in a solvent, and the solvent can either be Newtonian or a polymer of lower molecular mass. In the calculations here, the polymer is assumed to be dissolved in a Newtonian solvent of viscosity η. So that the total stress from the solution is then the sum of stress from the polymer $\boldsymbol{\sigma}$ and that from the Newtonian solvent $\mathbf{D}$ (where $\mathbf{D} = \boldsymbol{\kappa} + \boldsymbol{\kappa}^T$, and the velocity gradient tensor $\boldsymbol{\kappa} = (\nabla \mathbf{v})^{\mathrm{T}}$ [43]). This leads to the following expression for the total stress

$$\mathbf{T} = \boldsymbol{\sigma} + \eta(\boldsymbol{\kappa} + \boldsymbol{\kappa}^T) - p\boldsymbol{\delta}. \tag{4.2}$$

4.2 The Rolie-Poly (RP) Model

The GLaMM model [34] introduced in Section 2.6 derives the polymer contribution to the total stress from the position vector for each tube segment as shown in Figure 4.1. To this end, the tube of diameter a_d is discretized into $Z = M/M_e$ segments $S_1, S_2, ..., S_z$ whose position vectors are $\mathbf{R}_1, \mathbf{R}_2, ..., \mathbf{R}_z$ as shown in Figure 4.1. Where M is the molecular weight and M_e is the molecular weight between entanglements of the polymer. The position vector $\mathbf{R}(s,t)$ (where t is time), whose time evolution is given by a stochastic partial differential equation (SDE) contains information about the shape of the chain, and from this knowledge, various macroscopic quantities can be derived. This is possible since the SDE has s and t dependence and it has contributions from various sources of motion of the chain.

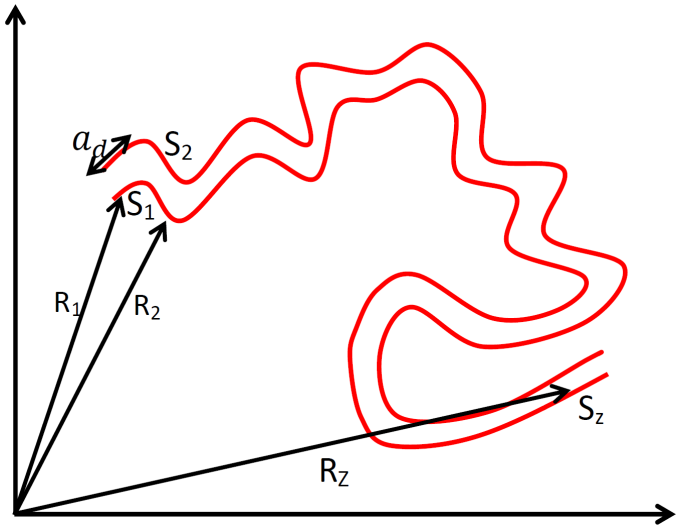

Figure 4.1: Schematic representation of the tube and the position vectors describing its conformation.

The polymer contribution to the total stress is obtained from the tangent correlation function f_{kl} (where k and l are indices in the Cartesian coordinate system) as [34, 42]

$$\begin{aligned} \sigma_{kl} &= \frac{3G}{Z} \int_0^Z f_{kl}(s,s)ds \\ f_{kl} &= \left\langle \frac{\partial R_k(s)}{\partial s} \frac{\partial R_l(s')}{\partial s'} \right\rangle, \end{aligned} \tag{4.3}$$

where G is the plateau modulus. The tangent correlation function contains information about tube orientation, chain stretch and chain trajectories.

The GLaMM model is completed with a partial differential equation (PDE) describing the time evolution of f_{kl}. This PDE is derived from the original SDE describing the time evolution of $\mathbf{R}(s,t)$. The nonlinear PDE describing the time evolution of f_{kl} has s dependence since it contains many relaxation modes of the chain, and this makes it difficult to implement in numerical simulations. The GLaMM model is very successful for linear chains. It was found [34] to give a good match to a wide class of experimental data; ranging from, linear oscillatory shear to steady shear viscosity, first normal stress difference, uniaxial extension and more.

To reduce the difficulty of implementing the GLaMM model in numerical simulations, the Rolie Poly (RP) model removes all s dependence in f_{kl} making it a single mode model. Similar to the GLaMM model, the polymer contribution to the total stress is given by [42]

$$\boldsymbol{\sigma} = G\mathbf{W}, \tag{4.4}$$

where $\mathbf{W}$ is the tangent correlation function averaged over s. Also, $\mathbf{W}$ contains information about the chain orientation, stretch and constraint release events. It can be seen as a measure of the strain on the tube. The PDE describing the time evolution of $\mathbf{W}$ is given by the RP model as [42]

$$\begin{aligned}\frac{d\mathbf{W}}{dt} = &\underbrace{\boldsymbol{\kappa}\cdot\mathbf{W} + \mathbf{W}\cdot\boldsymbol{\kappa}^T}_{I} - \underbrace{\frac{1}{\tau_d}(\mathbf{W}-\mathbf{I})}_{II} \\ &\underbrace{- \frac{2(1-\sqrt{3/\mathrm{tr}(\mathbf{W})})}{\tau_R}\left(\mathbf{W} + \beta\left(\frac{\mathrm{tr}\mathbf{W}}{3}\right)^{\delta}(\mathbf{W}-\mathbf{I})\right)}_{III},\end{aligned} \tag{4.5}$$

where $\mathbf{I}$ is the identity tensor and the parameter δ is a fitting parameter for experimental data [42]. The CCR parameter β models the degree of convective constraint release in the system.

The RP model is easier to implement in numerical simulations than the original GLaMM model. But the RP constitutive equation is nonlinear and this situation still introduces complications in numerical simulations. The RP model is a good choice for the kind of study being carried out here because it has been shown to give a good match to the GLaMM model as well as to experimental data [42] (at appropriate parameter values) and it contains the necessary physics exhibited by real polymer solutions at different concentrations.

Real polymer chains get stretched at sufficiently high strain rates and relax this stretch quickly when the flow is switched off. Although the time scale for this stretch relaxation is small, it is not negligible (for fast shear flows) as was assumed

in the DE theory. Also, the CCR parameter in the RP model can be adjusted to remove the stress maximum predicted by the DE theory and hence obtain better agreement with experimental data. The CCR parameter can also be adjusted to recover the original nonmonotonic behaviour of the DE constitutive equation. This will prove useful here where the 'fracture' reported in [4] may be due to the unstable nature of polymeric liquids.

The RP constitutive equation is easily understood by examining its predictions for the behaviour of the fluid under step shear. In typical well entangled solutions, the stretch relaxation time is much less than the reptation time, $\tau_R << \tau_d$. Thus, under fast deformations (a large step shear) such that $1/\dot{\gamma} << \tau_R << \tau_d$, the terms I dominates the right hand side of Equation (4.5) giving

$$\frac{d\mathbf{W}}{dt} = \boldsymbol{\kappa} \cdot \mathbf{W} + \mathbf{W} \cdot \boldsymbol{\kappa}^{\mathrm{T}}, \tag{4.6}$$

which then leads to a stress build up. At the end of the step shear (shear cessation), the tensor $\boldsymbol{\kappa}$ vanishes. Since $\tau_R << \tau_d$ then the term III dominates the right hand side of Equation (4.5) at the early stages of stress relaxation. Thus the early stages of stress relaxation is due mainly to relaxation of chain stretch which occurs on time scale of τ_R. In the RP equation, chain stretch is represented by the term $\mathrm{tr}(\mathbf{W})$, so that the effective stress relaxation due to relaxation of chain stretch is given by

$$\frac{d\mathbf{W}}{dt} = -\frac{2(1-\sqrt{3/\mathrm{tr}(\mathbf{W})})}{\tau_R}\left(\mathbf{W} + \beta\left(\frac{\mathrm{tr}\mathbf{W}}{3}\right)^{\delta}(\mathbf{W}-\mathbf{I})\right). \tag{4.7}$$

Finally, at the later stages of stress relaxation, the term II dominates so that stress relaxation is then due to reptation which occurs on a time scale of τ_d. Information about chain stretch can be obtained by computing the quantity $\mathrm{tr}\mathbf{W}$. Hence the momentum Equation (4.1) can be solved using the Equation (4.5). From

the velocity field the shear rate can be computed, hence the accumulated strain is computed.

In the case of steady shear, for times $t << \tau_R$ after startup, the terms II and III in Equation (4.5) have negligible effect on the stress. Hence, the stress grows due to the deformation described by the term I in Equation (4.5). However, as time time approaches τ_R the term III starts to dissipate the stress, and eventually the term II contributes to this dissipation. Finally, the stress passes through a maximum and decreases to some steady value. At this time the terms II and III balance the term I in Equation (4.5) and the time derivative vanishes, and this is the steady state situation. However, if the imposed shear rate $\langle\widehat{\dot{\gamma}}\rangle$ is such that $\langle\widehat{\dot{\gamma}}\rangle\tau_d < 1$, the stress does not pass through a maximum before reaching the steady state.

4.3 Stress Diffusivity

The RP Equation (4.5) assumes uniform conditions in space, which is not necessarily true. The spatial profile of the shear rate could become non uniform depending on the average shear rate imposed on the material. To account for this possibility Lu et al. [44, 45] extended the original idea of stress diffusivity introduced by El-Kareh and Leal [46] to a simpler viscoelastic model known as the Johnson-Segalmann (JS) model [47].

Similarly, the locality of the RP Equation (4.5) is removed by the addition of stress diffusivity, and the RP equation with the diffusive term is known as the diffusive RP equation (DRP) given as [25]

$$\begin{aligned}\frac{d\mathbf{W}}{dt} =& \boldsymbol{\kappa}\cdot\mathbf{W} + \mathbf{W}\cdot\boldsymbol{\kappa}^T - \frac{1}{\tau_d}(\mathbf{W}-\mathbf{I}) \\ &- \frac{2(1-\sqrt{3/\mathrm{tr}(\mathbf{W})})}{\tau_R}\left(\mathbf{W} + \beta\left(\frac{\mathrm{tr}\mathbf{W}}{3}\right)^{\delta}(\mathbf{W}-\mathbf{I})\right) + \mathscr{D}\nabla^2\mathbf{W},\end{aligned} \tag{4.8}$$

where $\mathscr{D}$ is stress diffusion constant.

The shear stress falls into a plateau in the range $1/\tau_d < \langle\dot{\gamma}\rangle < 1/\tau_R$, where $\langle\dot{\gamma}\rangle$ is the spatially averaged shear rate. The presence of stress diffusivity ensures that the selected plateau stress is unique [44, 45]. Also during shear banding, the width of the interface between the two bands of fluids at high and low viscosities is set by the stress diffusion constant [44, 45, 23]. More details of the physical effects of the diffusive term will be given later in this Chapter.

The phenomena of interest in this study occur when the system is out of equilibrium, hence it is useful to separate the tensor $\mathbf{W}$ into its equilibrium part $\mathbf{I}$ (the identity tensor) and its non equilibrium part $\mathbf{\Delta}$, so that $\mathbf{W} = \mathbf{I} + \mathbf{\Delta}$, where $\mathbf{\Delta}$ is zero at equilibrium. Substitution into the DRP equation gives

$$\begin{aligned}\frac{d\mathbf{\Delta}}{dt} &= \boldsymbol{\kappa}\cdot\mathbf{\Delta} + \mathbf{\Delta}\cdot\boldsymbol{\kappa}^T + \boldsymbol{\kappa} + \boldsymbol{\kappa}^T - \frac{1}{\tau_d}\mathbf{\Delta} \\ &\quad - \frac{2}{\tau_R}\left[1 - \left(1 + \frac{\mathrm{tr}(\mathbf{\Delta})}{3}\right)^{-1/2}\right]\left[\left(\beta\left(\frac{\mathrm{tr}\mathbf{\Delta}}{3}+1\right)^{\delta}+1\right)\mathbf{\Delta} + \mathbf{I}\right] + \mathscr{D}\nabla^2\mathbf{\Delta}.\end{aligned} \tag{4.9}$$

4.4 Coupled System of Equations in Different Geometries

For easy comparison of calculations with experimental data, it is necessary to apply different coordinate systems corresponding to the plate geometries commonly used in experiments. All calculations presented here will be carried out in 2-dimensions, considering only the flow and velocity gradient directions.

4.4.1 Flat Plates

For the case where the material is placed between two flat plates (assumed to be infinite) of separation L as depicted in Figure 2.2, the Cartesian coordinate system

is used. In this case, the flow direction is $\hat{\mathbf{x}}$ and the velocity gradient direction is $\hat{\mathbf{y}}$, so that $\mathbf{v} = v_x(y,t)\hat{\mathbf{x}}$ and $\boldsymbol{\Delta} = \boldsymbol{\Delta}(y,t)$. Using

$$\nabla = \hat{\mathbf{x}}\frac{\partial}{\partial x} + \hat{\mathbf{y}}\frac{\partial}{\partial y} \tag{4.10}$$

$$\kappa_{\alpha\beta} = (\nabla \mathbf{v})^{\mathrm{T}} = \partial_\alpha v_\beta = \begin{pmatrix} 0 & \dot{\gamma} \\ 0 & 0 \end{pmatrix} \tag{4.11a}$$

$$\dot{\gamma} = \frac{\partial v_x}{\partial y} \tag{4.11b}$$

$$\boldsymbol{\Delta} = \begin{pmatrix} \Delta_{xx} & \Delta_{xy} \\ \Delta_{xy} & \Delta_{yy} \end{pmatrix} \tag{4.12}$$

$$\boldsymbol{\kappa}\cdot\boldsymbol{\Delta} + \boldsymbol{\Delta}\cdot\boldsymbol{\kappa}^{\mathrm{T}} = \begin{pmatrix} 2\dot{\gamma}\Delta_{xy} & \dot{\gamma}\Delta_{yy} \\ \dot{\gamma}\Delta_{yy} & 0 \end{pmatrix} \tag{4.13}$$

$$\boldsymbol{\kappa} + \boldsymbol{\kappa}^{\mathrm{T}} = \begin{pmatrix} 0 & \dot{\gamma} \\ \dot{\gamma} & 0 \end{pmatrix} \tag{4.14}$$

and substituting into Equation (4.9) gives

$$\frac{\partial \Delta_{xx}}{\partial t} = 2\Delta_{xy}\dot{\gamma} - \frac{1}{\tau_d}\Delta_{xx} - \frac{2}{\tau_R}[1-A]\left[(\beta A+1)\,\Delta_{xx}+1\right] + \mathcal{D}\frac{\partial^2 \Delta_{xx}}{\partial y^2} \tag{4.15a}$$

$$\frac{\partial \Delta_{xy}}{\partial t} = \dot{\gamma} + \dot{\gamma}\Delta_{yy} - \frac{1}{\tau_d}\Delta_{xy} - \frac{2}{\tau_R}[1-A](\beta A+1)\Delta_{xy} + \mathcal{D}\frac{\partial^2 \Delta_{xy}}{\partial y^2} \tag{4.15b}$$

$$\frac{\partial \Delta_{yy}}{\partial t} = -\frac{1}{\tau_d}\Delta_{yy} - \frac{2}{\tau_R}[1-A][(\beta A+1)\Delta_{yy}+1] + \mathcal{D}\frac{\partial^2 \Delta_{yy}}{\partial y^2} \tag{4.15c}$$

$$A = \left(1 + \frac{\mathrm{Tr}\boldsymbol{\Delta}}{3}\right)^{-1/2}, \tag{4.15d}$$

where $\delta = -1/2$ has been used. This value of δ has been shown to give the best fit to experimental data [42]. Using the rescaled quantities

$$\begin{aligned}
\widehat{\dot{\gamma}} &= \dot{\gamma}\tau_d \\
\widehat{t} &= t/\tau_d \\
\widehat{\tau}_R &= \tau_R/\tau_d \\
\widehat{y} &= y/L \\
\widehat{\mathcal{D}} &= \frac{\mathcal{D}\tau_d}{L^2},
\end{aligned} \tag{4.16}$$

gives (writing $\widehat{t}$ as t, $\widehat{\tau}_R$ as τ_R and $\widehat{y}$ as y for simplicity)

$$\frac{\partial \Delta_{xx}}{\partial t} = 2\Delta_{xy}\widehat{\dot{\gamma}} - \Delta_{xx} - \frac{2}{\tau_R}[1-A]\left[(\beta A+1)\,\Delta_{xx}+1\right] + \widehat{\mathcal{D}}\frac{\partial^2 \Delta_{xx}}{\partial y^2} \tag{4.17a}$$

$$\frac{\partial \Delta_{xy}}{\partial t} = \widehat{\dot{\gamma}} + \widehat{\dot{\gamma}}\Delta_{yy} - \Delta_{xy} - \frac{2}{\tau_R}[1-A](\beta A+1)\Delta_{xy} + \widehat{\mathcal{D}}\frac{\partial^2 \Delta_{xy}}{\partial y^2} \tag{4.17b}$$

$$\frac{\partial \Delta_{yy}}{\partial t} = -\Delta_{yy} - \frac{2}{\tau_R}[1-A][(\beta A+1)\Delta_{yy}+1] + \widehat{\mathcal{D}}\frac{\partial^2 \Delta_{yy}}{\partial y^2}. \tag{4.17c}$$

Calculations with the momentum Equation (4.1) can be simplified by taking advantage of the sluggishness of the polymeric liquids under consideration here. The dynamics of these liquids is heavily dominated by viscosity as can be seen by computing their Reynolds number R_e using typical material properties. The Reynolds number determines the balance between inertia and viscosity in a fluid. The Reynolds number is given as [6]

$$R_e = \frac{\tilde{\rho}\tilde{V}\tilde{L}}{\tilde{\mu}}, \tag{4.18}$$

where $\tilde{\rho}$ is the fluid density, $\tilde{V}$ is typical velocity of the fluid, $\tilde{L}$ is typical length scale of the system and $\tilde{\mu}$ is fluid viscosity. Typical parallel plate configurations have gap sizes $\tilde{L} \sim 1\text{mm}$, and fluid velocity $\tilde{V} \sim 1\text{mm}\,\text{s}^{-1}$ [4]. The typical densities

are fairly close to $\tilde{\rho} \sim 1\mathrm{g\,cm^{-3}}$ [48], but the viscosities vary widely depending on molecular weight. Using viscosity $\tilde{\mu} \sim 10^5\mathrm{Pa\,s}$ for a polybutadiene sample [49] gives the Reynolds number as $R_e \approx 10^{-8} << 1$.

This implies that the inertia contribution to Equation (4.1) can be neglected giving

$$\nabla \cdot \mathbf{T} = 0. \tag{4.19}$$

Equations (4.10) and (4.12) give

$$\frac{\partial T_{xy}}{\partial y} = 0 \tag{4.20a}$$

$$\frac{\partial T_{yy}}{\partial y} = 0, \tag{4.20b}$$

which implies constant total stress in the space between the flat plates. Taking the shear component of Equation (4.2) gives

$$T_{xy} = G\Delta_{xy} + \eta\dot{\gamma}. \tag{4.21}$$

Although the quantities Δ_{xy} and $\dot{\gamma}$ have spatial dependence, they balance each other so that T_{xy} is uniform in space. Using

$$\begin{aligned} \widehat{T}_{xy} &= \frac{T_{xy}}{G} \\ \epsilon &= \frac{\eta}{G\tau_d}, \end{aligned} \tag{4.22}$$

gives

$$\widehat{T}_{xy} = \Delta_{xy} + \epsilon\widehat{\dot{\gamma}}. \tag{4.23}$$

Since

$$\widehat{T}_{xy} = \langle\widehat{T}_{xy}\rangle = \langle\Delta_{xy}\rangle + \epsilon\langle\widehat{\dot{\gamma}}\rangle, \tag{4.24}$$

then Equation (4.23) gives

$$\widehat{\dot{\gamma}} = \langle \widehat{\dot{\gamma}} \rangle + \frac{1}{\epsilon} \left[\langle \Delta_{xy} \rangle - \Delta_{xy} \right]. \tag{4.25}$$

The spatial average of any quantity $\diamond$ is defined as

$$\langle \diamond \rangle = \int_0^1 \diamond dy. \tag{4.26}$$

Equation (4.25) allows the calculation of the spatially resolved shear rate from the spatially averaged shear rate and the polymer stress. The fluid velocity is then obtained from

$$\widehat{\dot{\gamma}} = \frac{\partial \widehat{v}_x}{\partial y}, \tag{4.27}$$

leading to

$$\widehat{v}_x(y,t) = \int_0^y \widehat{\dot{\gamma}}(y',t) dy', \tag{4.28}$$

where $\widehat{v}_x = v\tau_d/L$.

Using Equations (4.17) and (4.25), the stress components and shear rate can be computed in space and time. Finally, Equation (4.28) allows the velocity field to be computed. A discussion of the numerical scheme used in the calculations is deferred to Chapter 5.

4.4.2 Concentric Cylinders

The representation of a point P in the cylindrical coordinate system is sketched in Figure 4.2. By translating the plane containing the xy axes, the corresponding representation of the point P in the Cartesian coordinate system can be obtained. The representation of a point in the cylindrical coordinate system is completely specified by the unit vectors $(\hat{\mathbf{r}}, \hat{\boldsymbol{\theta}}, \hat{\mathbf{z}})$.

For the case where the material is placed between two concentric cylinders

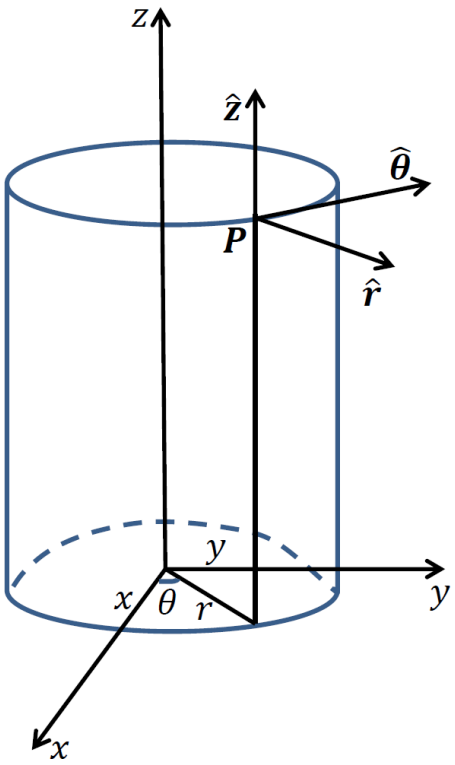

Figure 4.2: Sketch of a point P represented in the cylindrical coordinate system and its corresponding representation in the Cartesian coordinate system.

whose inner radius is R_1 and outer radius R_2, with the flow in the $\hat{\boldsymbol{\theta}}$ direction and velocity gradient in the $\hat{\mathbf{r}}$ direction, then $\mathbf{v} = v_\theta(r,t)\hat{\boldsymbol{\theta}}$ and $\boldsymbol{\Delta} = \boldsymbol{\Delta}(r,t)$. Using

$$\nabla = \hat{\mathbf{r}}\frac{\partial}{\partial r} + \hat{\boldsymbol{\theta}}\frac{1}{r}\frac{\partial}{\partial \theta} \tag{4.29}$$

gives

$$\boldsymbol{\kappa} = (\nabla \mathbf{v})^{\mathrm{T}} = \begin{pmatrix} 0 & -\frac{v_\theta}{r} \\ \frac{\partial v_\theta}{\partial r} & 0 \end{pmatrix}. \tag{4.30}$$

The quantity

$$\begin{aligned} \dot{\gamma} =& \frac{\partial v_\theta(r)}{\partial r} - \frac{v_\theta(r)}{r} \\ =& r\frac{\partial}{\partial r}\left(\frac{v_\theta}{r}\right), \end{aligned} \tag{4.31}$$

occurring in the tensor

$$\boldsymbol{\kappa} + \boldsymbol{\kappa}^T = \begin{pmatrix} 0 & \frac{\partial v_\theta}{\partial r} - \frac{v_\theta}{r} \\ \frac{\partial v_\theta}{\partial r} - \frac{v_\theta}{r} & 0 \end{pmatrix}. \tag{4.32}$$

is defined as the shear rate in the cylindrical coordinates system. Integrating Equation (4.30) from the inner to the outer cylinder gives

$$\int_{R_1}^{R_2} \frac{\dot{\gamma}}{r} dr = \int_{R_1}^{R_2} \frac{\partial}{\partial r} \left(\frac{v_\theta}{r} \right) dr, \tag{4.33}$$

so that using the transformations

$$\begin{aligned} \xi =& \frac{1}{q} \ln \frac{r}{R_1} \\ q =& \ln \frac{R_2}{R_1} \end{aligned} \tag{4.34}$$

gives

$$\frac{v_\theta}{r}\Big|_{R_1}^{R_2} = \int_0^1 q\dot{\gamma} d\xi. \tag{4.35}$$

In the calculations performed here, no slip boundary conditions are imposed on the fluid velocity so that the velocities at the boundaries are given by

$$\begin{aligned} v_\theta(R_1) &= \mathscr{V} \\ v_\theta(R_2) &= 0. \end{aligned} \tag{4.36}$$

Where $\mathscr{V}$ is the velocity of the moving cylinder. Hence Equation (4.35) then gives

$$\frac{\mathscr{V}}{qR_1} = -\int_0^1 \dot{\gamma} d\xi. \tag{4.37}$$

Multiplying through by τ_d gives

$$\hat{\mathscr{V}} = -\int_0^1 \hat{\dot{\gamma}} d\xi, \tag{4.38}$$

where $\hat{\mathscr{V}} = \mathscr{V}\tau_d/(qR_1)$. Since the integral on the right hand side of Equation (4.38) is the spatially averaged shear rate $\langle\hat{\dot{\gamma}}\rangle$, it follows that the imposed cylinder velocity is related to the spatially averaged shear rate by

$$\hat{\mathscr{V}} = -\int_0^1 \hat{\dot{\gamma}} d\xi = -\langle\hat{\dot{\gamma}}\rangle \tag{4.39}$$

with these rescaled quantities. Using

$$\frac{\partial v_\theta}{\partial \theta} = \frac{\partial \hat{\boldsymbol{\theta}}}{\partial r} = 0, \tag{4.40}$$

$$\frac{\partial \hat{\mathbf{r}}}{\partial \theta} = \hat{\boldsymbol{\theta}}, \quad \frac{\partial \hat{\boldsymbol{\theta}}}{\partial \theta} = -\hat{\mathbf{r}}, \tag{4.41}$$

and

$$\boldsymbol{\Delta} = \begin{pmatrix} \Delta_{rr} & \Delta_{r\theta} \\ \Delta_{r\theta} & \Delta_{\theta\theta} \end{pmatrix} \tag{4.42}$$

give

$$(\mathbf{v}\cdot\nabla)\boldsymbol{\Delta} = \frac{v_\theta}{r}\begin{pmatrix} -2\Delta_{r\theta} & \Delta_{rr}-\Delta_{\theta\theta} \\ \Delta_{rr}-\Delta_{\theta\theta} & 2\Delta_{r\theta} \end{pmatrix}, \tag{4.43}$$

$$\boldsymbol{\kappa}\cdot\boldsymbol{\Delta} = \begin{pmatrix} -\frac{v_\theta}{r}\Delta_{r\theta} & -\frac{v_\theta}{r}\Delta_{\theta\theta} \\ \frac{\partial v_\theta}{\partial r}\Delta_{rr} & \frac{\partial v_\theta}{\partial r}\Delta_{r\theta} \end{pmatrix}, \tag{4.44}$$

and

$$\boldsymbol{\Delta}\cdot\boldsymbol{\kappa}^T = \begin{pmatrix} -\frac{v_\theta}{r}\Delta_{r\theta} & \frac{\partial v_\theta}{\partial r}\Delta_{rr} \\ -\frac{v_\theta}{r}\Delta_{\theta\theta} & \frac{\partial v_\theta}{\partial r}\Delta_{r\theta} \end{pmatrix}. \tag{4.45}$$

Also using

$$\nabla^2 = \frac{\partial^2}{\partial r^2} + \frac{1}{r}\frac{\partial}{\partial r} + \frac{1}{r^2}\frac{\partial^2}{\partial \theta^2}, \tag{4.46}$$

gives

$$\begin{aligned}\nabla^2 \boldsymbol{\Delta} = &\left[\frac{\partial^2 \Delta_{rr}}{\partial r^2} + \frac{1}{r}\frac{\partial \Delta_{rr}}{\partial r} - \frac{2}{r^2}\Delta_{rr} + \frac{2}{r^2}\Delta_{\theta\theta}\right]\hat{\mathbf{r}}\hat{\mathbf{r}} + \left[\frac{\partial^2 \Delta_{r\theta}}{\partial r^2} + \frac{1}{r}\frac{\partial \Delta_{r\theta}}{\partial r} - \frac{4}{r^2}\Delta_{r\theta}\right]\left(\hat{\boldsymbol{\theta}}\hat{\mathbf{r}} + \hat{\mathbf{r}}\hat{\boldsymbol{\theta}}\right) \\ &+ \left[\frac{\partial^2 \Delta_{\theta\theta}}{\partial r^2} + \frac{1}{r}\frac{\partial \Delta_{\theta\theta}}{\partial r} - \frac{2}{r^2}\Delta_{\theta\theta} + \frac{2}{r^2}\Delta_{rr}\right]\hat{\boldsymbol{\theta}}\hat{\boldsymbol{\theta}}.\end{aligned} \tag{4.47}$$

Substitution into Equation (4.9) and using Equation (4.31) gives the following system of coupled nonlinear partial differential equations:

$$\begin{aligned}\frac{\partial \Delta_{\theta\theta}}{\partial t} =& 2\dot{\gamma}\Delta_{r\theta} - \frac{1}{\tau_d}\Delta_{\theta\theta} - \frac{2}{\tau_R}\left[1-\widetilde{A}\right]\left[\left(\beta\widetilde{A}+1\right)\Delta_{\theta\theta}+1\right] \\ &+ \mathscr{D}\left[\frac{\partial^2 \Delta_{\theta\theta}}{\partial r^2} + \frac{1}{r}\frac{\partial \Delta_{\theta\theta}}{\partial r} - \frac{2}{r^2}\left(\Delta_{\theta\theta} - \Delta_{rr}\right)\right] \qquad (4.48a) \\ \frac{\partial \Delta_{r\theta}}{\partial t} =& \dot{\gamma}\left[\Delta_{rr}+1\right] - \frac{1}{\tau_d}\Delta_{r\theta} - \frac{2}{\tau_R}\left[1-\widetilde{A}\right]\left[\beta\widetilde{A}+1\right]\Delta_{r\theta} \\ &+ \mathscr{D}\left[\frac{\partial^2 \Delta_{r\theta}}{\partial r^2} + \frac{1}{r}\frac{\partial \Delta_{r\theta}}{\partial r} - \frac{4}{r^2}\Delta_{r\theta}\right] \qquad (4.48b) \\ \frac{\partial \Delta_{rr}}{\partial t} =& -\frac{1}{\tau_d}\Delta_{rr} - \frac{2}{\tau_R}\left[1-\widetilde{A}\right]\left[\left(\beta\widetilde{A}+1\right)\Delta_{rr}+1\right] \\ &+ \mathscr{D}\left[\frac{\partial^2 \Delta_{rr}}{\partial r^2} + \frac{1}{r}\frac{\partial \Delta_{rr}}{\partial r} + \frac{2}{r^2}\left(\Delta_{\theta\theta} - \Delta_{rr}\right)\right] \qquad (4.48c) \\ \widetilde{A} =& \left(1 + \frac{\Delta_{\theta\theta} + \Delta_{rr}}{3}\right)^{-1/2}. \qquad (4.48d)\end{aligned}$$

Then, using transformation Equation (4.34), dimensionless time t and τ_R with

$$\widehat{\mathscr{D}} = \frac{\mathscr{D}\tau_d}{qR_1^2} \tag{4.49}$$

gives

$$\begin{aligned}
\frac{\partial \Delta_{\theta\theta}}{\partial t} =& 2\hat{\dot{\gamma}}\Delta_{r\theta} - \Delta_{\theta\theta} - \frac{2}{\tau_R}\left[1-\widetilde{A}\right]\left[\left(\beta\widetilde{A}+1\right)\Delta_{\theta\theta}+1\right] \\
&+ \widehat{\mathscr{D}}e^{-2q\xi}\left[\frac{\partial^2\Delta_{\theta\theta}}{\partial\xi^2} - 2q^2\left(\Delta_{\theta\theta}-\Delta_{rr}\right)\right] \qquad (4.50a)\\
\frac{\partial \Delta_{r\theta}}{\partial t} =& \hat{\dot{\gamma}}\left[\Delta_{rr}+1\right] - \Delta_{r\theta} - \frac{2}{\tau_R}\left[1-\widetilde{A}\right]\left[\beta\widetilde{A}+1\right]\Delta_{r\theta} \\
&+ \widehat{\mathscr{D}}e^{-2q\xi}\left[\frac{\partial^2\Delta_{r\theta}}{\partial\xi^2} - 4q^2\Delta_{r\theta}\right] \qquad (4.50b)\\
\frac{\partial \Delta_{rr}}{\partial t} =& -\Delta_{rr} - \frac{2}{\tau_R}\left[1-\widetilde{A}\right]\left[\left(\beta\widetilde{A}+1\right)\Delta_{rr}+1\right] \\
&+ \widehat{\mathscr{D}}e^{-2q\xi}\left[\frac{\partial^2\Delta_{rr}}{\partial\xi^2} + 2q^2\left(\Delta_{\theta\theta}-\Delta_{rr}\right)\right]. \qquad (4.50c)
\end{aligned}$$

Using

$$\nabla\cdot\mathbf{T} = G\nabla\cdot\mathbf{W} + \eta\nabla\cdot(\boldsymbol{\kappa}+\boldsymbol{\kappa}^T), \qquad (4.51)$$

in the momentum Equation (4.1) and taking the $\hat{\boldsymbol{\theta}}$ component gives

$$\rho\frac{\partial v_\theta}{\partial t} = \eta\left[\frac{\partial^2 v_\theta}{\partial r^2} + \frac{1}{r}\frac{\partial v_\theta}{\partial r} - \frac{v_\theta}{r^2}\right] + G\frac{\partial\Delta_{r\theta}}{\partial r} + G\frac{2}{r}\Delta_{r\theta}. \qquad (4.52)$$

Upon transformation into dimensionless quantities this becomes

$$\widehat{\rho}q^2\frac{\partial\widehat{v}_\theta}{\partial t} = \epsilon\left[e^{-2q\xi}\frac{\partial^2\widehat{v}_\theta}{\partial\xi^2} - q^2e^{-2q\xi}\widehat{v}_\theta\right] + e^{-q\xi}\frac{\partial\Delta_{r\theta}}{\partial\xi} + 2qe^{-q\xi}\Delta_{r\theta}, \qquad (4.53)$$

where

$$\begin{aligned}
\widehat{\rho} =& \frac{\rho R_1^2}{G\tau_d^2}\\
\epsilon =& \frac{\eta}{G\tau_d} \qquad (4.54)\\
\widehat{v}_\theta =& \frac{v_\theta\tau_d}{qR_1}.
\end{aligned}$$

Although Equation (4.19) implies constant total stress between flat plates, this

is not the case for concentric cylinders due to curvature effects. Writing

$$\mathbf{T} = \begin{pmatrix} T_{rr} & T_{r\theta} \\ T_{r\theta} & T_{\theta\theta} \end{pmatrix}, \tag{4.55}$$

gives

$$\nabla \cdot \mathbf{T} = \nabla \cdot \left[T_{rr}\hat{\mathbf{r}}\hat{\mathbf{r}} + T_{r\theta}\left(\hat{\boldsymbol{\theta}}\hat{\mathbf{r}} + \hat{\mathbf{r}}\hat{\boldsymbol{\theta}}\right) + T_{\theta\theta}\hat{\boldsymbol{\theta}}\hat{\boldsymbol{\theta}} \right], \tag{4.56}$$

which reduces to

$$\nabla \cdot \mathbf{T} = \left[\frac{\partial T_{rr}}{\partial r} + \frac{1}{r}T_{rr} - \frac{1}{r}T_{\theta\theta} \right] \hat{\mathbf{r}} + \left[\frac{\partial T_{r\theta}}{r} + \frac{2}{r}T_{r\theta} \right] \hat{\boldsymbol{\theta}}. \tag{4.57}$$

Then Equation (4.19) implies

$$\frac{\partial T_{r\theta}}{r} + \frac{2}{r}T_{r\theta} = 0 \tag{4.58a}$$

$$\frac{\partial T_{rr}}{\partial r} + \frac{1}{r}T_{rr} - \frac{1}{r}T_{\theta\theta} = 0. \tag{4.58b}$$

Then,

$$\frac{\partial T_{r\theta}}{r} + \frac{2}{r}T_{r\theta} = \frac{\partial}{\partial r}\left(r^2 T_{r\theta}\right) = 0 \tag{4.59}$$

leads to

$$T_{r\theta} = \frac{\Lambda}{r^2}, \tag{4.60}$$

where Λ is a constant of integration, and hence the stress gradient in cylindrical Couette geometry.

Similar to the case of flat plates, the spatial average of each quantity $\diamond$ in cylindrical Couette geometry is computed as

$$\langle \diamond \rangle = \int_0^1 \diamond d\xi, \tag{4.61}$$

which upon use of the transformation Equation (4.34) reduces to

$$\langle \diamond \rangle = \int_{R_1}^{R_2} \diamond \frac{dr}{qr}. \tag{4.62}$$

Taking the zero q limit gives

$$\lim_{q \to 0} r = \lim_{q \to 0} R_1 e^{q\xi} = R_1. \tag{4.63}$$

Hence Equation (4.62) reduces to

$$\langle \diamond \rangle = \int_{R_1}^{R_2} \diamond \frac{dr}{qR_1}. \tag{4.64}$$

Expanding q as a Taylor series about the point R_1 gives

$$q = \frac{(R_2 - R_1)}{R_1} + \mathcal{O}\left((R_2 - R_1)^2\right). \tag{4.65}$$

Hence, Equation (4.64) reduces to

$$\langle \diamond \rangle = \frac{1}{R_2 - R_1} \int_{R_1}^{R_2} \diamond dr. \tag{4.66}$$

In typical experiments where the gap between the plates is small, the stress components and velocity field are taken to vary only in the $\hat{\mathbf{y}}$ direction in the case of flat plates, and $\hat{\mathbf{r}}$ in the case of concentric cylinders. Hence,

$$dr \equiv dy, \tag{4.67}$$

so that Equation (4.66) can then be written as

$$\langle \diamond \rangle = \frac{1}{y_2 - y_1} \int_{y_1}^{y_2} \diamond dy. \tag{4.68}$$

Setting $y_1 = 0$ and choosing by $y_2 = L$ reduces Equation (4.68) to Equation (4.26). Thus, the spatial averages in cylindrical Couette configuration coincide the their counterparts in flat plates in the zero q limit.

4.5 Effects of Stress Diffusivity

The term

$$\frac{d\mathbf{W}}{dt} \equiv \frac{\partial \mathbf{W}}{\partial t} + \mathbf{v} \cdot \nabla \mathbf{W}, \tag{4.69}$$

in the RP model (Equation (4.5)) could lead to situations where $\nabla \mathbf{W}$ contains a delta function if there is a discontinuity in $\mathbf{W}$ [46]. This behaviour of $\mathbf{W}$ would imply a discontinuity in the polymer stress across streamlines [46]. This is unphysical since $\mathbf{W}$ contains information about chain stretch and orientation. A discontinuity in $\mathbf{W}$ would then imply a discontinuity in these quantities. To remove this possible unphysical situation, El-Kareh and Leal [46] used a simple polymer model (dumbbell model) to derive the requirement to remove this unphysical situation. It turned out that stress diffusivity was required to remove the possibility of a discontinuity in the polymer stress.

This stress diffusivity accounts for Brownian motion of the polymer stress across streamlines. This has the effect of smoothening out any discontinuities in the polymer stress [46]. The stress diffusivity can be thought of as relaxation by diffusion of differently strained polymer strands [45].

The question of what physical situations could lead to a jump in $\mathbf{W}$ is readily answered by looking at the behaviour of $\mathbf{W}$ in curved geometries and during shear banding. The shear banding phenomenon leads to inhomogeneities in $\mathbf{W}$ as can be readily seen in Equation (4.2) in the limit of small Reynolds number.

For the case of flat plates, Equation (4.19) implies a constant total stress between the plates. When shear banding occurs, such that $\widehat{\dot{\gamma}}$ becomes inhomogeneous

as in Figure 4.3(b), then Δ_{xy} must become inhomogeneous to maintain a constant total shear stress in Equation (4.23). This inhomogeneity in Δ_{xy} could then lead to a discontinuity in Δ_{xy} if stress diffusivity is neglected.

In the case of concentric cylinders, Equation (4.19) does not necessarily imply a constant total stress as seen in Equation (4.60). But the occurrence of inhomogeneities in $\widehat{\dot{\gamma}}$ during shear banding will still lead to inhomogeneities in $\Delta_{r\theta}$. This is because the stress gradients in Equation (4.60) have no $\widehat{\dot{\gamma}}$ dependence.

The shear banding phenomenon that occurs in a polymeric liquid with a non-monotonic constitutive relation was introduced in Section 2.5. When the applied shear rate satisfies $1/\tau_d < \langle\dot{\gamma}\rangle < 1/\tau_R$, the total shear stress forms a plateau, for example the plateau at $\widehat{T}^0_{xy}$ in Figure 4.3(a). This is because the constitutive relation is multivalued in the unstable part of the constitutive relation as discussed in Section 2.5.

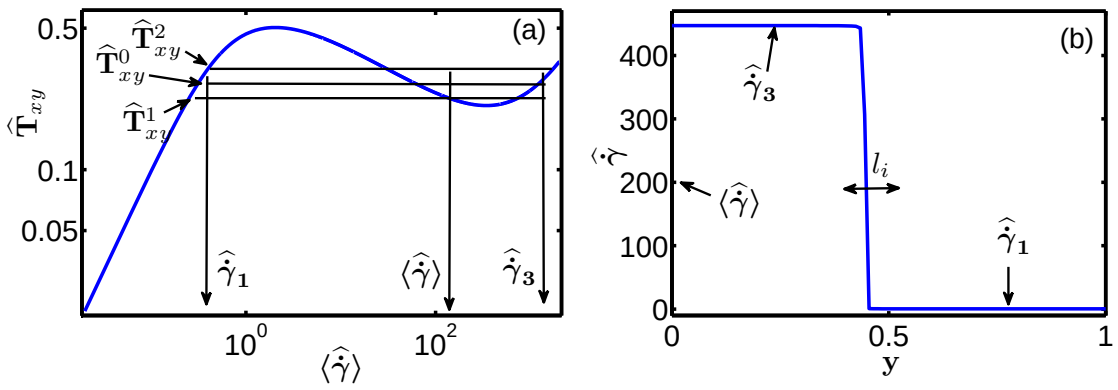

Figure 4.3: (a) Constitutive curve and hypothetical stress plateaus for the DRP model with $\langle\widehat{\dot{\gamma}}\rangle = 200$ and $\widehat{\mathcal{D}} = 10^{-5}$. (b) Corresponding shear rate profile for the applied shear rate in (a).

However, Figure 4.3(a) shows that there are many possible values of $\widehat{T}_{xy}$ which correspond to shear rates $\widehat{\dot{\gamma}}_1$ and $\widehat{\dot{\gamma}}_2$, for an applied shear rate $\langle\widehat{\dot{\gamma}}\rangle$ as indicated in Figure 4.3(a). For example, the shear stresses $\widehat{T}^1_{xy}$ and $\widehat{T}^2_{xy}$ both correspond to the shear rates $\widehat{\dot{\gamma}}_1$, $\langle\widehat{\dot{\gamma}}\rangle$ and $\widehat{\dot{\gamma}}_2$ as shown in Figure 4.3. This situation is unphysical, as experimental data has shown that the selected plateau is unique [50]. The addition

of stress diffusivity [44, 45] removes this unphysical possibility.

Figure 4.3(b) shows the corresponding spatially resolved shear rate profile for the applied spatially averaged shear rate $\langle\widehat{\dot{\gamma}}\rangle = 200$. The values of the spatially resolved shear rate $\widehat{\dot{\gamma}}_1$ and $\widehat{\dot{\gamma}}_2$ which fall in the stable branches of the constitutive curve in Figure 4.3(a) are shown in Figure 4.3(b). They are separated by an interface of width l_i in Figure 4.3(a). The stress diffusion constant sets the value of the width l_i of this interface [44, 45].

4.6 Remarks

The RP model was chosen for this work because it captures the essential physics associated with the behaviour of linear chains under shear deformation and another kind of deformation known as extensional deformation. However, only shear deformation is being considered in this thesis. The RP model contains only the relaxation mode of the whole chain unlike the full GLaMM model which has many relaxation modes down to the relaxation of an entanglement segment. The relaxation time of a segment τ_e is very small, so that the time step required to do numerical simulation of this time scale will be very small, and this will lead to very long simulation times. This single mode RP model which has been shown to give good agreement with experimental data in the past [42, 51] does not have this time constraint. The smallest time scale involved in the RP model is τ_R which is reasonably large for simulations.

Computations with the RP model are difficult because the RP model equation is nonlinear, however the complications with the nonlinearities can be reduced by using semi-implicit finite difference schemes. Explicit schemes would be much easier to code, but they become unstable when the time step is too large. The procedure for implementing a semi-implicit finite difference scheme to the RP model equation will be described in the next chapter.

The equations shown in this chapter were derived from the DRP model equation in two geometries commonly used in experiments: flat plates and concentric cylinders. A third configuration commonly used is the cone and plate arrangement, which is not discussed here. The calculations from the concentric cylinders converge to the case of cone and plate under suitable values of the parameter $q = \ln(R_2/R_1)$. They also converge to the case of flat plates as $q \to 0$. Hence by using sufficiently small values of q such that the calculations become q independent a direct comparison can be made between calculations from concentric cylinders and experimental data from flat plates. To make a direct comparison with the Experiment I described in Chapter 3 which were done with flat plates, the calculations to be presented in Chapter 6 will be done with flat plates. However, there will be a brief discussion of curvature effects on the calculations at the end of Chapter 6.

Chapter 5

Numerical Scheme

The system of partial differential equations derived for the plate configurations in the previous Chapter contains nonlinearities. These kind of coupled system of nonlinear partial differential equations have no analytical solution. It then becomes necessary to employ appropriate numerical techniques in solving these kinds of problems. The numerical schemes used in solving the system of equations encountered in the current study will be described in this chapter. The illustration presented in this chapter is for the case of concentric cylinders, while the approach is the same for the case of flat plates.

5.1 Steady State Solutions

The first step in this study is to investigate the behaviour of the system at steady state when the time derivatives vanish. In the case of flat plates, setting $\widehat{\mathcal{D}} = 0$ in Equation (4.17) ensures spatial homogeneity, but this is not so for the case of concentric cylinders due to the inherent spatial gradients given by Equation (4.60). However, in the limit of $q \to 0$, the condition $\widehat{\mathscr{D}} = 0$ in Equation (4.50) ensures homogeneity in the gap between the cylinders. Then phenomena such as the effect of the CCR parameter in changing the system from a stable to an unstable one

can then be investigated without the complications of spatial inhomogeneities.

In steady state, with $q = 0$ and $\widehat{\mathscr{D}} = 0$ the system of Equations (4.50) become

$$2\hat{\dot{\gamma}}\Delta_{r\theta} - \Delta_{\theta\theta} - \frac{2\tau_d}{\tau_R}\left[1-\widetilde{A}\right]\left[\left(\beta\widetilde{A}+1\right)\Delta_{\theta\theta}+1\right] = 0 \tag{5.1a}$$

$$\hat{\dot{\gamma}}\left[\Delta_{rr}+1\right] - \Delta_{r\theta} - \frac{2\tau_d}{\tau_R}\left[1-\widetilde{A}\right]\left[\beta\widetilde{A}+1\right]\Delta_{r\theta} = 0 \tag{5.1b}$$

$$-\Delta_{rr} - \frac{2\tau_d}{\tau_R}\left[1-\widetilde{A}\right]\left[\left(\beta\widetilde{A}+1\right)\Delta_{rr}+1\right] = 0, \tag{5.1c}$$

which is a system of nonlinear equations. Equations (5.1) can be solved by the Newton algorithm.

5.1.1 Newton algorithm

The Newton algorithm is described in most literature describing solution of systems of equations, for example [52]. The Newton algorithm gives an iterative procedure for solving a system of nonlinear equations. Hence, it is suitable for finding the steady state solution (the solution at long times) of Equation (4.50). This steady state is defined by Equation (5.1).

Consider the system of nonlinear equations given by

$$f_1(u_1, u_2, \ldots, u_m) = 0 \tag{5.2a}$$

$$f_2(u_1, u_2, \ldots, u_m) = 0 \tag{5.2b}$$

$$\vdots$$

$$f_m(u_1, u_2, \ldots, u_m) = 0, \tag{5.2c}$$

where each of the function f_i, $i = 1, 2, \ldots, m$ maps a vector $\mathbf{u} = (u_1, u_2, \ldots, u_m)^T$ of the m dimensional space $\Re^m$ into the real line $\Re$ [52]. Introducing the function

$\mathbf{F}$ which maps $\Re^m$ into $\Re^m$ allows Equation (5.2) to be written as

$$\mathbf{F}(\mathbf{u}) = (f_1(\mathbf{u}), f_2(\mathbf{u}), \ldots, f_m(\mathbf{u}))^T = 0, \tag{5.3}$$

where f_i, $i = 1, 2, \ldots, m$ are the coordinate functions of $\mathbf{F}$. Using an initial condition $\mathbf{u}_0$, the approximate solution of the set of Equations (5.2) at $\mathbf{u}_{n+1}$ is given by the iterative scheme [52]

$$\mathbf{u}_{n+1} = \mathbf{u}_n - \frac{\mathbf{F}(\mathbf{u}_n)}{\mathbf{F}'(\mathbf{u}_n)}, \quad n = 0, 1, 2, \ldots, \tag{5.4}$$

where $\mathbf{F}'(\mathbf{u}_n)$ is the Jacobian matrix at the iterate n.

To solve the nonlinear system of Equations (5.1), one writes

$$f_1(\Delta_{rr}, \Delta_{r\theta}, \Delta_{\theta\theta}) = 0 \tag{5.5a}$$

$$f_2(\Delta_{rr}, \Delta_{r\theta}, \Delta_{\theta\theta}) = 0 \tag{5.5b}$$

$$f_3(\Delta_{rr}, \Delta_{r\theta}, \Delta_{\theta\theta}) = 0, \tag{5.5c}$$

where

$$f_1 = 2\hat{\dot{\gamma}}\Delta_{r\theta} - \Delta_{\theta\theta} - \frac{2\tau_d}{\tau_R}\left[1 - \widetilde{A}\right]\left[\left(\beta\widetilde{A} + 1\right)\Delta_{\theta\theta} + 1\right] \tag{5.6a}$$

$$f_2 = \hat{\dot{\gamma}}\left[\Delta_{rr} + 1\right] - \Delta_{r\theta} - \frac{2\tau_d}{\tau_R}\left[1 - \widetilde{A}\right]\left[\beta\widetilde{A} + 1\right]\Delta_{r\theta} \tag{5.6b}$$

$$f_3 = -\Delta_{rr} - \frac{2\tau_d}{\tau_R}\left[1 - \widetilde{A}\right]\left[\left(\beta\widetilde{A} + 1\right)\Delta_{rr} + 1\right] \tag{5.6c}$$

The solution will then be obtained by performing the iterations,

$$\boldsymbol{\Delta}_{n+1} = \boldsymbol{\Delta}_n - \frac{\mathbf{F}(\boldsymbol{\Delta}_n)}{\mathbf{F}'(\boldsymbol{\Delta}_n)}, \quad n = 0, 1, 2, \ldots. \tag{5.7}$$

The Jacobian matrix $\mathbf{F}'(\mathbf{\Delta}_n)$ at the iterate n is given by:

$$\mathbf{F}'(\mathbf{\Delta}) = \begin{pmatrix} \frac{\partial f_1}{\partial \Delta_{rr}} & \frac{\partial f_1}{\partial \Delta_{r\theta}} & \frac{\partial f_1}{\partial \Delta_{\theta\theta}} \\ \frac{\partial f_2}{\partial \Delta_{rr}} & \frac{\partial f_2}{\partial \Delta_{r\theta}} & \frac{\partial f_2}{\partial \Delta_{\theta\theta}} \\ \frac{\partial f_3}{\partial \Delta_{rr}} & \frac{\partial f_3}{\partial \Delta_{r\theta}} & \frac{\partial f_3}{\partial \Delta_{\theta\theta}} \end{pmatrix}, \tag{5.8}$$

where the function $\mathbf{F}(\mathbf{\Delta})$ is defined by as in Equation (5.3). The iterations are performed using a fixed value of $\hat{\dot{\gamma}}$ until the system converges to a solution. Other values of $\hat{\dot{\gamma}}$ are then used until the desired range of $\hat{\dot{\gamma}}$ is covered.

This method of solution allows the quantity $\Delta_{r\theta}$ to be computed. Taking the shear component of Equation (4.2) and rescaling gives

$$\widehat{T}_{r\theta} = \Delta_{r\theta} + \epsilon\hat{\dot{\gamma}}, \tag{5.9}$$

where $\widehat{T}_{r\theta} = T_{r\theta}/G$. Equation (5.9) then allows $\widehat{T}_{r\theta}$ to be computed from $\Delta_{r\theta}$ calculated by the Newton algorithm. The results of this calculations are shown in Figure 5.1 where the shear stress changes from monotonic to non-monotonic behaviour depending on the value of the CCR parameter used.

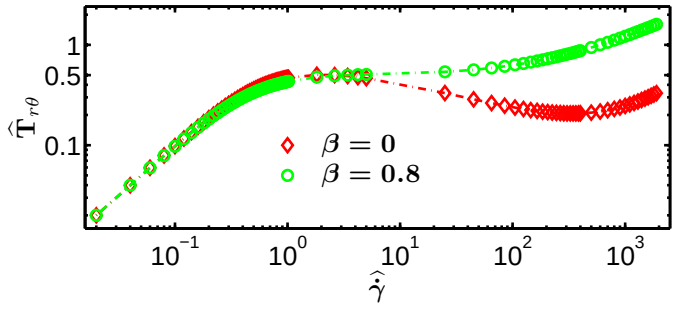

Figure 5.1: Steady state constitutive curves for the RP model for different values of the CCR parameter β for $q = 10^{-10}$, $Z = 72$, calculated from Equation (5.9) using the Newton algorithm.

The red diamonds in figure 5.1 shows the steady state solution for the case of $\beta = 0$ which is non monotonic. However, the green circles in figure 5.1 shows the case for $\beta = 0.8$ which is monotonic.

5.2 Dynamics For a Spatially Homogeneous System

In some situations where it is necessary to study the time evolution of the system in the absence of spatial gradients, the parameters $q = 0$ and $\widehat{\mathscr{D}} = 0$ are used in the set of Equations (4.50). The set of coupled PDEs (4.50) then reduces to a set of coupled ordinary differential equations (ODEs). This set of coupled ODEs can be solved using the 4th order Runge-Kutta scheme (RK4).

5.2.1 4th Order Runge-Kutta Scheme (RK4)

Consider a system of ODEs defined as

$$\frac{du_1}{dt} = f_1(u_1, u_2, \ldots, u_m) \tag{5.10a}$$

$$\frac{du_2}{dt} = f_2(u_1, u_2, \ldots, u_m) \tag{5.10b}$$

$$\vdots$$

$$\frac{du_m}{dt} = f_m(u_1, u_2, \ldots, u_m), \tag{5.10c}$$

which is subject to the initial conditions

$$u_1(0) = u_{1,0} \tag{5.11a}$$

$$u_2(0) = u_{2,0} \tag{5.11b}$$

$$\vdots$$

$$u_m(0) = u_{m,0}, \tag{5.11c}$$

where t is an independent variable. The set of Equations (5.10) and (5.11) can be rewritten as

$$\frac{du_i}{dt} = f_i(u_1, u_2, \ldots, u_m) \tag{5.12a}$$

$$u_i(0) = u_{i,0}, \quad i = 1, 2, \ldots, m. \tag{5.12b}$$

The RK4 scheme gives the solution to the system of ODEs defined by Equation (5.12) as

$$\mathbf{u}_{n+1} = \mathbf{u}_n + \frac{1}{6}\left[\mathbf{\Gamma} + 2\mathbf{\Xi} + 2\mathbf{\Pi} + \mathbf{\Psi}\right], \tag{5.13}$$

where

$$\mathbf{\Gamma} = \delta t \mathbf{F}\left(\mathbf{u}_n\right) \tag{5.14a}$$

$$\mathbf{\Xi} = \delta t \mathbf{F}\left(\mathbf{u}_n + \frac{1}{2}\mathbf{\Gamma}\right) \tag{5.14b}$$

$$\mathbf{\Pi} = \delta t \mathbf{F}\left(\mathbf{u}_n + \frac{1}{2}\mathbf{\Xi}\right) \tag{5.14c}$$

$$\mathbf{\Psi} = \delta t \mathbf{F}\left(\mathbf{u}_n + \frac{1}{2}\mathbf{\Pi}\right), \tag{5.14d}$$

where the independent variable t has been discretized with step size δt and index n, and the corresponding values of the dependent variables $\mathbf{u}$ have index n. The function $\mathbf{F}$ has the same meaning as in Equation (5.3).

The RK4 scheme is easily applied to the set of Equations (4.50) with $q = 0$ and $\widehat{\mathscr{D}} = 0$ by making the following identifications,

$$u_1' \equiv \frac{d\Delta_{\theta\theta}}{dt} \tag{5.15a}$$

$$u_2' \equiv \frac{d\Delta_{r\theta}}{dt} \tag{5.15b}$$

$$u_3' \equiv \frac{d\Delta_{rr}}{dt} \tag{5.15c}$$

and

$$f_1(u_1,u_2,u_3) \equiv 2\hat{\dot{\gamma}}\Delta_{r\theta} - \Delta_{\theta\theta} - \frac{2\tau_d}{\tau_R}\left[1-\widetilde{A}\right]\left[\left(\beta\widetilde{A}+1\right)\Delta_{\theta\theta}+1\right] \tag{5.16a}$$

$$f_2(u_1,u_2,u_3) \equiv \hat{\dot{\gamma}}\left[\Delta_{rr}+1\right] - \Delta_{r\theta} - \frac{2\tau_d}{\tau_R}\left[1-\widetilde{A}\right]\left[\beta\widetilde{A}+1\right]\Delta_{r\theta} \tag{5.16b}$$

$$f_3(u_1,u_2,u_3) \equiv -\Delta_{rr} - \frac{2\tau_d}{\tau_R}\left[1-\widetilde{A}\right]\left[\left(\beta\widetilde{A}+1\right)\Delta_{rr}+1\right] \tag{5.16c}$$

5.3 Spatially Inhomogeneous System

When the constraints of $q = 0$ and $\widehat{\mathscr{D}} = 0$ are lifted in the cylindrical Couette geometry, the system becomes spatially inhomogeneous. Hence, the full set of Equations (4.50) needs to be solved with $q \neq 0$ and $\widehat{\mathscr{D}} \neq 0$. This requires a numerical scheme suitable for solving a system of coupled partial differential equations. The numerical scheme employed for this purpose is described in the following subsection.

5.3.1 Backward Implicit Scheme (BIS)

To obtain the time evolution of the system from startup to steady state, the full set of Equations (4.50) is solved using the BIS. The Equations (4.50) are of the form

$$\frac{\partial U}{\partial t} = \frac{\partial^2 U}{\partial x^2} + f(U), \tag{5.17}$$

where U is an arbitrary function and f is an arbitrary function of U. To simplify the analysis, consider the case of $f = 0$. Then Equation (5.17) becomes

$$\frac{\partial U}{\partial t} = \frac{\partial^2 U}{\partial x^2}. \tag{5.18}$$

The finite difference method involves forming the discretised versions of the time and space derivatives in Equation (5.18). In the BIS, the time and space derivatives are given as [53, 54]

$$x \approx j\delta x, \quad j = 1, 2, 3, \ldots \tag{5.19a}$$

$$t \approx n\delta t, \quad n = 1, 2, 3, \ldots \tag{5.19b}$$

$$U(x,t) \approx U(x_j, t_n) \equiv U_{j,n} \tag{5.19c}$$

$$\frac{\partial U}{\partial t} \approx \frac{1}{\delta t}\left[U_{j,n+1} - U_{j,n}\right] \tag{5.19d}$$

$$\frac{\partial^2 U}{\partial x^2} \approx \frac{1}{(\delta x)^2}\left[U_{j+1,n+1} - 2U_{j,n+1} + U_{j-1,n+1}\right]. \tag{5.19e}$$

Then substitution into Equation (5.18) gives

$$\left(1 + \frac{2\delta t}{(\delta x)^2}\right) U_{j,n+1} - \frac{\delta t}{(\delta x)^2}\left[U_{j+1,n+1} + U_{j-1,n+1}\right] = U_{j,n}. \tag{5.20}$$

A finite difference approximation such as Equation (5.20) is said to converge to the true solution $\overline{U}$ of Equation (5.18) if it meets the requirement [54]

$$\left\|\overline{U}_{j,n} - U_{j,n}\right\| \to 0 \quad \text{as} \quad \delta x, \delta t \to 0, \tag{5.21}$$

where $\|.\|$ is some suitable norm between the exact value of $\overline{U}(x,t)$ and the computed value $U_{j,n}$ at some fixed point j, n. Hence the finite difference approximation can be brought closer to the true solution by refining the mesh. However, since the true solution is not known before hand, the convergence is inferred from the Lax equivalence theorem. This theorem states that if a finite difference scheme is **consistent**, then its **stability** is the necessary and sufficient condition for convergence [54].

The consistency of a finite difference scheme has to do with the truncation errors associated with the construction of the time and space derivatives [54]. A

finite difference scheme is consistent if the truncation errors go to zero as δx, δt go to zero. In this case, the finite difference scheme actually approximates the desired PDE and not some other PDE [54]. The truncation errors associated with the BIS vanish as δx, $\delta t \to 0$ [54], hence the BIS is consistent.

The stability of a finite difference approximation has to do with the unstable growth or stable decay of errors in the arithmetic operations needed to solve the finite difference equations themselves. This has nothing to do with the PDE, the errors are due to round-off errors from the computer [54]. The errors which occur in the solution of the BIS equation decay with time for all values of δx and δt. Thus the BIS is stable for large time steps [54].

Since the BIS is consistent and unconditionally stable (stable for all values of δx, δt), then the BIS is convergent by the Lax equivalent theorem. However, the BIS is first order accurate in time so that the rate of convergence is slow. To increase the rate of convergence the average values of the spatial discretisations at two time steps will be used in the calculations to follow.

5.3.2 Calculating Stress Using BIS

The BIS is implemented in Equation (4.50) using

$$\xi \approx j\delta\xi, \quad j = 1, 2, \ldots, X_n \tag{5.22a}$$

$$t \approx n\delta t, \quad n = 1, 2, \ldots, T_n \tag{5.22b}$$

$$\widehat{\dot{\gamma}}(\xi, t) \approx \widehat{\dot{\gamma}}_{j,n} \tag{5.22c}$$

$$\Delta_{\theta\theta}(\xi, t) \approx \Delta_{\theta\theta}^{j,n} \tag{5.22d}$$

$$\Delta_{r\theta}(\xi, t) \approx \Delta_{r\theta}^{j,n} \tag{5.22e}$$

$$\Delta_{rr}(\xi, t) \approx \Delta_{rr}^{j,n} \tag{5.22f}$$

$$\left(1 + \frac{\Delta_{\theta\theta}(\xi, t) + \Delta_{rr}(\xi, t)}{3}\right)^{-1/2} \approx \left(1 + \frac{\Delta_{\theta\theta}^{j,n} + \Delta_{rr}^{j,n}}{3}\right)^{-1/2}, \tag{5.22g}$$

where X_n is the number of spatial points and T_n is the number of time steps. The zero gradient boundary conditions on $\mathbf{\Delta}$ give

$$\Delta_{rr}^{1,n+1} = \Delta_{rr}^{2,n+1} \tag{5.23a}$$

$$\Delta_{rr}^{X_n-1,n+1} = \Delta_{rr}^{X_n,n+1}, \tag{5.23b}$$

and similarly for the other components of $\mathbf{\Delta}$. The time and space discretisations for the case of Δ_{rr} take the form

$$\frac{\partial \Delta_{rr}}{\partial t} \approx \frac{1}{\delta t}\left[\Delta_{rr}^{j,n+1} - \Delta_{rr}^{j,n}\right] \tag{5.24a}$$

$$\frac{\partial^2 \Delta_{rr}}{\partial \xi^2} \approx \frac{1}{2(\delta\xi)^2}\left[\Delta_{rr}^{j+1,n+1} - 2\Delta_{rr}^{j,n+1} + \Delta_{rr}^{j-1,n+1}\right] + \frac{1}{2(\delta\xi)^2}\left[\Delta_{rr}^{j+1,n} - 2\Delta_{rr}^{j,n} + \Delta_{rr}^{j-1,n}\right], \tag{5.24b}$$

where the spatial derivatives have been averaged at the two time steps n and $n+1$ to increase the rate of convergence. The time and space discretizations for $\Delta_{r\theta}$ and $\Delta_{\theta\theta}$ are similar to the case of Δ_{rr} as given in Equation (5.24).

The initial conditions are implemented as

$$\widehat{\dot{\gamma}}(\xi, 0) \approx \widehat{\dot{\gamma}}_{j,0} \tag{5.25a}$$

$$\Delta_{rr}(\xi, 0) \approx \Delta_{rr}^{j,0} \tag{5.25b}$$

$$\left(1 + \frac{\Delta_{rr}(\xi,0) + \Delta_{\theta\theta}(\xi,0)}{3}\right)^{-1/2} \approx \left(1 + \frac{\Delta_{rr}^{j,0} + \Delta_{\theta\theta}^{j,0}}{3}\right)^{-1/2}. \tag{5.25c}$$

The boundary conditions for the stress were obtained by using the anchoring potential analogy used in [23]. In this analogy, the viscoelastic stress is connected to an anchoring potential $\mathscr{W}$ as follows:

$$\mathscr{D}\tau\hat{\mathbf{n}} \cdot \nabla\mathbf{\Delta} + \mathscr{W}(\mathbf{\Delta} - \mathbf{\Delta_o}) = 0. \tag{5.26}$$

Here, $\hat{\mathbf{n}}$ is a unit normal to the wall and $\mathscr{W}$ is the anchoring potential. For a weak anchoring potential Equation (5.26) reduces to:

$$\hat{\mathbf{n}} \cdot \nabla \boldsymbol{\Delta} = 0, \tag{5.27}$$

which gives

$$\frac{\partial \Delta}{\partial \xi} = 0 \quad (\text{at} \quad \xi = 0) \tag{5.28a}$$

$$\frac{\partial \Delta}{\partial \xi} = 0 \quad (\text{at} \quad \xi = 1). \tag{5.28b}$$

Hence zero gradient boundary condition is used for the calculation of the stress components.

5.3.3 Calculating the Velocity Field Using BIS

Similar to the case of $\boldsymbol{\Delta}$, the BIS applied to the momentum Equation (4.53) gives

$$\widehat{v}(\xi, t) \approx \widehat{v}_{j,n} \tag{5.29a}$$

$$\Delta_{r\theta}(\xi, t) \approx \Delta_{r\theta}^{j,n} \tag{5.29b}$$

$$\frac{\partial \Delta_{r\theta}}{\partial \xi} \approx \frac{1}{4\delta\xi}\left[\Delta_{r\theta}^{j+1,n+1} - \Delta_{r\theta}^{j-1,n+1}\right] + \frac{1}{4\delta\xi}\left[\Delta_{r\theta}^{j+1,n} - \Delta_{r\theta}^{j-1,n}\right] \tag{5.29c}$$

$$\frac{\partial \widehat{v}}{\partial t} \approx \frac{1}{\delta t}\left[\widehat{v}_{j,n+1} - \widehat{v}_{j,n}\right] \tag{5.29d}$$

$$\frac{\partial^2 \widehat{v}}{\partial \xi^2} \approx \frac{1}{2(\delta\xi)^2}\left[\widehat{v}_{j+1,n+1} - 2\widehat{v}_{j,n+1} + \widehat{v}_{j-1,n+1}\right] + \frac{1}{2(\delta\xi)^2}\left[\widehat{v}_{j+1,n} - 2\widehat{v}_{j,n} + \widehat{v}_{j-1,n}\right], \tag{5.29e}$$

where $\widehat{v}_\theta$ in Equation (4.53) has been written as $\widehat{v}$ for simplicity. The no slip boundary conditions in Equation (4.36) give

$$\widehat{v}_{1,n} = \widehat{\mathscr{V}} \tag{5.30a}$$

$$\widehat{v}_{X_n,n} = 0, \tag{5.30b}$$

where the moving inner cylinder is indexed $j = 1$, while the stationary outer cylinder is indexed $j = X_n$. Equation (4.39) shows that

$$\widehat{\mathscr{V}} = -\langle\widehat{\dot{\gamma}}\rangle, \tag{5.31}$$

where $\langle\widehat{\dot{\gamma}}\rangle$ is the imposed averaged shear rate. The initial condition is implemented as

$$\widehat{v}_{j,0} = \widehat{v}_{j0,0}, \quad j = 2, 3, \ldots, X_n - 1. \tag{5.32}$$

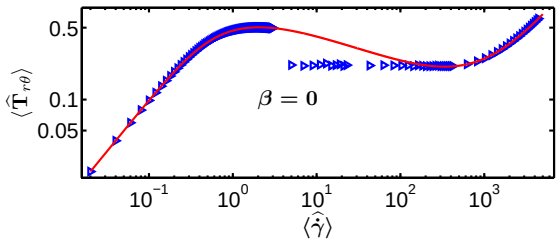

Figure 5.2: Flow curve (triangles) for the DRP model for $\beta = 0$ calculated from Equation (4.50) using the BIS. The solid line shows the constitutive curve calculated by the Newton algorithm.

The spatially resolved shear rate is obtained by discretising Equation (4.31) whose dimensionless form is given as

$$\widehat{\dot{\gamma}} = e^{-q\xi}\left[\frac{\partial\widehat{v}_\theta}{\partial\xi} - q\widehat{v}_\theta\right], \tag{5.33}$$

where q is defined in Equation (4.34). Once $\widehat{\dot{\gamma}}$ is calculated at the first time step,

then Equation (4.50) can be evolved one time step forward. The average total shear stress at the first time step is obtained by taking the average of Equation (5.9) as

$$\langle \hat{T}_{r\theta} \rangle(1) = \langle \Delta_{r\theta} \rangle(1) + \epsilon \langle \widehat{\dot{\gamma}} \rangle. \tag{5.34}$$

This process is repeated at subsequent time steps until the time evolution of the average total shear stress is obtained.

The steady state of the system is determined by defining a tolerance ς which serves as an upper bound for subsequent values of the average total shear stress. Then to determine steady state, a suitable range of $\langle \hat{T}_{r\theta} \rangle$ is chosen such that when the condition

$$\left| \langle \hat{T}_{r\theta} \rangle(2n) - \langle \hat{T}_{r\theta} \rangle(n) \right| < \varsigma \tag{5.35}$$

is satisfied, then $\langle \hat{T}_{r\theta} \rangle$ is said to have reached steady state. A suitable value of ς can be determined by comparing the steady state value of $\langle \hat{T}_{r\theta} \rangle$ with another steady value of $\langle \hat{T}_{r\theta} \rangle$ obtained with a smaller value of ς. The values of ς are decreased until a consistent steady value of $\langle \hat{T}_{r\theta} \rangle$ is obtained for a given $\langle \widehat{\dot{\gamma}} \rangle$. Then the value of $\langle \widehat{\dot{\gamma}} \rangle$ is increased and a new steady value of $\langle \hat{T}_{r\theta} \rangle$ is obtained. This process is repeated until the desired range of $\langle \widehat{\dot{\gamma}} \rangle$ is covered. The result which is known as the flow curve is shown by the blue triangles in Figure 5.2.

5.4 Choice of Parameters

The parameters used in these calculations were chosen to be consistent with typical experimental data. The value $Z = 72$ lies in the range of data reported in [4]. The solvent viscosity $\eta \approx 1\text{Pa}\,\text{s}$, $\tau_d = 310\,s$ [4] and $G \approx 7 \times 10^3$ [55] gives $\epsilon \approx 10^{-7}$. However, fitting the constitutive curve from the RP model with the experimentally measured constitutive curve in [29] give estimates of $\epsilon \approx 10^{-4}$. Hence $\epsilon = 10^{-4}$ was used. The results from the simulations do not change qualitatively at smaller values

of ϵ but they require smaller time steps due to scaling problems in the coefficient matrix associated with the finite difference Equation (5.20). This value of $\epsilon = 10^{-4}$ allows the use of large time steps in the simulations.

For the case of concentric cylinders, typical values of q lie in the range $(2 \times 10^{-3}, 2 \times 10^{-4})$ [25]. However, because the calculations become independent of system curvature below $q = 10^{-6}$ a value of $q = 10^{-10}$ was used to match experimental data from [4]. In the case of concentric cylinders, it is not possible to go to the $q = 0$ limit because of the transformation $\xi = (1/q)\ln(r/R_1)$. However, repeating the calculations in the case of flat plates (which corresponds to the $q = 0$ limit) using the same initial conditions give exactly the same results as the case of concentric cylinders with $q = 10^{-10}$. Using $R_1 = 16\text{mm}$ [35], $\rho \approx 10^3\,\text{kg}\,\text{m}^{-3}$ gives $\hat{\rho} \approx 3 \times 10^{-10}$ so that $\hat{\rho} = 10^{-10}$ was used in the calculations for concentric cylinders. Finally, $\widehat{\mathcal{D}} = 10^{-5}$ in the case of flat plates to match experimental data of [4], and $\widehat{\mathscr{D}} = 10^{-5}$ for the case of concentric cylinders to study curvature effects on the calculations. The value of $\widehat{\mathcal{D}}$ or $\widehat{\mathscr{D}}$ used in the simulations puts a restriction on the spatial width of the mesh used. The width of the interface between shear bands indicated as l_i in Figure 4.3(b) is set by the value of $\widehat{\mathscr{D}}$ as $l_i \sim \sqrt{\widehat{\mathscr{D}}}$ [23]. The scale of stress diffusion constant used in the simulations is typical of polymer solutions [23].

Although a value of $q = 10^{-10}$ was used in the calculation with concentric cylinders to match the flat plates data of [29], the 'fracture' effect is still possible with $q \neq 0$. The effect of the curvature parameter on the calculations will be discussed in the next Chapter.

5.5 Test For Convergence

To ensure that the solutions obtained from the numerical scheme actually converged to the true solution, the calculations were repeated with smaller values of δt and $\delta\xi$

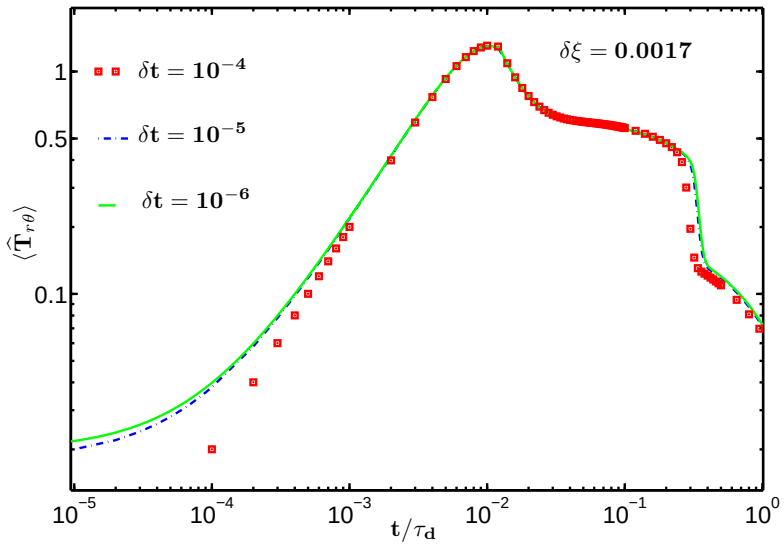

Figure 5.3: Shear stress during startup and relaxation after a step strain for strain amplitude $\gamma_0 = 2.5$. The average total shear stress is calculated from Equation (5.9) using the BIS for a mesh of 600 grid points X_n ($\delta\xi = 1/X_n \simeq 1.7 \times 10^{-3}$) for the time steps δt shown. The profiles begin to converge to some limiting value as δt decreases. [Parameters: $\langle \widehat{\dot{\gamma}} \rangle = 200$, $\widehat{\mathscr{D}} = 10^{-5}$, $Z = 72$, $\widehat{\rho} = 10^{-10}$, $q = 10^{-10}$]

(starting from suitable initial values) until nearly constant results were obtained. The choice of parameters to perform the test is very important. In the current work, the test was carried out when the shear stress was relaxing rapidly following a large step shear. During this interval, the velocity profile also changes very rapidly in space and time, and thus the solutions are most vulnerable to errors in this interval. The velocity profile also develops sharp spatial gradients in this interval which may lead to jumps in the spatial profile of the velocity.

To obtain the desired shear stress and velocity profiles, Equation (4.50) was initialised with random perturbations. These perturbations will be described in Chapter 6. The shear stress and velocity profiles obtained using meshes of different number of grid points X_n are shown in Figures 5.3 to 5.6. The value of $\delta\xi$ decreases as the number of grid points is increased since $\delta\xi = 1/X_n$. The Figures also show the results for different values of δt. The results show that the velocity profile and shear stress begin to converge to some limiting value as both $\delta\xi$ and δt are decreased.

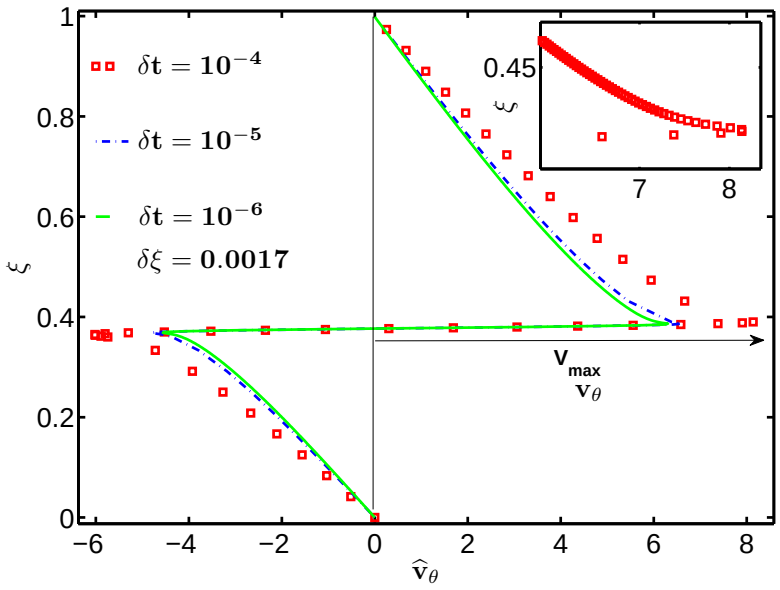

Figure 5.4: Velocity profiles during stress relaxation after a step strain calculated from Equation (5.35) for a mesh of 600 grid points X_n ($\delta x = 1/X_n \simeq 1.7 \times 10^{-3}$). The profiles converge as δt decreases. Parameters same as Figure 5.3.

Also the inset of Figure 5.4 shows that the velocity profiles change smoothly around the regions of strong spatial gradients. All the computations were done in MATLAB®. All the results presented in this thesis were computed using $\delta t = 10^{-5}$ and $\delta x = 10^{-3}$. These values of δt and δx require creation of large arrays which require large amounts of computer memory, and the simulations run into hours. Hence the computations were done using the advanced research computing (ARC) infrastructure of the University of Leeds whose configuration is described in [56].

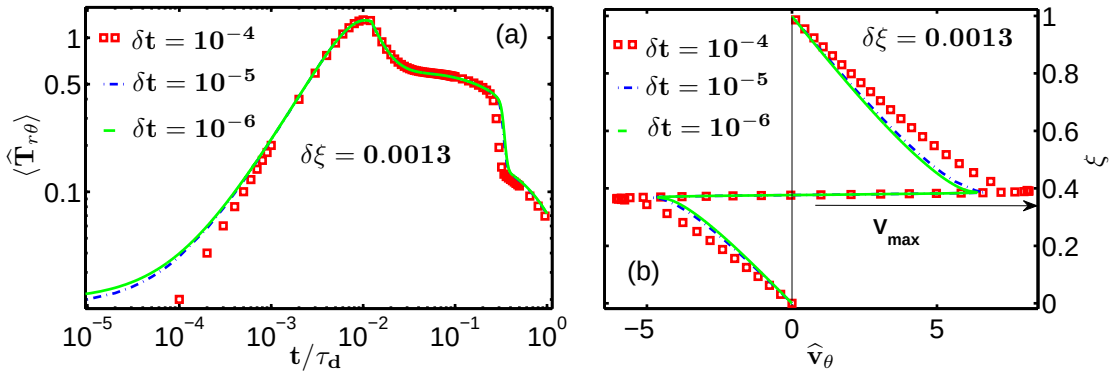

Figure 5.5: Same as Figures 5.3 and 5.4 with a mesh of 800 grid points.

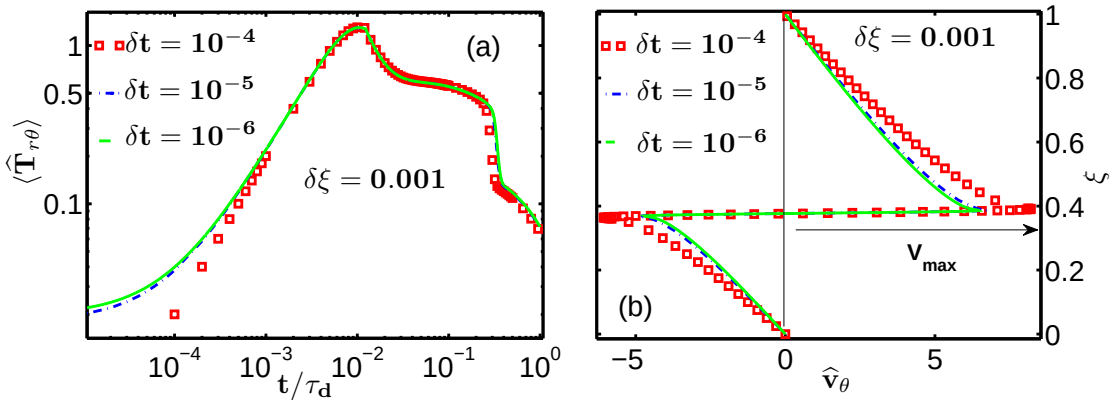

Figure 5.6: Same as Figures 5.3 and 5.4 with a mesh of 1000 grid points.

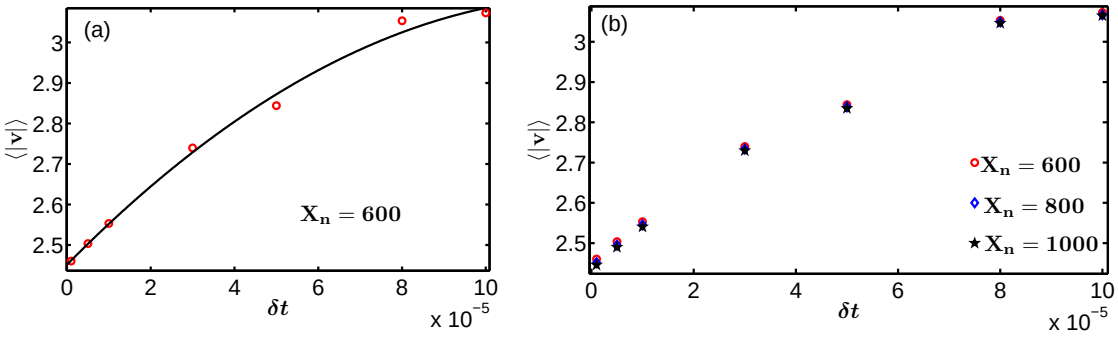

Figure 5.7: Data showing convergence of calculations as mesh size increases and time step decreases.

Most of the computations were done with a single processor since the process of distributing the arrays among many processors resulted in too much communication overhead among the processors. However, the calculation of the free energy (Equation (2.22)) does not involve communication between processors. In this case, it is possible to split the loop index among different processors and the calculations done in parallel. This was achieved using the Parallel Computing Toolbox™ of MATLAB® using its default settings which allows a maximum of eight labs (processors). All eight labs were used in this case.

As a mean of quantifying the behaviour of of the velocity profiles for different values of $\delta\xi$ and δt, the quantity $\langle |\mathbf{v}| \rangle$ defined as

$$\langle |\mathbf{v}| \rangle = \frac{1}{X_n} \sum_i |v_i|, \tag{5.36}$$

(where the sum is over all spatial position) is computed for different values of $\delta\xi$ and δt. The results are shown in Figures 5.7(ab). Figure 5.7(a) shows that the percentage change of $\langle|\mathbf{v}|\rangle$ reduces to about 4% as the time step is reduced to $\delta t = 10^{-6}$. The data nearly fits a quadratic, which shows that the convergence is faster than linear. The quadratic behaviour is more prominent at the larger time steps. Figure 5.7(b) shows a similar situation for $X_n = 800$ and $X_n = 1000$.

5.6 Remarks

All the calculations presented in this Chapter are based on the geometry of concentric cylinders for the purpose of illustrating the application of the numerical schemes used in this work. The same procedure is used in the case of flat plates. No attempt has been made to make a direct comparison with the experimental data of [4] since they were done with flat plates. In chapters 6 and 7 where the calculations were done with flat plates, there will be comparisons with the data of [4]. Figures 5.3 to 5.6 show that the calculations converge as the time and spatial resolutions increase, which shows that the results from the numerical scheme are real solutions of the DRP equation and not some artifact from the mesh.

The use of the semi-implicit finite difference scheme allows the use of large time steps to quickly get results without running into difficulties of instability associated with explicit schemes. However, to get trusted (converged) calculations, a small time step and finner mesh is used.

Chapter 6

Modelling Fracture

The previous Chapter illustrated the numerical schemes used in solving the equations encountered in Chapter 4. The key results of the calculations in the flat plate geometry will be presented in this Chapter, while a detailed study of the effect of the perturbations is deferred to Chapter 7. There will also be a brief discussion of curvature effects on the calculations.

When polymeric liquids are subjected to fast shear deformation such that the applied shear rate $\langle\dot{\gamma}\rangle$ satisfies $\langle\dot{\gamma}\rangle\tau_d > 1$, then the total shear stress given in Equation (4.23) grows from startup through a maximum (or stress overshoot), and finally relaxes to some steady value. The stress overshoot for $\langle\widehat{\dot{\gamma}}\rangle = \langle\dot{\gamma}\rangle\tau_d = 200$ is shown in Figure 6.1(a). The overshoot stress $\hat{T}_{xy}^{ov}$ and strain for overshoot γ_{ov} are indicated in the Figure. The overshoot stress varies with applied shear rate as indicated by the green squares in Figure 6.1(b). For $1 < \widehat{\dot{\gamma}} < 1/\tau_R$[1], the shear stress relaxes to a plateau after the stress overshoot as shown by the black dashed lines in Figure 6.1(b). This situation only occurs when the constitutive relation is non-monotonic as shown by the solid line in Figure 6.1(b).

The Rolie Poly model yields either a monotonic or non-monotonic behaviour depending on how much Convective Constraint Release (CCR) is allowed in the

[1]The stretch relaxation time τ_R has been made dimensionless as defined in Equation (4.16).

system, as set with the CCR parameter β. This is shown by the curves in Figure 5.1 for $\beta = 0$ and $\beta = 0.8$. The constitutive relation shown by the red solid line in Figure 6.1(b) is the case of $\beta = 0$.

The 'fracture' phenomenon as seen in experiments has already been described in Section 3.2. This discussion now proceeds with a description of the procedure employed in capturing this fracture-like behaviour. The calculations will be based on Experiment I described in Sub section 3.2.1.

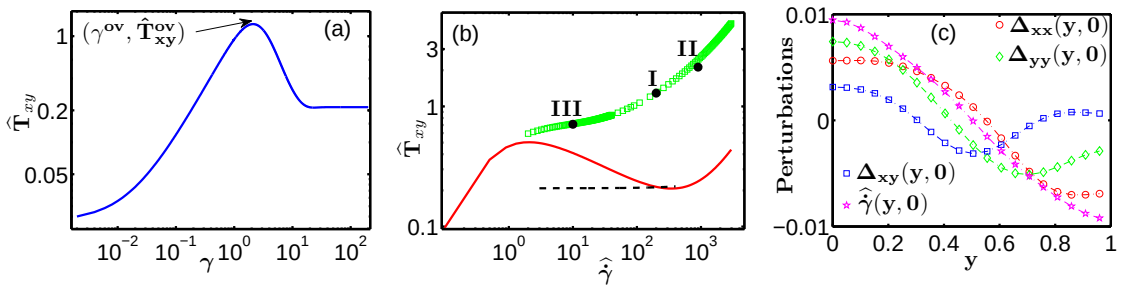

Figure 6.1: (a) Shear stress from startup, evolving through a maximum (overshoot) then towards steady state for $\langle\hat{\dot{\gamma}}\rangle = 200$. The overshoot stress and strain are indicated by the arrow. (b) Green squares: overshoot stress at different imposed shear rates. Red solid line: Steady state constitutive curve for the Rolie-Poly (RP) model at $\beta = 0$ showing nonmonotonic behaviour. Black dashed lines: Flow curve of the DRP, for $\beta = 0$. The labels I, II and III are the stresses at t_0 for the Cases I, II and III as described in the text.(c) Random perturbations used to initialise the system for the calculations in this Chapter. The initial condition for each of the quantities $\hat{\dot{\gamma}}$, Δ_{xx}, Δ_{xy} and Δ_{yy} are indicated. Parameters: $Z = 72$, $\beta = 0$ and $\nu = 0.01$.

To capture the behaviour reported in [4], Equation (4.17) is initialised [2] with random perturbations of the form

$$\delta\mathbf{u}(0, y) = \nu \sum_{n=1}^{5} (\mathbf{A}_n/n^2)\cos(n\pi y), \tag{6.1}$$

where $\mathbf{u} \equiv [\hat{\dot{\gamma}}, \Delta_{xx}, \Delta_{xy}, \Delta_{yy}]$. The vectors $\mathbf{A}_n$ contain the amplitudes of the perturbations used to initialise each of the quantities in $\mathbf{u}$. The components A_{ni} of

[2]For the remaining part of this thesis, all the calculations will be done using the set of Equations (4.17) since the Cartesian coordinates system is consistent with the flat plates used in the experiments [4]. However, there will be a brief presentation of curvature effects on the calculations at the end of this Chapter.

each vector is chosen randomly from the interval $[-1, 1]$. The index $i = 1, 2, 3, 4$ corresponds to each of the quantity $[\widehat{\dot{\gamma}}, \Delta_{xx}, \Delta_{xy}, \Delta_{yy}]$. The parameter ν sets the scale of the amplitude [57], the value $\nu = 0.01$ is consistent with the scale of typical thermal fluctuations [26, 57]. High wavenumbers n are suppressed by spatial gradients in $\mathbf{\Delta}$ [57, 58, 59] hence the $1/n^2$ penalty on the amplitudes A_{ni}. The cosine modes satisfy the zero gradient boundary condition imposed on $\mathbf{\Delta}$.

The system is started with a randomly chosen perturbation at a given applied shear rate $\langle\widehat{\dot{\gamma}}\rangle$, and the flow is switched off at some time t_0[3] during which the system suffers some strain $\gamma_0 = \langle\widehat{\dot{\gamma}}\rangle t_0$. Different random perturbations give rise to different velocity profiles after shear cessation at t_0. In 300 simulations using different random perturbations [4], about 34% of the resultant velocity profiles were similar to the cases reported in [4] (as shown in Figure 3.3) for an applied shear rate $\langle\widehat{\dot{\gamma}}\rangle = 200$ and strain $\gamma_0 = 2.5$.

As noted in earlier discussions, when the applied shear rate is such that $\langle\widehat{\dot{\gamma}}\rangle\tau_R > 1$[5], then the chains suffer significant stretch. Also, when $\langle\dot{\gamma}\rangle\tau_d > 1$ the total shear stress passes through an overshoot before relaxing to some steady value. The stress overshoot is an indication of an elastic instability as discussed earlier [16, 18].

Hence, deformations in which $\langle\widehat{\dot{\gamma}}\rangle\tau_R < 1$ will be referred to as slow or low shear rate, while the case of $\langle\widehat{\dot{\gamma}}\rangle\tau_R > 1$ will be fast deformation or high shear rate. Also, deformations in which shearing is stopped before the stress overshoot will be referred to as low strain. When shearing is stopped after the stress overshoot, such deformation will be referred to as high strain. This will allow possible effects of chain stretch and elastic effects on 'fracture' to be studied.

Thus, using a set of perturbation (shown in Figure 6.1(c)) which are known to give a fracture like profile, the different cases reported in [4] are simulated.

[3]The time t is dimensionless as defined in Equation (4.16)
[4]See Chapter 7 for a more detailed discussion of the perturbations.
[5]Recall that $\tau_d/\tau_R = 3Z$.

6.1 Case I: Intermediate Shear Rate, High Strain

In this case, the applied shear rate $\langle\widehat{\dot{\gamma}}\rangle = 200$ gives $\langle\widehat{\dot{\gamma}}\rangle\tau_R \simeq 0.93 \simeq 1$ and the applied strain $\gamma_0 = 2.5 > \gamma_{ov} \approx 2.1$, where γ_{ov} is the strain for stress overshoot. The total shear stress at t_0 for this Case is indicated by I in Figure 6.1(b). This implies that the shear stress satisfies $\partial T_{xy}/\partial\gamma < 0$, which is the requirement for elastic instability. The velocity profile is nearly perfectly homogeneous just before shear cessation at t_0^-, as shown in the inset of Figure 6.2(a); this is similar to the experimental data shown in the inset of Figure 6.3. However, just after shear cessation at t_0^+, the velocity profile is nearly zero except with a slight inhomogeneity due to the initial perturbation as shown in Figure 6.2(a). Subsequently, it begins to show recoil before developing a fracture-like profile with a so called 'failure plane' separating two layers of fluid moving in opposite directions, as shown in Figure 6.2(a). This is similar to the experimental data shown in Figures 6.2(b) and 6.3. Figure 6.2(b) are the velocity profiles at various times after shear cessation for the material SBR of molecular weight $250000\,\mathrm{g\,mol^{-1}}$ labelled SBR250K. In this case, the SBR250K was subjected to a strain amplitude $\gamma_0 = 2.1$ and shear rate $\dot{\gamma} = 0.7\,\mathrm{s^{-1}}$, whereupon after shear cessation it developed a fracture-like profile [4]. The location of the 'failure plane' is sensitive to the initial conditions whereas the stress relaxation profile is not. This is similar to the report in [4] that the location of the 'failure plane' changes in different runs of the experiment whereas the stress relaxation profile does not.

Figure 6.2(a) also shows dimensionless data taken from Figure 6.2(b) at the time $t - t_0 = 32.5$s. The experimental data was made dimensionless using $\tau_d = 310$s for SBR250K [4] and a gap size of 0.7mm [4]. The velocity profile at the time $t - t_0 = 32.5$s is indicated as V_{max} in Figure 6.2(b). This experimentally determined velocity profile at $t - t_0 = 32.5$s shows very good qualitative match with the calculations in Figure 6.2(a). However, the magnitude of the largest velocity profile from the

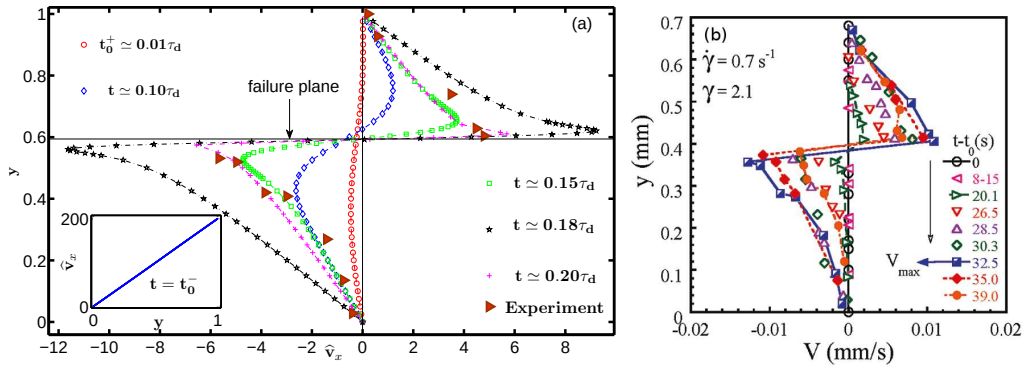

Figure 6.2: (a) Velocity profiles just after shear cessation at t_0^+ and during 'fracture'. The 'failure plane' indicated in the Figure is a horizontal plane perpendicular to the plane of the Figure separating the regions where the fluid moves in opposite direction. The inset shows the velocity profile just before shear cessation at t_0^-. The filled triangles are dimensionless experimental data at the time $t - t_0 = 32.5$s from (b) for direct comparison with calculations. Parameters: $\langle\dot{\hat{\gamma}}\rangle = 200$, $\gamma_0 = 2.5$, $Z = 72$, $\beta = 0$ and $\nu = 0.01$. (b) Experimental data for SBR250K showing velocity profiles after shear cessation and various times afterwards, Figure from [4].

calculation in Figure 6.2(a) is nearly twice the magnitude of the dimensionless (experimentally determined) velocity profile in Figure 6.2(a). Hence predictions from the theoretical model are mostly qualitative than quantitative.

Figure 6.3 shows the displacement of tracked particles during the experiment for SBR250K for different strain amplitudes. For the low strain amplitudes of $\gamma_0 = 0.1$ and $\gamma_0 = 0.7$ no particle displacement is observed after shear cessation. Only at the sufficiently large strain amplitude of $\gamma_0 = 2.1$ is particle displacement observed after shear cessation. The inset of Figure 6.3 is the velocity profile of the fluid just before shear cessation. These particle displacements in Figure 6.3 corresponds to the velocity profiles of Figure 6.2(b) [4], which are consistent with the calculations shown in Figure 6.2(a).

The nearly perfect homogeneity of the velocity profiles just before shear cessation both from the calculations (inset of Figure 6.2(a)) and experiment (inset of Figure 6.3) clearly shows that the fluid had not gone through shear banding before shear cessation. However, the velocity profile is not perfectly homogeneous. It contains a very small degree of inhomogeneity due to the initial perturbation.

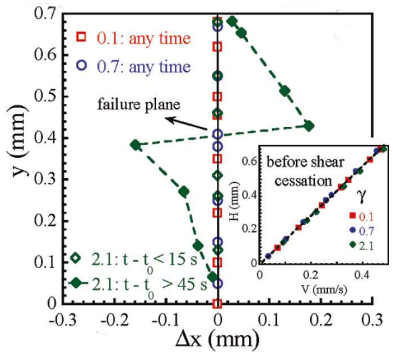

Figure 6.3: Experimental data for SBR250K showing positions of tracked particles after shear cessation for strain amplitudes $\gamma_0 = 0.1$ (red squares), $\gamma_0 = 0.7$ (blue circles) and $\gamma_0 = 2.1$ solid green squares. The 'failure plane' is indicated in the Figure, while the inset shows the velocity profile just before shear cessation for all strain amplitudes, Figures from [4].

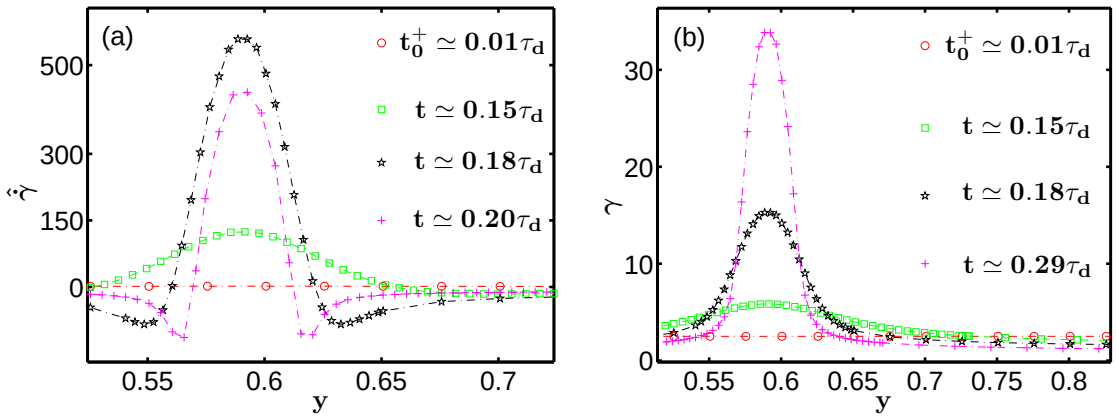

Figure 6.4: Spatially resolved (a) shear rate and (b) strain just after shear cessation t_0^+ and during 'fracture'. Calculations corresponding to Figure 6.2(a).

The noise amplitude of $\nu = 0.01$ is about 5% of the steady state stress plateau in Figure 6.1(b) or about 1% of the overshoot stress in Figure 6.1(a). The tracked particles used in the experiment of [4] are not small enough to resolve this scale of perturbations. Hence the velocity profile in the inset of Figure 6.3 appears homogeneous.

This apparent homogeneity of the velocity profile before shear cessation in the experiment of [4] was interpreted to mean that the chain network was still intact before shear cessation, after which it struggled for an 'induction time' before undergoing a cohesive failure [4]. However, the excellent qualitative agreement of the

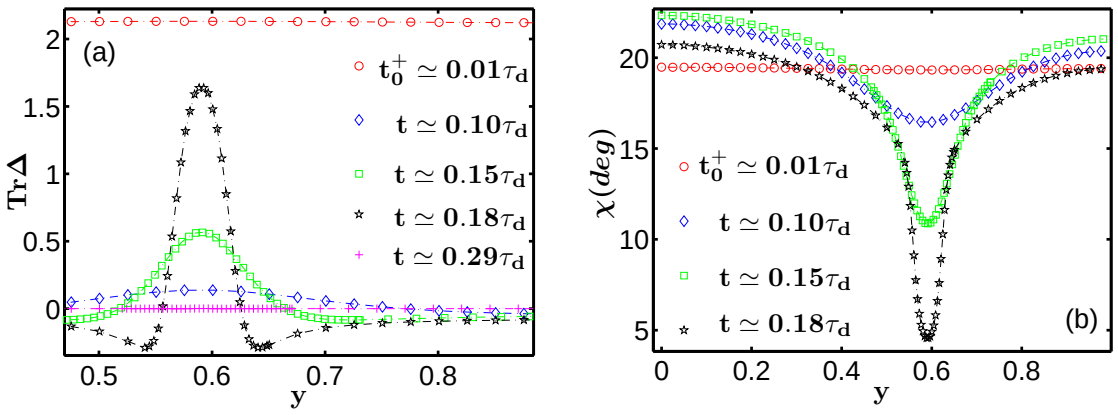

Figure 6.5: Calculated (a) Chain stretch and (b) Orientation angle of chains relative to the flow direction just after shear cessation at t_0^+ and during 'fracture'. Parameters as in Figure 6.2(a).

experimental data and the calculations in Figure 6.2 shows that this phenomenon does not involve such cohesive failure as suggested in [4]. This is because the theoretical model does not accommodate this process of cohesive failure of tube entanglements. This clearly demonstrates that new physics are not required to capture this phenomenon, at least qualitatively.

The calculations reveal that the velocity profile is not perfectly homogeneous. The slight inhomogeneity is revealed just after shear cessation at t_0^+ in Figure 6.2(a). This inhomogeneity then grows to initiate strain localisation in a narrow region in the fluid as seen in Figure 6.4(b). This 'phase separation' of strain implies a narrow region where the fluid continues to suffer an increasing shear between two outer layers where the fluid suffers very low shear as shown in Figure 6.4(a).

The shear rate is nearly zero just after shear cessation as in Figure 6.4(a). However, as time progresses, a narrow region of high shear rate corresponding to low viscosity develops between two regions of high viscosity as in Figure 6.4(a). As this low viscosity continues to develop in this narrow region, the two outer regions of high viscosity begin to slip against each other. The slip velocity is substantial enough to cause sufficient displacement of tracked particles within the scale of resolution of the apparatus of experiment [4]. This slip is so substantial that the

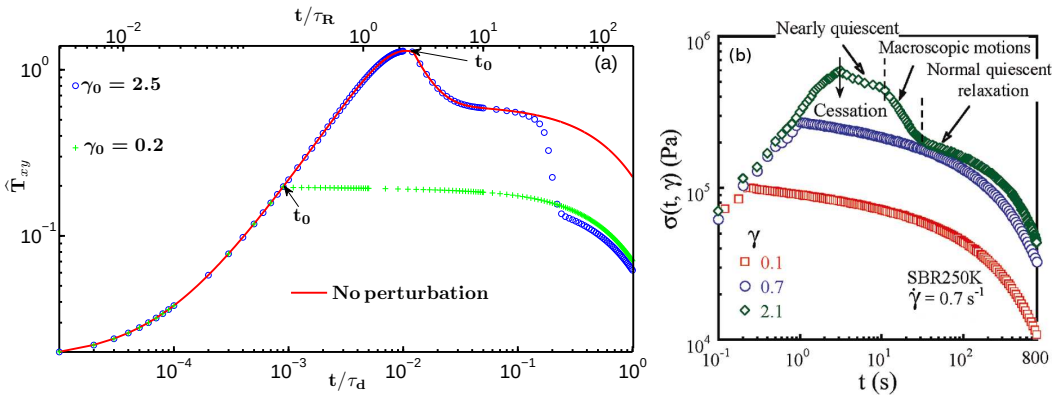

Figure 6.6: (a) Blue circles: shear stress from startup to shear cessation at t_0 showing an unusual fast relaxation during 'fracture'. Green crosses: similar to blue circles but with a smaller imposed strain. Red solid line: similar to blue circles but without an initial perturbation. Parameters as in Figure 6.2(a), $\tau_R = \tau_d/(3Z)$. (b) Experimentally measured shear stress from startup to shear cessation and beyond for applied shear rate $\dot{\gamma} = 0.7\text{s}^{-1}$ and different strain amplitudes γ showing features similar to the calculations, Figure from [4].

material appears like a solid undergoing fracture.

Figure 6.5(a) shows that the chain stretch is nearly homogeneous just after shear cessation at t_0^+. However, as the internal slip proceeds, the maximum shear rate $\widehat{\dot{\gamma}}_{max}$ in the slip layer grows such that $\widehat{\dot{\gamma}}_{max}\tau_R > 1$ as seen in Figure 6.4(a). This then induces a sizable stretch in the chain segments in the slip layer as seen in Figure 6.5(a). The stretch grows during 'fracture' and finally relaxes to zero. Figure 6.5(b) shows that the alignment of chain segments relative to the flow direction decreases during 'fracture'. The chain alignment angle χ is calculated from [60]

$$\tan 2\chi = \frac{2\Delta_{xy}}{\Delta_{xx} - \Delta_{yy}}. \tag{6.2}$$

The increase in stretch and decrease in alignment angle of chain segments in the slip layer indicate a strong alignment of stretched chain segments in the flow direction as opposed to the suggestion of a cohesive failure in [4].

With the initial perturbation in Figure 6.1(c) and a strain amplitude $\gamma_0 = 2.5$, the shear stress increases from startup and goes through an overshoot just before

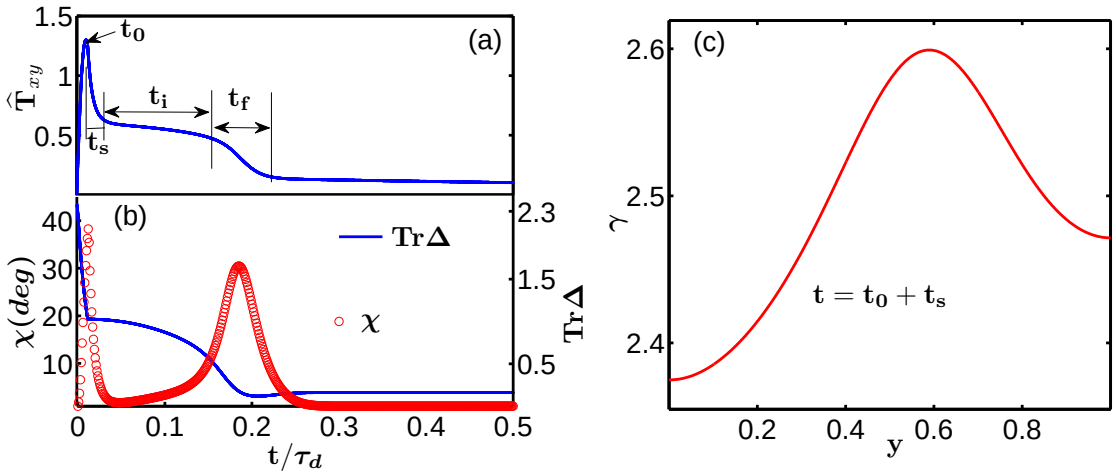

Figure 6.7: (a) Shear stress from startup to shear cessation at t_0 with the stretch relaxation time t_s, 'induction time' t_i and 'fracture time' t_f indicated. (b) Maximum chain stretch (red circles) and minimum chain orientation angle (blue solid line) in space corresponding to the stress profile in (a). (c) Spatial profile of strain at the time $t = t_0 + t_s$ just after stretch relaxation. Parameters as in Figure 6.2(a).

shear cessation for the applied shear rate of $\langle\dot{\hat{\gamma}}\rangle = 200$ as shown by the blue circles in Figure 6.6(a). However, just after shear cessation, the shear stress shows an initial quick relaxation. Figures 6.7(ab) show that this initial quick relaxation, which lasts a duration indicated as t_s in Figure 6.7(a), is due to relaxation of stretch, but the chain alignment angle stays nearly constant during this period. The shear stress then enters a plateau for a duration indicated as $t_i \approx 30\tau_R$ in Figure 6.7(a). During this period, the chain stretch only increases slowly while the chain alignment decreases very slowly as seen in Figure 6.7(b). The shear stress then relaxes very rapidly for a duration indicated as t_f in Figure 6.7(b). During t_f the stretch increases very rapidly and finally relaxes to its equilibrium value and the chain alignment decreases very rapidly and increases slightly to its equilibrium value as in Figure 6.7(b). After t_f, the shear stress resumes its quiescent relaxation as shown by the blue circles in Figure 6.6(a). The final slow relaxation almost coincides with the quiescent relaxation for a material subjected to the same step shear of $\langle\dot{\hat{\gamma}}\rangle = 200$ but with a strain amplitude of $\gamma_0 = 0.2$ as shown by the green crosses in Figure 6.6(a).

The red solid line in Figure 6.6(a) shows that with no initial perturbation the shear stress only goes through a quiescent relaxation after the same strain amplitude of $\gamma_0 = 2.5$. For the small strain amplitude of $\gamma_0 = 0.2$, only a quiescent relaxation is seen, even with the initial perturbation.

The green squares of Figure 6.6(b) show the behaviour of the experimentally measured shear stress for the material SBR250K subjected to a shear rate of $\dot{\gamma} = 0.7\text{s}^{-1}$ at a strain amplitude $\gamma_0 = 2.1$. After shear cessation the shear stress falls into a plateau indicated as 'nearly quiescent' in Figure 6.6b. This plateau is consistent with the plateau shown by the blue circles in Figure 6.6(a) which is indicated by the time t_i in Figure 6.7(b). The stress then shows a quick relaxation indicated as 'macroscopic motions' in Figure 6.6(b), which is consistent with the calculations as shown by the blue circles in Figure 6.6(a) or t_f in Figure 6.7(a). Finally the shear stress resumes its slow relaxation indicated by 'normal quiescent relaxation' in Figure 6.6(b). This final slow relaxation nearly coincides with the slow relaxation of the material subjected to a strain amplitude of $\gamma_0 = 0.7$ as shown by the blue circles in Figure 6.6(b). The experimental data of Figure 6.6(b) show that for the insufficient strain amplitudes of $\gamma_0 = 0.1$ and $\gamma_0 = 0.7$, only quiescent relaxation is observed, and this is consistent with the green crosses in Figure 6.6(a) where the low strain amplitude of $\gamma_0 = 0.2$ only leads to a quiescent relaxation. This excellent agreement of the calculated shear stress and the experimentally measured shear stress under different strain amplitudes again demonstrates that new physics are not necessary to demonstrate these phenomena.

The fast stress relaxation during the internal slip or 'fracture' is due to dissipation of elastic energy in the form of stress relaxation. When the fluid is subjected to sufficiently large strain, and in the presence of nonuniform stresses, the material will dissipate the accumulated strain or elastic energy nonuniformly. The initial perturbation induces nonuniform stresses in the material which then induces strain localisation in the material.

In the experiments, these perturbations can be induced, say, from non-uniform relaxation of the material after sample loading, or by temperature gradients in the material. There is no statement of reproducibility in the report [4] except that the position of the 'failure plane' varies in different runs of the experiment. This make it difficult to pin down what exactly may have been the cause of the fluctuations in the experiment. The effect of the initial perturbation in inducing a nonuniform strain in the material is clearly seen in the strain profile after stretch relaxation as seen in Figure 6.7(c). The position of the maximum at $y \approx 0.6$ coincides with the region where the slip layer occurs in Figure 6.4(a). In the case where there is no initial perturbation, this nonuniform strain does not show up. Then the fluid just dissipates the accumulated strain uniformly and the unusual fast stress relaxation does not occur as shown by the red solid line in Figure 6.6(a).

The fact that $\partial T_{xy}/\partial\gamma < 0$ at t_0 in Case I suggests a possible elastic instability in the material. This is coupled with the fact that the applied shear rate satisfies $\partial T_{xy}/\partial\widehat{\dot{\gamma}} < 0$ which is a sign of viscous instability. The instability creates the environment for the initial perturbation to grow and induce strain localisation which gives this 'fracture' effect. If there is a viscous contribution to the instability, then 'fracture' should occur if shearing is stopped before the condition $\partial T_{xy}/\partial\gamma < 0$ is reached. This possibility is explored in Cases II and III.

6.2 Case II: High Shear Rate, Low Strain

For the case where the applied shear rate $\langle\widehat{\dot{\gamma}}\rangle = 900$ gives $\langle\widehat{\dot{\gamma}}\rangle\tau_R \simeq 4.17 > 1$ and the applied strain $\gamma_0 = 2.5 < \gamma_{ov} \approx 4.2$, then $\partial T_{xy}/\partial\gamma > 0$ at t_0. The total shear stress at t_0 for this Case is indicated by II in Figure 6.1(b). The total shear stress shows the unusual fast relaxation after an initial delay similar to Case I. This behaviour is seen in Figure 6.8(a).

The applied shear rate which gives $\langle\widehat{\dot{\gamma}}\rangle\tau_R > 1$ is well into the stretching regime.

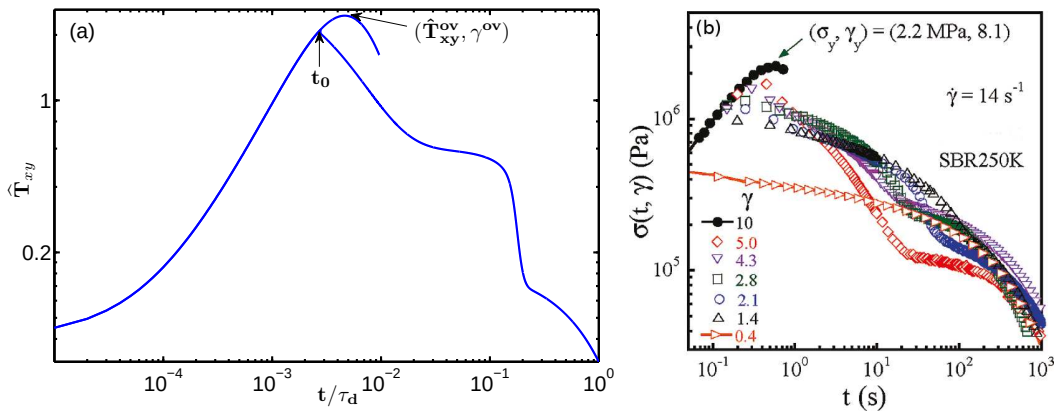

Figure 6.8: (a) Shear stress evolution during 'fracture' for Case II. Parameters as in Figure 6.2(a), $\langle\hat{\dot{\gamma}}\rangle = 900$. (b) Experimentally measured shear stress corresponding to case II, Figure from [4].

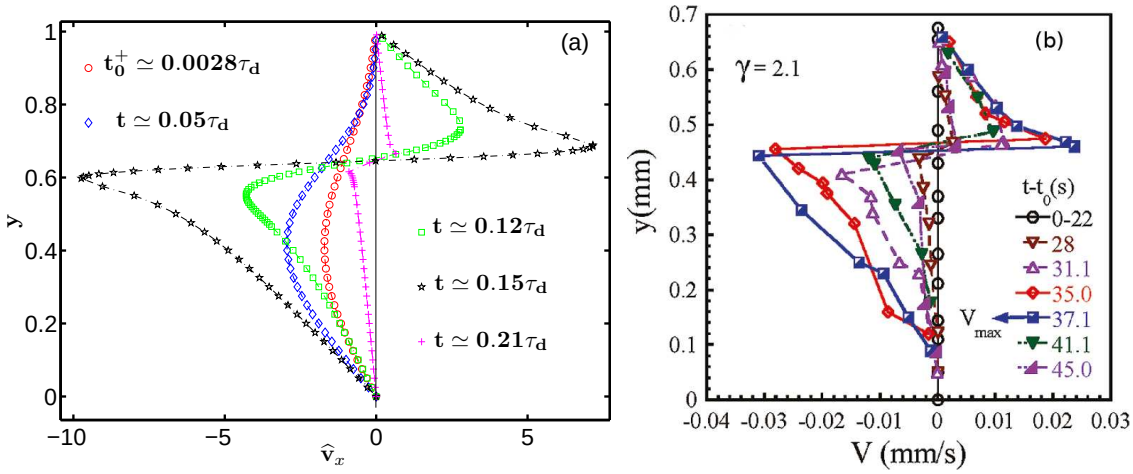

Figure 6.9: (a) Velocity profile during 'fracture' for Case II. Parameters as in Figure 6.2(a), $\langle\hat{\dot{\gamma}}\rangle = 900$. (b) Corresponding experimentally measured velocity profile for SBR250K consistent with Case II, Figure from [4].

But $\partial T_{xy}/\partial\gamma > 0$ at t_0. This implies that, although the elastic instability is yet to show up in this regime, there is still sufficient elasticity in the system since the chains are highly stretched. However, there is obviously a viscous contribution to the instability. This is because 'fracture' is still possible even when $\partial T_{xy}/\partial\gamma > 0$ at t_0.

In this case, the delay time or 'induction time' of the shear stress in the plateau after stretch relaxation is comparable to the Case I. The experimentally measured shear stresses shown in Figure 6.8(b) show a similar delay before going through a

fast relaxation for strain amplitudes ≥ 2.1. In both the calculations and experiment, shearing is stopped before the stress overshoot. The overshoot stress and strain for the calculation is indicated by $(\hat{T}_{xy}^{ov}, \gamma^{ov})$ in Figure 6.8(a). Similarly, the overshoot stress and strain in the experimentally measured shear stress is indicated as (σ_y, γ_y) in Figure 6.8(b).

Also, the fluid velocity shows a corresponding fracture-like profile during this fast stress relaxation as in Figure 6.9(a). The 'fracture' profile is very similar to the experimentally measured velocity profile shown in Figure 6.9(b). The experimentally measured velocity profile shown in Figure 6.9(b) corresponds to the experimentally measured shear stress for the applied strain $\gamma_0 = 2.1$ as shown in Figure 6.8(b).

6.3 Case III: Low Shear Rate, Low Strain:

Case III explores the situation where the elasticity due to stretch is significantly reduced as the applied shear rate of $\langle\widehat{\dot{\gamma}}\rangle = 10$ satisfies $\langle\widehat{\dot{\gamma}}\rangle\tau_R \simeq 0.05 < 1$. In this case, there is no significant chain stretch. Instead, most of the stress comes from chain alignment in the flow direction. Also, the applied strain satisfies $\gamma_0 = 1.3 < \gamma_{ov} \approx 1.4$. That is, shearing is stopped before the stress overshoot, so that $\partial T_{xy}/\partial\gamma > 0$ at t_0. The total shear stress at t_0 for this Case in indicated by III in Figure 6.1(b). Hence Case III is dominated by viscous behaviour. It is difficult to identify any delayed or fast stress relaxation in this Case. The stress seems to relax quiescently as seen in Figure 6.10(a).

Similarly, the experimentally measured shear stress for this case shows very little delay, as in Figure 6.10(b). Comparing Figure 6.10(b) with Figures 6.8(b) and 6.6(b) shows that the delay time for Case III is much less than for the Cases II and I. However, the calculated velocity profile for this case is more consistent with the experimentally measured profiles. The calculated profiles in Figure 6.11(a)

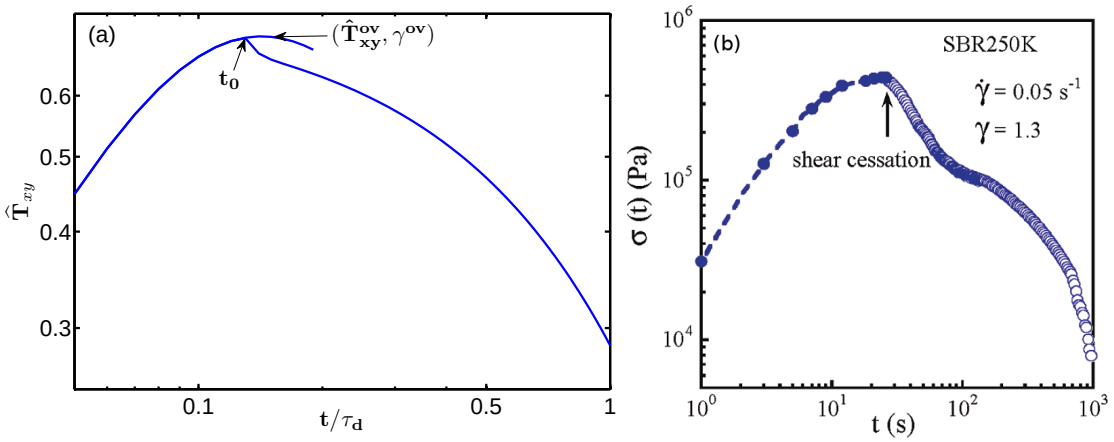

Figure 6.10: (a) Shear stress evolution for Case III. Parameters as in Figure 6.2(a), $\langle\hat{\dot{\gamma}}\rangle = 10$. (b) Experimentally measured shear stress corresponding to Case III, Figure from [4].

are roughly two orders of magnitude less than the calculated velocity profiles for Cases II and I. Similarly, the experimentally measured velocity profiles shown in Figure 6.11(b) are roughly one order of magnitude less than the experimentally measured velocity profiles for Cases I and II.

Case III demonstrates the role of viscous effects to the instability leading to 'fracture'. However, viscous effects alone are not sufficient to bring about significant 'fracture' as the 'fracture' seen here is very 'weak' compared to Cases I and II.

6.4 Characterisation of Fracture

The case III described in the previous section shows that it may be possible to obtain the 'fracture' effect with some parameter values, but the 'fracture' may not be significant. This 'weak fracture' may not be measurable experimentally. Therefore to determine parameter values which yield possible experimentally measurable 'fracture', then it is necessary to introduce a criterion for 'fracture'. To this end,

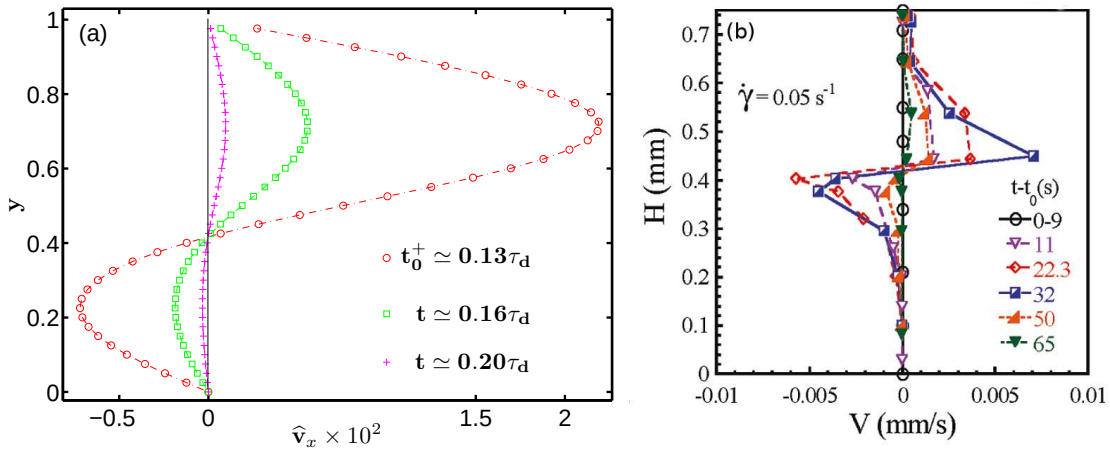

Figure 6.11: (a) Velocity profile for Case III. Parameters as in Figure 6.2(a), $\langle\hat{\dot{\gamma}}\rangle = 10$. (b) Experimentally measured velocity profiles corresponding to Case III, Figure from [4].

let μ_+ and μ_- be velocity moments defined as

$$\mu_+ = \frac{\sum_i v_i H(v_i)}{\sum_i H(v_i)} \tag{6.3a}$$

$$\mu_- = \frac{\sum_i v_i H(-v_i)}{\sum_i H(-v_i)}, \tag{6.3b}$$

where the sum is over all spatial positions y_i and H is the Heaviside step function. If both positive moment μ_+ and negative moment μ_- occur together at any time during stress relaxation after shear cessation, then 'fracture' has occurred; otherwise there is no 'fracture'. When there is no 'fracture' μ_+ becomes non zero after shear cessation, but later relaxes to zero while μ_- stays at zero throughout the duration of stress relaxation from shear cessation. Otherwise, μ_- becomes non zero after shear cessation, and later relaxes to zero while μ_+ stays at zero for the duration of stress relaxation after shear cessation.

For parameter values where

$$\left|\frac{\mu_-}{\mu_+}\right| > 0.7, \tag{6.4}$$

at any time after shear cessation, the velocity profiles give a clear 'failure' plane as in Figure 6.2(a), and the shear stress shows discernible slow and fast relaxation intervals after stretch relaxation. The criterion in Equation (6.4) is somewhat arbitrary since it is not derived from the model, but based on inspection of the data. However, it consistently captures the key signatures of the 'fracture' phenomenon. Using this criterion in Equation (6.4), the parameter values of β, Z and γ_0 where 'fracture' occurs for a given $\langle\widehat{\dot{\gamma}}\rangle$ can be explored. The results are shown in Figure 6.12.

6.4.1 CCR, Strain and Number of Entanglements per Chain

There is a low range of CCR within which 'fracture' occurs as shown in Figure 6.12(a) for different number of entanglements per chain Z and applied strains γ_0. The effect of β on 'fracture' can be easily understood since large values of β removes the nonmonotonic behaviour in the constitutive curve. As β is increased, the stability of the fluid to small amplitude perturbation increases, so that the scale of amplitude of the perturbation needs to be increased to yield 'fracture'. All the values of β shown in Figure 6.12(a) which yield 'fracture' also yield nonmonotonic constitutive curves.

For any given applied shear rate, there is a lower cut-off for Z below which 'fracture' does not occur for any applied strain γ_0 as in Figure 6.12(b). Also, there are left and right boundaries for Z for different values of γ_0 as seen in Figure 6.12(b). The behaviour of 'fracture' with γ_0 and Z is due to the nature of the free energy function describing the fluid. This free energy function exhibits a negative curvature at certain range of γ_0, where the fluid becomes unstable to small amplitude fluctuations. The growing perturbation after shear cessation competes with the background reptation and this competition is mediated by Z. When Z is not large enough, then the perturbation decays to zero, and no 'fracture' occurs. Other-

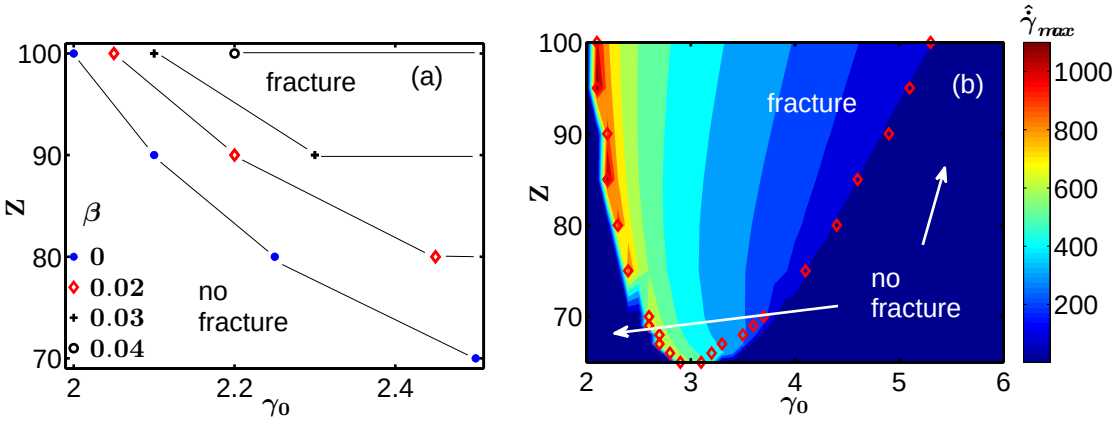

Figure 6.12: Range of parameters for $\langle\dot{\hat{\gamma}}\rangle = 200$ (a)β, Z and γ_0, (b) Z and γ_0 for $\beta = 0$ for which 'fracture' is or not observed. The contours are the peak values of the shear rate in the slip layer during 'fracture' which are represented by the legend.

wise when Z is large enough, the growing pertubation wins the competition and 'fracture' occurs. This leads to the minimum in Z seen in Figure 6.12(b). More details of the effect of γ_0 and Z in determining the behaviour of the free energy will be given in Chapter 7. Figure 6.12(b) shows that the transition to 'fracture' from the left boundary is much sharper than the transition to 'no fracture' at the right boundary. This is because the fluid has been sheared for much longer for the larger strain amplitudes at the right boundary. This allows more reptation to occur which dissipates some of the elastic energy away as the shear stress moves closer to the steady state. The severity of 'fracture' can be quantified by the peak value of the shear rate $\dot{\hat{\gamma}}_{max}$ in the slip layer during fracture. Figure 6.12(b) shows that lower values of γ_0 yield more severe 'fracture'. At $\langle\dot{\hat{\gamma}}\rangle = 200$, the higher strains have gone further beyond the overshoot bringing the shear stress to a lower value before shear cessation, so that less stress is released during 'fracture', hence the 'fracture' is less severe at higher values of γ_0 [57].

6.4.2 Fracture Width

The overshoot strain $\gamma_{ov} \simeq 2.1$ for the applied shear rate $\langle\widehat{\dot{\gamma}}\rangle = 200$. Then the strains shown in Figure 6.13(b) already take the shear stress beyond the overshoot. The higher strains take the shear stress further beyond the overshoot, so that less elastic energy is dissipated during 'fracture', thus leading to less severe 'fracture'. This situation leads to a reduction in the peak of shear rate $\widehat{\dot{\gamma}}_{max}$ as seen in Figure 6.13(c). The width of the slip layer during 'fracture' can be quantified by the full width at half maximum ($FWHM$) of the shear rate at the peak of 'fracture'. This is illustrated in Figure 6.13(a), where $FWHM = y_2 - y_1$. The width of the slip layer increases as 'fracture' becomes less severe at higher applied strains as shown in Figure 6.13(b).

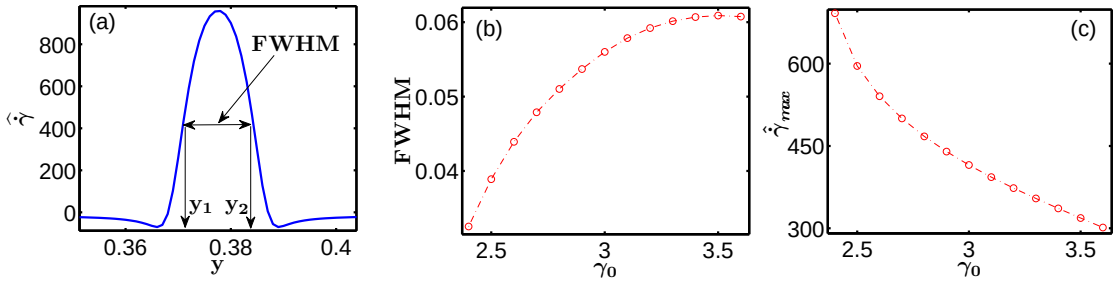

Figure 6.13: (a) Illustration of the 'fracture width' defined as the Full Width at Half Maximum of the shear rate profile at the peak of 'fracture'. (b) 'Fracture width' and (c) maximum shear rate at different strains amplitudes. Parameters: $\langle\widehat{\dot{\gamma}}\rangle = 200$, $Z = 72$.

6.4.3 Type C Behaviour

Figure 6.14(a) shows that the unusual fast stress relaxation associated with 'fracture' is the Type C behaviour earlier reported in the literature, for example [15]. This is revealed by the nonlinear relaxation modulus $G(t, \gamma_0)$ defined as

$$G(t, \gamma_0) = \frac{T_{xy}(t, \gamma_0)}{\gamma_0}. \tag{6.5}$$

Figure 6.14(a) shows that $G(t, \gamma_0)$ suddenly develops a 'kink' at intermediate times

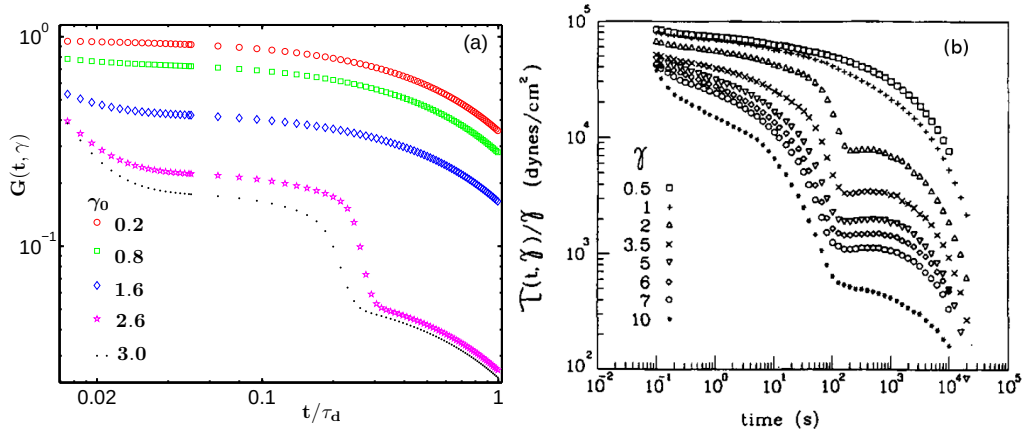

Figure 6.14: (a) Calculated nonlinear relaxation moduli at different applied strains. (b) Corresponding experimentally measured nonlinear relaxation moduli for polystyrene solutions at different strain amplitudes γ indicated in the Figure. Figure from [19]. Both Figures show a 'kink' in the nonlinear relaxation moduli at intermediate times for large enough strain amplitude.

as the applied strain γ_0 is increased, this is a key characteristic of this behaviour. Figure 6.14(a) is consistent with the experimentally measured nonlinear relaxation moduli shown in Figure 6.14(b) which shows a material exhibiting Type C behaviour at sufficiently large values of Z and γ_0. This Type C behaviour which is an excessive strain softening at intermediate strains has its origin in the behaviour of the free energy describing polymeric liquids at intermediate strains. Details of this discussion will be given in the next Chapter.

6.4.4 Induction Time

The delay time t_i (or 'induction time') after stretch relaxation decreases as the number of entanglements Z increases as shown in Figure 6.15(a). Figure 6.15(b) shows stress relaxation after step shear for strain amplitude $\gamma = 2.1$ applied to three different SBR melts. The melts have molecular weights 174000 gmol^{-1} (SBR170K), 250000 gmol^{-1} (SBR250K) and 497000 gmol^{-1} (SBR500K) [4], and the applied shear rate to each sample is such that $\dot{\gamma}\tau_R = 3.0$. Also, the number of entangle-

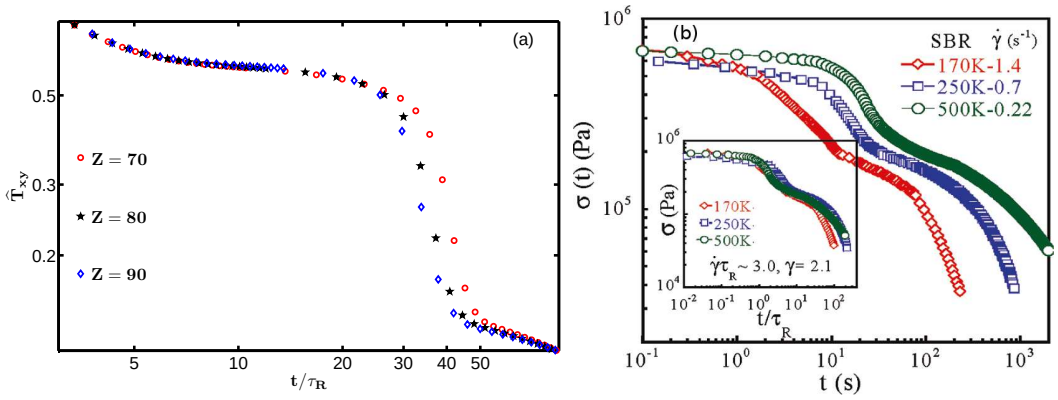

Figure 6.15: (a) Variation of 'induction time' with Z at fixed $\gamma_0 = 2.5$, $\langle\hat{\dot{\gamma}}\rangle\tau_R = 3.0$ and $\beta = 0$ from the calculations. (b) Experimentally measured shear stresses for step shears of the materials indicated in the Figure showing a variation of 'induction time' with molecular weight. Figure from [4].

ments per chain Z for the melts were reported [4] as $Z = 53$ (SBR170K), $Z = 76$ (SBR250K) and $Z = 160$ (SBR500K). Figure 6.15(b) shows that the material with higher molecular weight exhibits the longest delay before 'fracture', while the material with the lowest molecular weight exhibits the shortest delay. This suggests an increase in 'induction time' with increasing number of chain entanglement.

However, the inset of Figure 6.15(b) shows that SBR500K which has the highest molecular weight and Z value has the shortest 'induction time'. This is followed by SBR250K which has an intermediate Z. It is not so clear from the inset of Figure 6.15(b) where the 'induction time' of SBR170K lies. The data in the inset of Figure 6.15(b) have been scaled by τ_R, and this gives a better agreement with the calculations. In order to do calculations consistent with Figure 6.15(b), different shear rates $\langle\hat{\dot{\gamma}}\rangle$ were applied for each value of Z to maintain $\langle\hat{\dot{\gamma}}\rangle\tau_R = 3$. This data is shown in Table 6.1, where $\gamma_0 = 2.5$ in all cases. Figure 6.15(a) shows that the material with the highest value of Z has the shortest 'induction time' in agreement with the inset of Figure 6.15(b). The time axis of Figure 6.15(a) has been scaled by τ_R to make it comparable to the inset of Figure 6.15(b).

The quantities in the model Equations 4.17 have been scaled by τ_d which effectively sets $\tau_d = 1$. Hence the procedure of changing Z in the calculations cor-

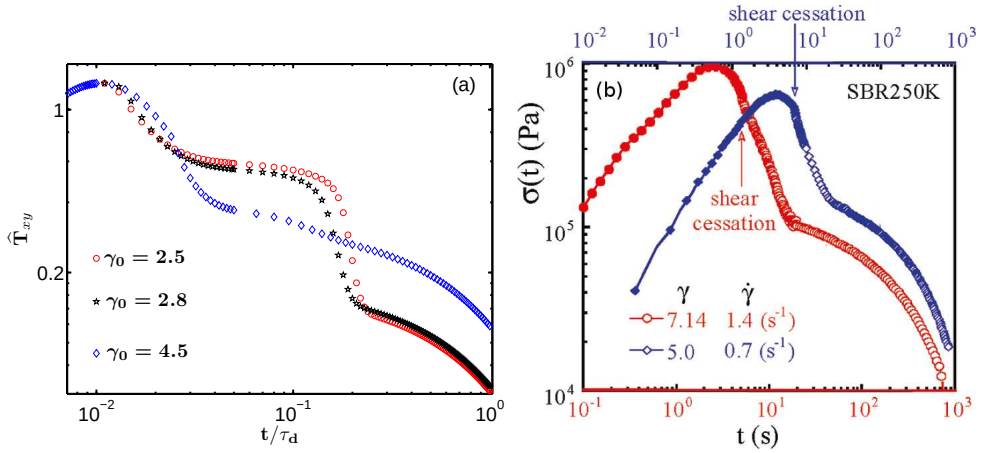

Figure 6.16: (a) Variation of 'induction time' with applied strains at fixed $Z = 72$, $\langle\dot{\hat{\gamma}}\rangle = 200$ and $\beta = 0$ from the calculations. The applied strain $\gamma_0 = 4.5$ gives negligible 'induction time'. (b) Experimentally measured shear stresses for step shears at the applied strains indicated. The material SBR250K exhibits negligible 'induction time' at these high strains. Figure from [4].

Table 6.1: Applied shear rates for fixed $\langle\dot{\hat{\gamma}}\rangle\tau_R$ at different values of Z

$\langle\dot{\hat{\gamma}}\rangle$	Z	$\langle\dot{\hat{\gamma}}\rangle\tau_R$
630	70	3
720	80	3
810	90	3

responds to using materials with the same values of τ_d but different values of τ_R. This procedure does not directly match the experimental situation of using samples of different molecular weights since samples with different molecular weights have different values of τ_d and τ_R. However, materials with higher molecular weights have a larger separation between τ_R and τ_d. This situation is the same with the calculations. This separation of timescales between τ_R and τ_d is more important than the individual values of τ_R and τ_d. Hence the level of agreement found between Figure 6.15(a) and the inset of Figure 6.15(b).

The decrease in 'induction time' with increasing Z seen in Figure 6.15(a) is due to a 'weakening' of the strength of reptation in its competition with the growing perturbation at higher values of Z. This idea is suggested by the MG theory

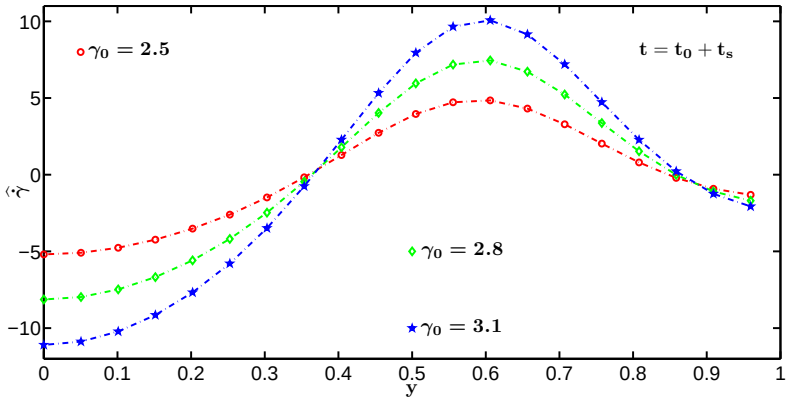

Figure 6.17: Calculated shear rate just after stretch relaxation (the time $t_0 + t_s$ in Figure 6.7(a)) at the applied strains indicated in the Figure. Parameters: same as in Figure 6.2 but with different strains.

which will be described in Chapter 7. Also, the perturbations grow faster as Z increases, and hence 'fracture' develops more quickly with increasing Z as seen in Figure 6.15(a). More details of the perturbations will be given in Chapter 7.

The variation of 'induction time' with applied strain is easier to compare with experimental data as this does not involve variation of relaxation times. Figure 6.16(a) shows that when the applied strain takes the shear stress further beyond the overshoot, the induction time decreases, which is in excellent agreement with the experimental data. Figure 6.16(b) shows the experimentally measured shear stress for the material SBR250K for strain amplitudes $\gamma_0 = 5.0$ and $\gamma_0 = 7.14$. The material shows significantly reduced induction times unlike in the case of Figure 6.6(b) where the material shows a much more significant 'induction time' for a smaller strain amplitude $\gamma_0 = 2.1$. In particular, the shear rate $\dot{\gamma} = 0.7\text{s}^{-1}$ in Figure 6.16(b) matches the shear rate in Figure 6.6(b). But in Figure 6.16(b), the strain amplitude of $\gamma_0 = 5.0$ shows an insignificant 'induction time' compared with Figure 6.6(b) of a lower strain amplitude. This behaviour agrees very well with the calculations in Figure 6.16(a) where the strain amplitude $\gamma_0 = 4.5$ shows an insignificant 'induction time' compared with the smaller strain amplitudes $\gamma_0 = 2.8$ and $\gamma_0 = 2.5$.

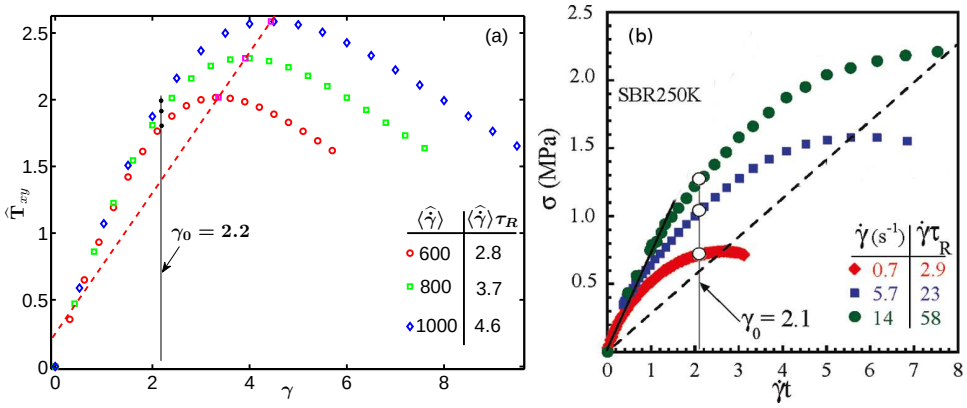

Figure 6.18: (a) Shear stress versus strain at the three different applied shear rates (calculated) indicated in the figure such that $\langle\hat{\dot{\gamma}}\rangle\tau_R > 1$ in all cases. The dashed line connects the strains for overshoot and their corresponding stresses for each applied shear rate. The strain $\gamma_0 = 2.2$ indicated in the Figure lies in the sub overshoot regime in the three cases. The applied shear rates $\langle\hat{\dot{\gamma}}\rangle$ and corresponding values of $\langle\hat{\dot{\gamma}}\rangle\tau_R$ are summarised in the table in the inset. (b) Experimental data corresponding to (a) for the material SBR250K. Figure from [4].

Since shearing is stopped at a later time for a higher applied strain, then the initial perturbation has more time to grow before shear cessation for a higher applied strain. Since the initial perturbation has grown to a higher amplitude for a higher applied strain, it induces 'strain localisation' faster for a higher applied strain. This leads to a reduction in the 'induction time' for a higher applied strain as seen in Figure 6.16(a). The amplitude of the growing perturbation is proportional to the peak of the inhomogeneous shear rate after shear cessation. Figure 6.17 shows the shear rate profiles after stretch relaxation for three different strain amplitudes indicated in the Figure. The perturbation had grown the most for $\gamma_0 = 3.1$ at the end of stretch relaxation than for $\gamma_0 = 2.8$ and $\gamma_0 = 2.5$. However, as the applied strain is increased further, the 'fracture' effect gradually reduces leading to the insignificant 'induction time' seen in Figure 6.16(a). This is due to the increased dissipation by reptation at higher strain amplitude which reduces the elasticity in the material. More details of this effect of reptation will be given in the next Chapter.

Figure 6.18(a) shows the shear stress as a function of strain for three differ-

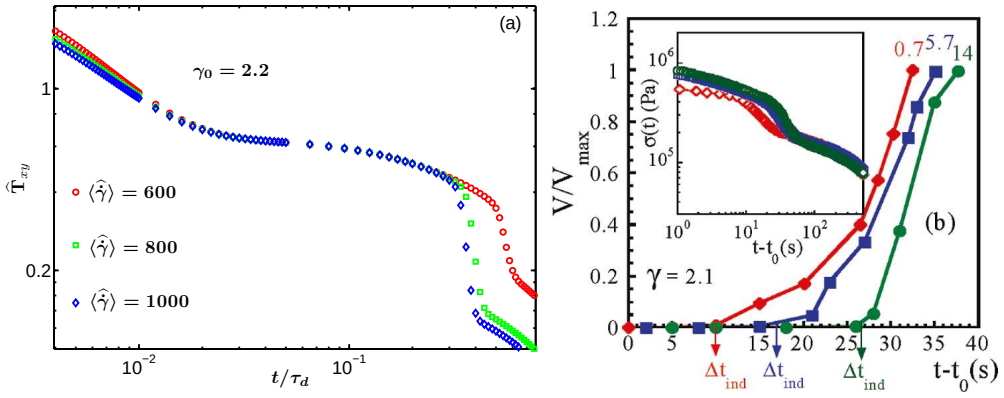

Figure 6.19: (a) Variation of 'induction time' for the applied shear rates in Figure 6.18(a). The applied strain $\gamma_0 = 2.2$ is indicated in Figure 6.18(a). (b) Experimentally measured 'induction times' Δt_{ind} for the material SBR250K at the applied shear rates indicated in Figure 6.18(b). The applied strain $\gamma_0 = 2.1$ is indicated in Figure 6.18(b). Figure from [4].

ent applied shear rates such that $\langle\dot{\hat{\gamma}}\rangle\tau_R > 1$ as indicated in the Figure. The overshoot stresses follow a straight line and they increase with increasing shear rates and strain. This is in excellent agreement with the experimentally measured shear stresses at shown in Figure 6.18(b). The applied shear rates in the experimental data of Figure 6.18(b) also meet the same criteria of $\dot{\gamma}\tau_R > 1$ as seen in Figure 6.18(b). For the sub overshoot strain of $\gamma_0 = 2.2$ in Figure 6.18(a), Figure 6.19(a) shows that the higher applied shear rate yields the shortest 'induction time'. This is at variance with the experimental data which shows that for the sub overshoot strain of $\gamma_0 = 2.1$ in Figure 6.18(b), the higher imposed shear rate yields the longest 'induction time' as seen in Figure 6.19(b) and the inset of Figure 6.19(b). The reason for this discrepancy is not understood at the moment. However, the calculations to be presented in the next Chapter show that the growth rate of the perturbation is higher at a higher applied shear rate, so that 'fracture' develops faster at a higher applied shear rate.

6.5 Curvature Effects

The calculations describing the 'fracture' phenomenon presented in the foregoing discussion have been carried out in the Cartesian coordinates system following the experiments of [4]. However, this phenomenon can still be realized in curved geometries, for example in the cylindrical Couette geometry or cone and plate configuration. For the cylindrical Couette case, the calculations are repeated with finite inertia ($\widehat{\rho} = 10^{-10}$) for the initial condition shown in Figure 6.20(a). The initial condition is applied applied to $\Delta_{\theta\theta}$ in Equation (4.50). The same initial condition shown in Figure 6.20(a) is applied to Δ_{xx} in Equation 4.17 so that the results can be compared to the case of flat plates. The curvature parameter $q = 0$ for flat plates, and the value $q = 2 \times 10^{-4}$ for the cylindrical Couette case is consistent with typical cone angles for cone and plate configurations [25].

Figure 6.20(b) shows the velocity profiles for both cases at the peak of 'fracture' where $\langle\widehat{\dot{\gamma}}\rangle = 200$, $\gamma_0 = 2.5$ and $Z = 72$. The velocity profiles in Figure 6.20(b) almost match except for a slight difference in the positions of the 'failure planes'. Similarly, the shear stresses for both cases almost match except for a slight delay in the onset of 'fracture' for the cylindrical case as seen in Figure 6.20(c).

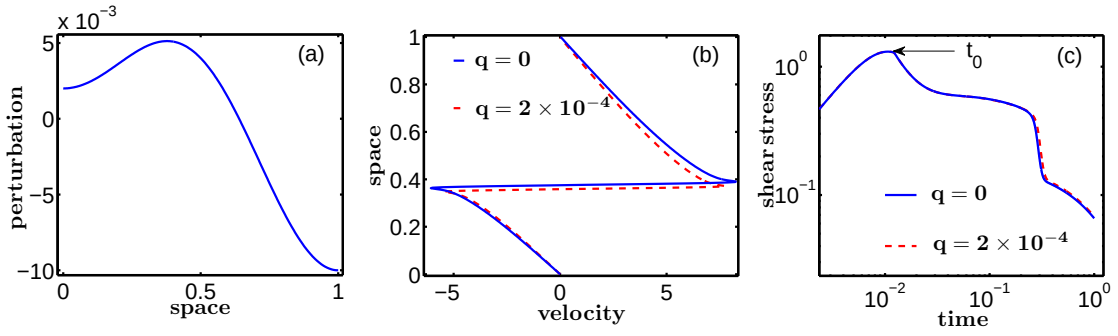

Figure 6.20: (a) Initial condition imposed on Δ_{xx} (flat plates) or $\Delta_{\theta\theta}$ (cylindrical Couette). (b) Velocity profile at the time $t \simeq 0.281\tau_d$ (flat plates) or $t \simeq 0.296\tau_d$ (cylindrical Couette) when the shear rate is maximum during 'fracture'. (c) Shear stress from startup and subsequent relaxation after shear cessation at t_0 for both cases. Parameters: $q = 0$ (flat plates), $q = 2 \times 10^{-4}$ (cylindrical Couette), $\langle\widehat{\dot{\gamma}}\rangle = 200$, $\gamma_0 = 2.5$, $Z = 72$, $\epsilon = 10^{-4}$ and $\widehat{\mathcal{D}} = 10^{-5}$.

Figure 6.20 shows that the 'fracture' phenomenon is not restricted to flat plate configurations. It can also be realized with the cone and plate configuration. However, it may not be practical to do this kind of experiment in the cylindrical Couette geometry as high molecular weight samples are required to see 'fracture'. It will be very difficult to load samples of the required molecular weight between concentric cylinders that are extremely close.

6.6 Remarks

It is quite surprising that this strange fracture-like behaviour can be captured very well with the simple Diffusive Rolie-Poly (DRP) viscoelastic model without adding new physics. There have been suggestions before [3, 4] that new physics will be required to explain this phenomenon. This involves an interplay between a retraction force in the polymer strands developed during deformation and a cohesive force that maintains chain entanglement. A cohesive 'failure' or 'fracture' occurs when the retraction force exceeds the cohesive force during strong flows [3, 4]. The results presented so far show that the physics of chain stretch and alignment as well as reptation already contained in the DRP model is sufficient to capture most of the essential aspects of this 'fracture' phenomenon. This is not to say that the current viscoelastic models are complete. There have been discrepancies reported between calculations from molecular dynamics simulations and predictions of tube models [41]. Figure 6.19 also shows a discrepancy between experimental data of [4] and calculation from the DRP whose origin is not clear at this time. These discrepancies suggest that new physics may still be required to make the current tube models complete.

Apart from this little discrepancy, the calculations show excellent qualitative and near quantitative agreement with the experimental data. Although the 'fracture' phenomenon seems to be new because it has only been reported recently [4],

Figure 6.14 shows that it is actually not new. It is the same phenomenon which has been tagged 'Type C behaviour' in the past [15, 16, 19]. If the earlier workers carried out some visualisation during this Type C measurement they would have observed 'fracture' long before now.

The dependence of 'fracture' on spatial inhomogeneities suggest that the 'fracture' is just an event that occurs due to imperfections in the experiments and also thermal fluctuations in the samples. Non uniform distribution of the material during sample loading, small temperature gradients or slight misalignments of plates are possible causes of these inhomogeneities. It will be interesting to see an experiment where these inhomogeneities are carefully controlled and the possible dependence of this event on the shape of these inhomogeneities probed.

The high shear rate and small chain alignment angle in the slip layer during 'fracture' suggests that the chains become highly aligned in the flow direction within the slip layer during this 'fracture' event. It will be interesting to do a molecular dynamics simulation of this event where the state of chain alignment or entanglement during 'fracture' can be probed directly.

This discussion now proceeds with a more detailed study of the perturbations used in initiating this fracture-like behaviour.

Chapter 7

Analysis of Perturbations

The procedure for modelling the 'fracture' phenomenon has been presented in Chapter 6 and the role of small amplitude perturbations has been illustrated. A more detailed study of these perturbations is now presented in this Chapter. This will involve checking for possible signs of instability in the system. Although the nonmonotonic constitutive relation in Figure 6.1(b) already indicates instability in the system when the applied shear rate satisfies $\langle\hat{\dot{\gamma}}\rangle > 1$, the analysis to be carried out in this chapter will reveal possible elastic or viscous contributions to this instability.

The initial perturbations used to initiate the fracture-like behaviour discussed in Chapter 6 were applied using different protocols. In the first protocol, each of the quantities $\hat{\dot{\gamma}}$, Δ_{xx}, Δ_{xy} and Δ_{yy} was perturbed with a randomly chosen initial condition of the form

$$\delta\mathbf{u}(0,y) = \nu\sum_{n=1}^{5}(\mathbf{A}_n/n^2)\cos(n\pi y), \tag{7.1}$$

where $\mathbf{u} \equiv [\widehat{\dot{\gamma}}, \Delta_{xx}, \Delta_{xy}, \Delta_{yy}]$. The components $A_{ni},\ i = 1,2,3,4$ of the vector of amplitudes $\mathbf{A}$ are chosen randomly from the interval $[-1,1]$. In this protocol, the perturbed quantity is initialised with Equation (7.1) such that the component A_{ni}

corresponding to the perturbed quantity is non zero, while the other components are set to zero. In the second protocol, all the quantities $\hat{\dot{\gamma}}$, Δ_{xx}, Δ_{xy} and Δ_{yy} were perturbed simultaneously with a random perturbation of the same form as Equation (7.1). In this case, the components A_{ni} corresponding to each quantity is non zero for all vectors $\mathbf{A}_n$. In the calculations presented in Chapter 6, a specific set of perturbations that yields fracture-like behaviour was applied simultaneously to all quantities. These perturbations are shown in Figure 6.1(c).

The kind of perturbations given in Equation (7.1) could come from various sources in an experiment. For example, some regions in a sample could still have finite stresses after loading in a rheometer. There could also be temperature gradients in the sample as experiments are not necessarily performed in isothermal conditions. All these perturbations have the possibility to grow if the material is unstable.

7.1 I: Perturbing Each Quantity Separately

In this case, one of the quantities $\widehat{\dot{\gamma}}$, Δ_{xx}, Δ_{xy} or, Δ_{yy} is initialized (one at a time) using a random perturbation of the form given in Equation (7.1). That is, initialize one of the quantities, such as $\widehat{\dot{\gamma}}(y,0) \neq 0$ while $\Delta_{xx}(y,0) = 0$, $\Delta_{xy}(y,0) = 0$ and $\Delta_{yy}(y,0) = 0$. To determine if 'fracture' has occurred or not, consider the 'velocity moments' $\mu_{\pm}$, defined by Equation (6.3) reproduced here for convenience

$$\mu_+ = \frac{\sum_i v_i H(v_i)}{\sum_i H(v_i)} \tag{7.2a}$$

$$\mu_- = \frac{\sum_i v_i H(-v_i)}{\sum_i H(-v_i)}, \tag{7.2b}$$

where the sum is over all spatial positions y_i and H is the Heaviside step function. If both positive moment μ_+ and negative moment μ_- occur together at any time during stress relaxation after shear cessation, then 'fracture' has occurred;

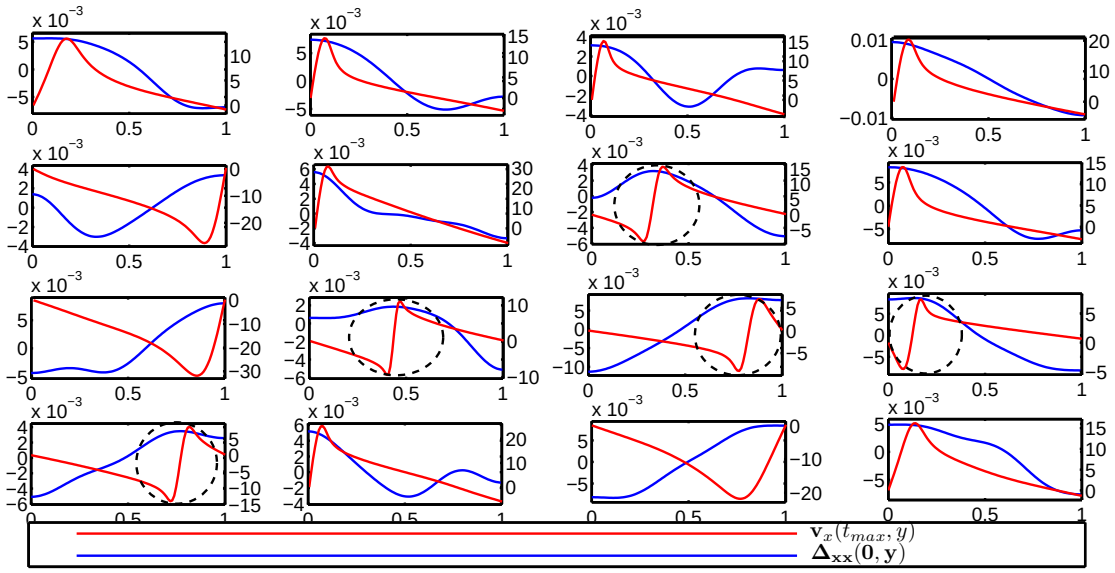

Figure 7.1: Recoil or 'fracture' for different random initial conditions upon perturbing Δ_{xx} In all cases, the blue line is the perturbation and the red line is the velocity profile when both $\mu_{\pm}$ reach their extrema together (for 'fracture') or $\mu_{\pm}$ reach their extrema separately (for recoil without 'fracture'). The 'fracture' profiles are indicated by the dashed circles. Left axis: perturbation; Right axis: velocity.

otherwise there is no 'fracture'.

The velocity profiles shown in Figures. 7.1 to 7.4 occur at the time when both μ_+ and μ_- reach their extrema for the case of 'fracture'. When there is no 'fracture', either μ_+ becomes non zero after shear cessation, but later relaxes to zero while $\mu_- = 0$ throughout the duration of stress relaxation from shear cessation; otherwise, μ_- becomes non zero after shear cessation, and later relaxes to zero while $\mu_+ = 0$ for the duration of stress relaxation after shear cessation. When there is no 'fracture' the velocity profiles are shown when either μ_+ reaches its maximum or μ_- reaches its minimum. When 'fracture' occurs, the position of the 'fracture' plane depends on the shape of the specific perturbation. The stress relaxation is independent of the position of the 'fracture' plane, similar to the report in section IIIA of [4].

Figures 7.1 and 7.2 shows that when the quantities Δ_{xx} or Δ_{yy} receive a perturbation of an appropriate shape then 'fracture' occurs after shear cessation. Otherwise there is no 'fracture'. However, Figure 7.3 shows that for the case of perturbing

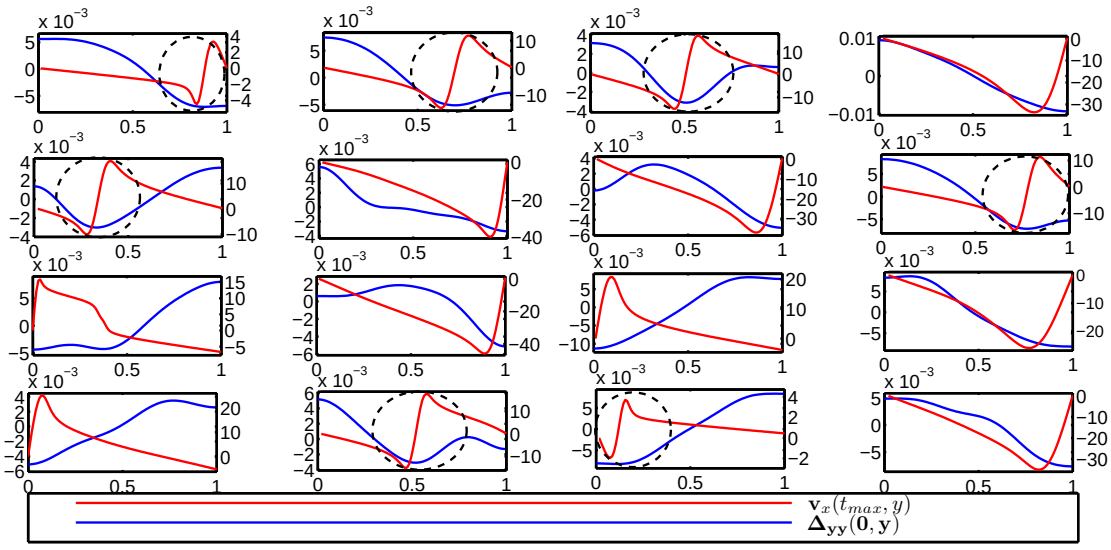

Figure 7.2: Same as Figure 7.1 but with perturbation to Δ_{yy}.

Δ_{xy}, only a weak 'fracture' is obtained for some shapes of the perturbation, while $\widehat{\dot{\gamma}}$ almost gives zero velocity for all shapes of the perturbation.

The zero response of the fluid to perturbations in $\widehat{\dot{\gamma}}$ can be understood from the contributions to the total stress as

$$\widehat{T}_{xy} = \Delta_{xy} + \epsilon\widehat{\dot{\gamma}}. \tag{7.3}$$

The 'Newtonian' contribution $\epsilon\widehat{\dot{\gamma}}$ is very small compared with Δ_{xy} since $\epsilon = 10^{-4}$. But since $\widehat{T}_{xy}$ is constant in space, then

$$\Delta_{xy} \sim \epsilon\widehat{\dot{\gamma}}. \tag{7.4}$$

The two terms balance each other to give a uniform $\widehat{T}_{xy}$ in space. Then a small perturbation in $\widehat{\dot{\gamma}}$ is scaled to nearly zero by ϵ. But a small perturbation in Δ_{xy} is amplified by ϵ to give a large response in $\widehat{\dot{\gamma}}$. This then creates a low viscosity in a narrow region if the response in $\widehat{\dot{\gamma}}$ is localised to that region. If this region of low viscosity occurs between two regions of high viscosity then an internal slip occurs which is the 'fracture' phenomenon. The reason why the components Δ_{xx}

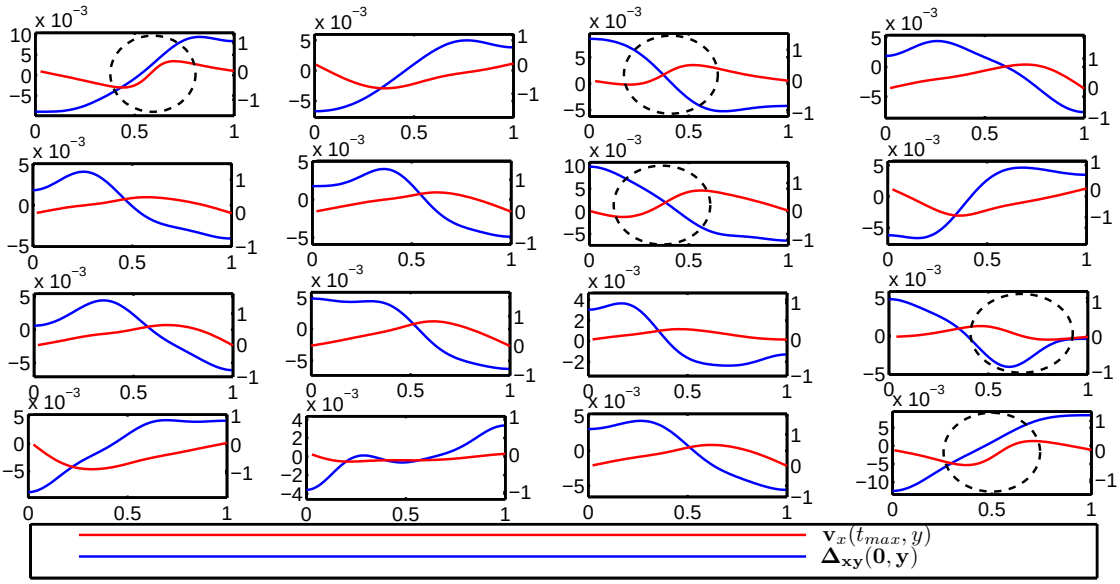

Figure 7.3: Perturbation of Δ_{xy}. Only a weak recoil or a weak sign of 'fracture' is seen in this case. The blue and red lines have the same meaning as in Fig. 7.1. The 'weak fracture' profiles are indicated by the dashed circles. Left axis: perturbation; Right axis: velocity.

and Δ_{yy} seem to be more effective in inducing 'fracture' will be discussed later in this Chapter after a linear stability analysis has been performed on the system.

7.2 II: Perturbing All Quantities Simultaneously

In this case all the quantities $\widehat{\dot{\gamma}}$, Δ_{xx}, Δ_{xy} and Δ_{yy} are initialised simultaneously with separate random perturbation of the form given in Equation (7.1). Similar to the previous protocol, the resultant velocity profile after shear cessation is checked for 'fracture' using the 'velocity moments' given in Equation (7.2). The situation in this case as shown in Figure 7.5 is more complex as each quantity receives a separate random perturbation of different shape. The cases where 'fracture' occur are marked with the dashed circles in the Figures. For detailed analysis of 'fracture', a set of initial conditions such as Subfigure (P_1) of Figure 7.5 which is known to give 'fracture' can be chosen to perform all the calculations required to probe the 'fracture' phenomenon.

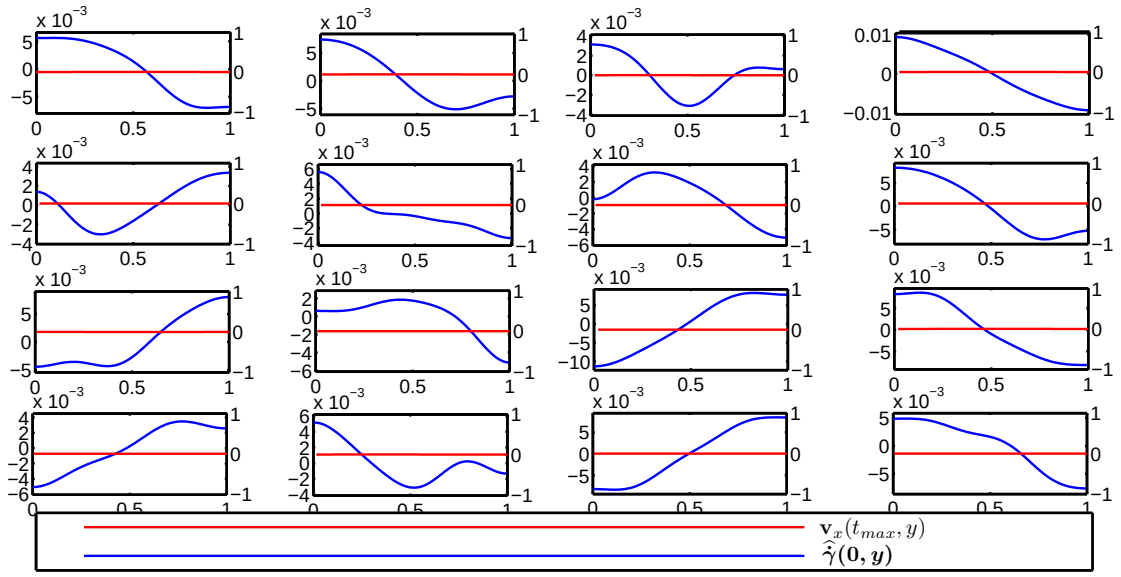

Figure 7.4: Same as Figure 7.3 but with perturbation to $\hat{\dot{\gamma}}$.

7.3 Instability

A brief overview of the two kinds of instabilities that could be encountered during shear deformation of polymeric fluids was given in Section 2.5. As mentioned before, the elastic instability occurs when the shear stress satisfies

$$\frac{\partial \hat{T}_{x,y}(t,\gamma)}{\partial \gamma} < 0, \tag{7.5}$$

while the viscous instability occurs when the shear stress satisfies

$$\frac{\partial \hat{T}_{x,y}(t,\hat{\dot{\gamma}})}{\partial \hat{\dot{\gamma}}} < 0. \tag{7.6}$$

However, in real step strain experiments the instabilities encountered is usually due to a combination of both effects [18]. The elastic and viscous contributions to the instability leading to the 'fracture' phenomenon shall be examined in the following sections.

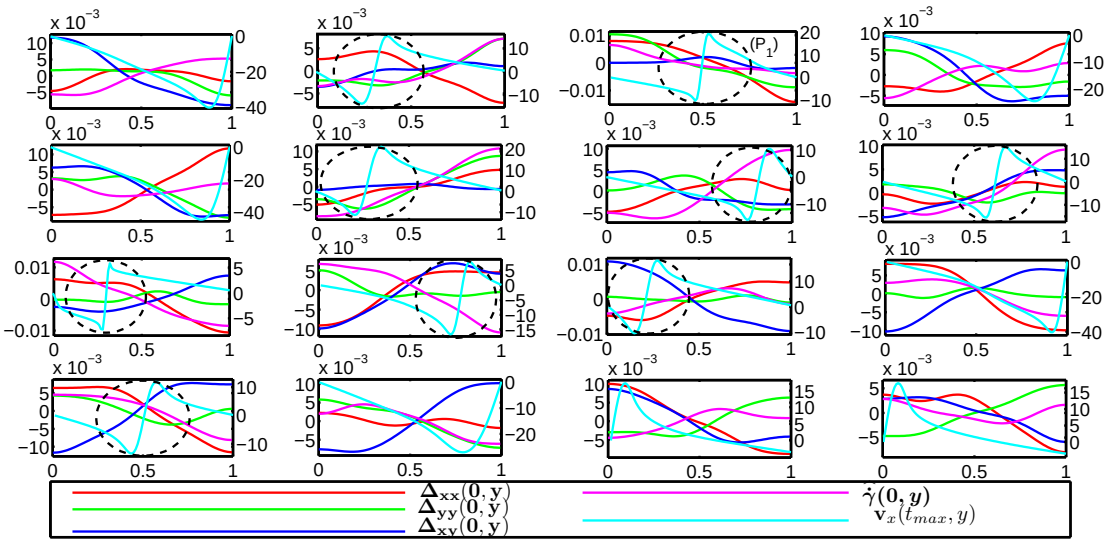

Figure 7.5: Recoil or 'fracture' upon perturbing all components, with each component receiving a separate random perturbation. Red line: perturbation to Δ_{xx}. Green line: perturbation to Δ_{yy}. Blue line: perturbation to Δ_{xy}. Magenta line: perturbation to $\dot{\gamma}$. Cyan line: recoil or 'fracture' velocity profile v. Left axis: perturbation; Right axis: velocity. In all cases, the velocity profiles occur at the time specified in Figure 7.1, and the 'fracture' profiles are indicated with the dashed circles.

7.4 Elastic Instability

The elastic contribution to the instability results in stress overshoots during rapid startups as in Figure 6.1(a). The origin of elastic instability was described by Marrucci and Grizzuti (MG) [16] in their calculations to explain the Type C 'anomaly', as discussed in Section 2.5. The basic idea comes from the principles of the tube theory which describes a two stage relaxation mechanism for the chain segments after a rapid step shear. The chain segments are initially oriented randomly in equilibrium before the deformation. The chain segments get aligned in the flow direction and stretched during the deformation. This stretching and subsequent relaxation after the deformation leads to a change in the length and number of chain segments. However, to simplify their calculation, MG assumed that the length and number of chain segments at the end of stretch relaxation were the same as their equilibrium values before the deformation was imposed. Hence they treated the

chain segments as a system of rigid rods which only respond to deformation by rotation without stretching. The free energy for this system of rigid rods in shear deformation is given as [16]

$$\mathcal{F}(\gamma) = \frac{1}{2}\int_0^1 \ln\left(\frac{1+\gamma^2\zeta^2+\left[\zeta^4(\gamma^4+4\gamma^2)-2\gamma^2\zeta^2+1\right]^{1/2}}{2}\right)d\zeta, \tag{7.7}$$

where ζ is an arbitrary integration variable and γ is the accumulated strain.

After stretch relaxation following a step strain, the tube segments can be treated as having approximately equal length. But the tube segments are still oriented in the flow direction and hence can be treated as a system of rigid rods which is described by the free energy function given in Equation (7.7) as shown in Figure 7.6(a). The curvature for this free energy function is given as [16]

$$\begin{aligned}\frac{d^2\mathcal{F}}{d\gamma^2} &= 2\int_0^1 \frac{\zeta^4\left(\gamma^2\zeta^2+1\right)}{h_f^3(\zeta)}d\zeta - \frac{1}{2\gamma^2}\int_0^1\left(1+\frac{\gamma^2\zeta^2-1}{h_f(\zeta)}\right)d\zeta \\ h_f(\zeta) &= \left[\zeta^4\left(\gamma^4+4\gamma^2\right)-2\gamma^2\zeta^2+1\right]^{1/2}.\end{aligned} \tag{7.8}$$

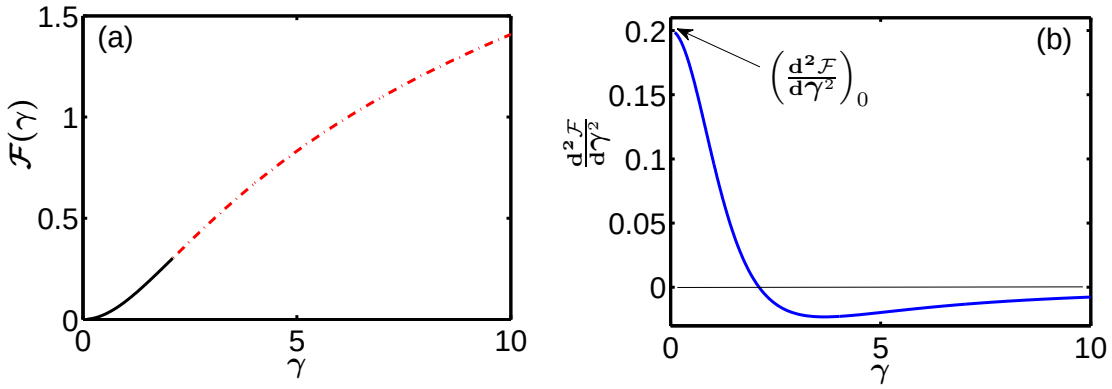

Figure 7.6: (a) The free energy function of a system of rigid rods aligned by an external shear deformation. The red dash-dot indicate where the curvature becomes negative. (b) Curvature of the free energy function in (a).

This curvature becomes negative as the strain increases as shown in Figure 7.6(b). The region of negative curvature of the free energy is shown by the red dash-dot line in Figure 7.6(a). As reptation proceeds, the tube segments which were

originally aligned in the flow direction become isotropic. Then the fluid behaves like a viscous liquid that is stable to perturbations. Hence, an otherwise unstable system regains stability. In the absence of reptation during stretch relaxation following a step strain, the occurrence of a negative curvature is sufficient to determine elastic instability. The condition $d^2\mathcal{F}/d\gamma^2 < 0$ corresponds to $\partial \hat{T}_{x,y}(t,\gamma)/\partial\gamma < 0$ [16, 18, 57, 61], so that the fluid goes unstable just at the stress overshoot during startup. However, some reptation usually accompanies stretch relaxation following a step strain, which has the effect of stabilizing an otherwise unstable system.

To account for the effect of reptation on elastic instability, MG introduced the effective curvature A^{eff}, which considers the fraction of tube segments still aligned anisotropically in the flow direction after stretch relaxation:

$$A^{eff} = \mu \underbrace{\left(\frac{d^2\mathcal{F}}{d\gamma^2}\right)_{\gamma}}_{I} + (1-\mu) \underbrace{\left(\frac{d^2\mathcal{F}}{d\gamma^2}\right)_{0}}_{II}. \tag{7.9}$$

where μ is the fraction of chain segments still aligned anisotropically in the flow direction. Elastic instability of the fluid to an imposed deformation is then determined by the occurrence of $A^{eff} < 0$.

To see this, note that at the end of stretch relaxation some amount of reptation had already occurred. Then only a fraction μ of the tube segments are still oriented in the flow direction at the end of stretch relaxation. A fraction $1-\mu$ had already become isotropic. The elastic fraction μ may become unstable depending on the applied strain. But the viscous fraction is always stable as seen in Figure 7.6(b). The contribution I to A^{eff} is either positive or negative depending on the applied strain, while the contribution II is strictly positive as in Figure 7.6(b). If the applied strain is such that I is negative with a larger magnitude than the contribution II then A^{eff} may become negative after stretch relaxation.

For the case where the contribution I to A^{eff} in Equation (7.9) is negative after stretch relaxation, the overall sign of A^{eff} is controlled by the parameter μ. When $\mu \approx 1$ after stretch relaxation and the contribution I is negative then A^{eff} becomes negative, otherwise it is positive. The magnitude of μ after stretch relaxation is determined by the amount of reptation which had occurred at that time. If only a little amount of reptation had occurred after stretch relaxation then $\mu \approx 1$, otherwise $\mu \ll 1$. How much reptation had occurred just after stretch relaxation depends on the separation of timescales for stretch relaxation and reptation. If the separation is large, then only a little amount of reptation would have occurred before stretch is completely relaxed, otherwise a significant amount of reptation would have occurred at the end of stretch relaxation. The separation of timescales for stretch relaxation and reptation is controlled by $Z = \tau_d/(3\tau_R)$. Hence, the elastic instability does not show up at small values of Z. This leads to the lower cut-off for Z seen in Figure 6.12(b) repeated in Figure 7.7(a) for convenience.

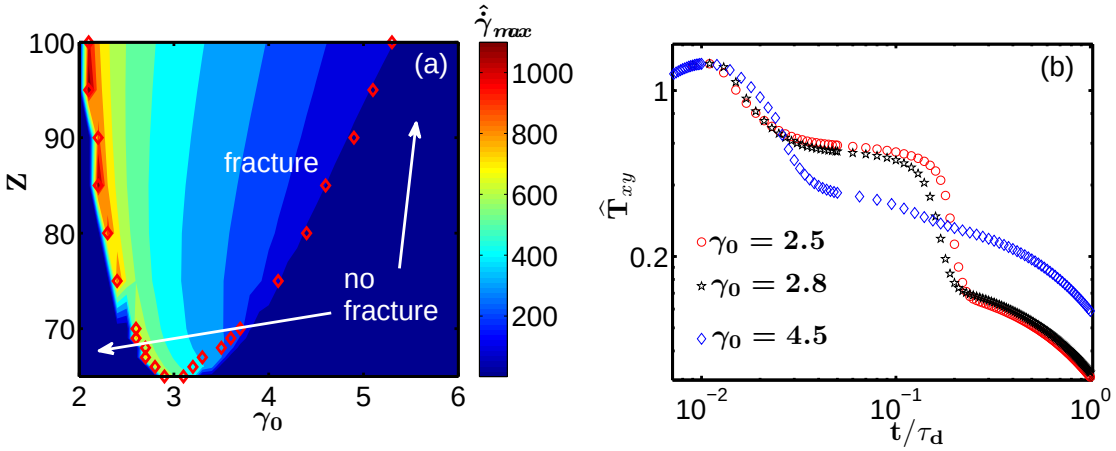

Figure 7.7: Range of Z and γ_0 for which 'fracture' occurs exhibiting a lower cut-off in Z. Parameters: $\langle\hat{\dot{\gamma}}\rangle = 200$, $\epsilon = 10^{-4}$, $\widehat{\mathcal{D}} = 10^{-5}$ and $\beta = 0$.

At low values of applied strain $A^{eff} > 0$ since I is positive at low strains in Equation (7.9). At higher applied strains I becomes negative, but its magnitude decreases as the applied strain is increased as seen in Figure 7.6(b). Hence, at higher strains $A^{eff} > 0$ at the end of stretch relaxation due to the effect of μ in

Equation (7.7). This explains why 'fracture' only occurs at intermediate strains as seen in Figure 7.7(a). This also explains why the 'induction time' becomes negligible at high strains as in the case of $\gamma_0 = 4.5$ in Figure 7.7(b), and why the type C behaviour is only observed at intermediate strains [16].

The original formulation by Marrucci and Grizzuti [16] used a form of the relaxation function μ that assumes uniform deformation and relaxation of the material. With an initial perturbation, the material will not necessarily deform or relax uniformly. Also, the dynamics for the DRP model is not exactly the same as that of the original DE model for which μ was employed. Hence it is necessary to compute a new representation for μ which does not assume homogeneity, and consistent with the dynamics of the DRP model.

7.4.1 Deformed Chains

All chains that are still oriented anistropically in the flow direction are still in the deformed state; they only become isotropic with some random orientation after reptation has completed. To compute this fraction of deformed chains, consider a blob of fluid roughly in the shape of an ellipsoid (an ellipse in 2 dimensions) due to the deformation, as shown in Figure 7.8. Its degree of deviation from isotropy can be quantified by $|\lambda_1 - \lambda_2|$, where λ_1 and λ_2 are the eigenvalues of the dimensionless strain tensor $\mathbf{W}$. Since μ is the fraction of chains still aligned in the flow direction, it meets the requirement

$$\mu \in [0, 1]. \tag{7.10}$$

Hence μ can be represented as

$$\mu = \frac{|\lambda_1 - \lambda_2|}{|\lambda_1 + \lambda_2|}. \tag{7.11}$$

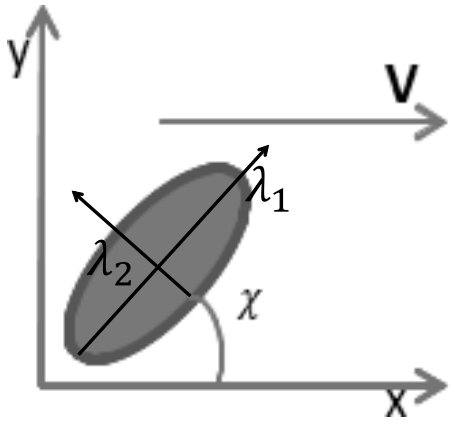

Figure 7.8: Approximate representation of entangled chains by an ellipsoidal blob.

In the isotropic state $\lambda_1 = \lambda_2$ and $\mu = 0$, while in a state of high degree of deformation, $\lambda_1 \gg \lambda_2$ and $\mu \approx 1$. using

$$\left(\frac{\lambda_1 - \lambda_2}{\lambda_1 + \lambda_2}\right)^2 = \frac{(\lambda_1 + \lambda_2)^2 - 4\lambda_1\lambda_2}{(\lambda_1 + \lambda_2)^2}, \tag{7.12}$$

and the following properties of diagonalizable matrices [62]

$$\begin{aligned} \lambda_1 + \lambda_2 &= \mathrm{tr}(\mathbf{W}) \\ \lambda_1\lambda_2 &= \det(\mathbf{W}), \end{aligned} \tag{7.13}$$

then

$$\mu = \left|\frac{\lambda_1 - \lambda_2}{\lambda_1 + \lambda_2}\right| = \sqrt{1 - \frac{4\det(\mathbf{W})}{(\mathrm{tr}(\mathbf{W}))^2}}, \tag{7.14}$$

which allows the computation of the effective curvature given in Equation (7.9).

7.4.2 Validity of the Relaxation Function

In the original formulation of the effective curvature, Marrucci and Grizzuti [16] defined the relaxation function $\mu(t)$ as

$$\mu_{MG}(t) = \frac{8}{\pi^2} \sum_{p}^{odd} \frac{1}{p^2} \exp\left(-tp^2/\tau_d\right), \tag{7.15}$$

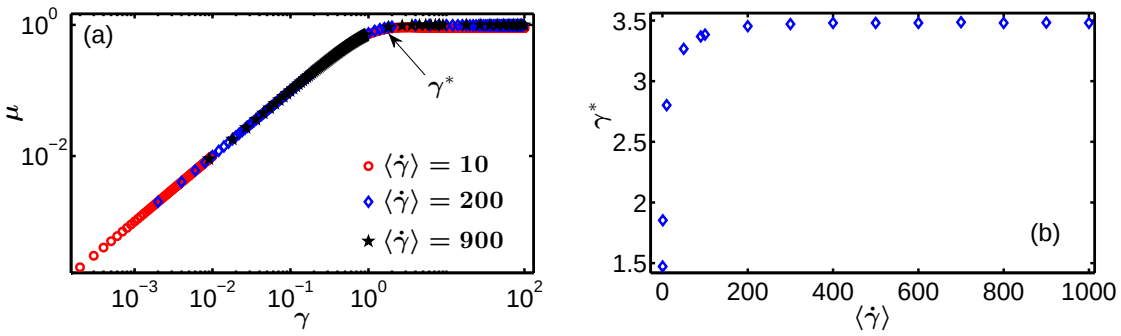

Figure 7.9: (a) Evolution of the relaxation function μ with shear strain at the applied shear rates indicated in the Figure. The relaxation function becomes strain independent at some critical shear strain γ^* as indicated in the Figure. (b) Behaviour of the critical strain with applied shear rate. The critical strain forms a plateau at intermediate and high shear rates.

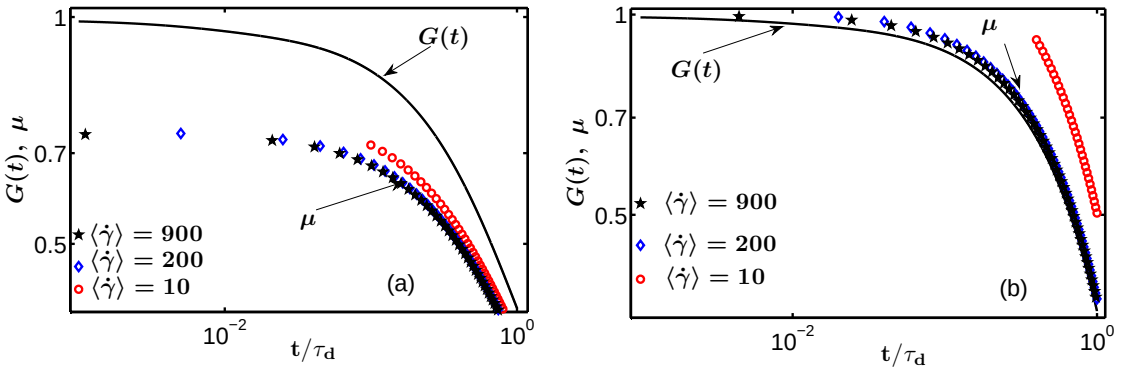

Figure 7.10: (a) Comparison of the relaxation function (symbols, for $\gamma_0 = 1$) with the linear relaxation modulus (solid line, for $\gamma_0 = 0.2$) at the applied shear rates indicated in the Figure. The applied strain $\gamma_0 = 1 < \gamma^*$. (b) Same as in (a) for $\gamma_0 = 4 > \gamma^*$

where τ_d is reptation time. Equation (7.15) (which was also used in the DE theory [13]) is just the de Gennes expression for the relaxation modulus scaled by the plateau modulus G_N^0 [7, 10],

$$G(t) = G_N^0 \mu_{MG}(t). \tag{7.16}$$

It is not apparent that the relaxation function as given by Equation (7.14) is strain independent as in the case of Equation (7.15). However, Figure 7.9(a) shows that μ becomes strain independent at some critical strain γ^*. Figure 7.9(b) shows that

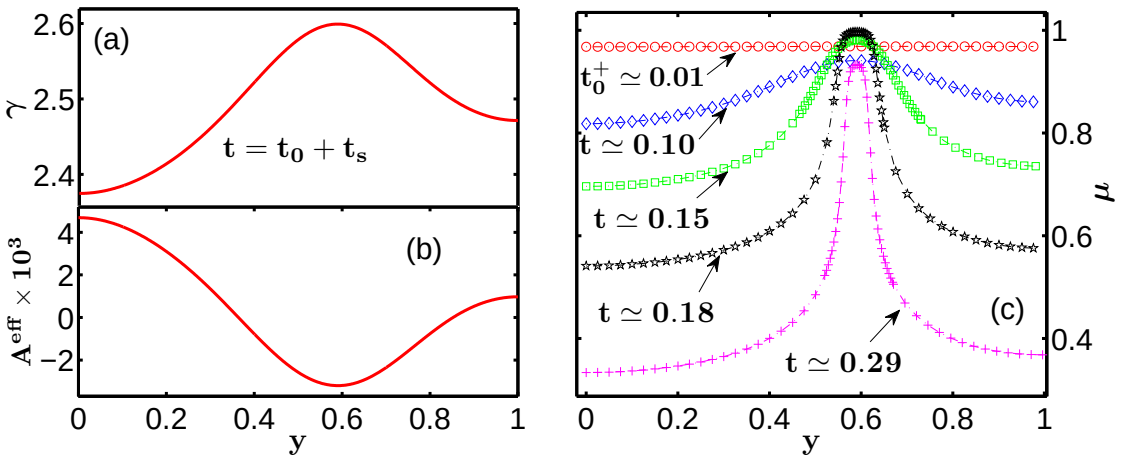

Figure 7.11: Spatial profiles of (a) strain and (b) effective curvature at the time of stretch relaxation $t_0 + t_s$ for $\gamma_0 = 2.5$. (c) Fraction of deformed chains μ just after shear cessation and during 'fracture' for $\langle\dot{\widehat{\gamma}}\rangle = 200$ and $\gamma_0 = 2.5$.

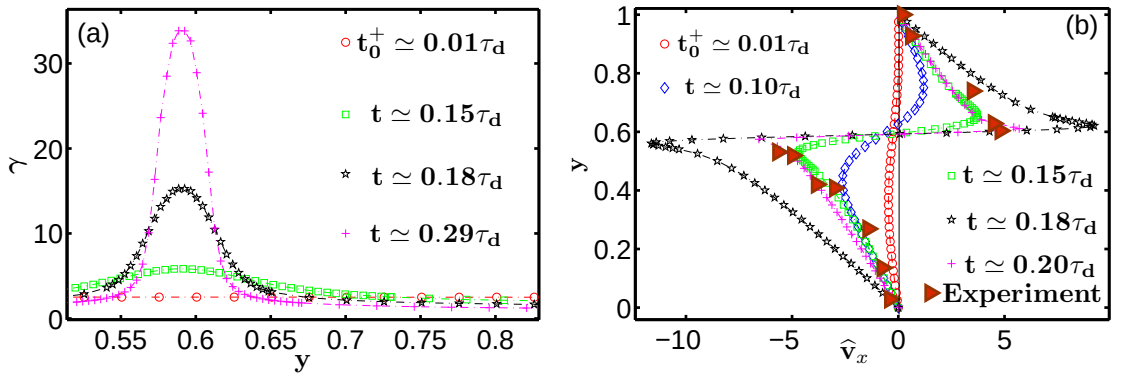

Figure 7.12: (a) Localisation of strain in the slip layer from the inhomogeneous strain profile in Figure 7.11(a). (b) Fluid velocity showing fracture-like behaviour due to strain localisation.

γ^* initially increases at low applied shear rates (applied shear rates $\langle\dot{\widehat{\gamma}}\rangle$, such that $\langle\dot{\widehat{\gamma}}\rangle\tau_R < 1$). It then forms a plateau at intermediate and high applied shear rates (applied shear rates $\langle\dot{\widehat{\gamma}}\rangle$, such that $\langle\dot{\widehat{\gamma}}\rangle\tau_R \gtrsim 1$). The critical strain is of order 3 for these shear rates. This value lies in the 'fracture' region as in Figure 7.7(a).

For applied strains $\gamma_0 < \gamma^*$, the relaxation function falls below the linear relaxation modulus for the low, intermediate and high shear rate regimes as in Figure 7.10(a). However, for $\gamma_0 > \gamma^*$, only the intermediate and high shear rate regimes give a close match to the linear relaxation modulus as in Figure 7.10(b). The relaxation function for the low shear rate regime shows a significant deviation

from the linear relaxation modulus. Hence, the definition of the relaxation function given in Equation (7.14) is only valid at an applied shear rate $\langle\widehat{\dot{\gamma}}\rangle$, such that $\langle\widehat{\dot{\gamma}}\rangle\tau_R \approx 1$, and strains $\gamma_0 \gtrsim \gamma^*$.

For Case I discussed in Section 6.1, where $\langle\widehat{\dot{\gamma}}\rangle > 1$, $\langle\widehat{\dot{\gamma}}\rangle\tau_R \simeq 1$ and $\gamma_0 = 2.5$, Figures 7.11(ab) show that the local maximum in the strain (induced by the initial perturbation in Figure 6.1(c)) after stretch relaxation in turn induces a local minimum in the effective curvature at $y \simeq 0.6$. Figure 7.11(b) shows that this region of local minimum in A^{eff} is negative, which is an indication of elastic instability. This situation allows localisation of strain around this region as seen in Figure 7.12(a) which leads to the 'fracture' event shown in Figure 7.12(b). Figure 7.11(c) shows that during this 'fracture' event the chains in the internal slip layer become strongly anisotropic, before gradually regaining isotropy so that the slip comes to a halt. Quiescent stress relaxation resumes at the end of this internal slip.

7.5 Linear Stability Analysis

The relaxation function as defined in Equation (7.14) is only valid for applied shear rates $\langle\widehat{\dot{\gamma}}\rangle$, such that $\langle\widehat{\dot{\gamma}}\rangle\tau_R \simeq 1$, and strains $\gamma_0 > \gamma^*$. This is the regime where the elastic nature of the fluid is dominant. However, experiments [4] have shown that the 'fracture' phenomenon is realisable for applied shear rates $\langle\widehat{\dot{\gamma}}\rangle\tau_R < 1$ and strains of order 1. This situation is shown in Figures 6.10(b) and 6.11(b). The calculations in Figures 6.10(a) and 6.11(a) show that the theoretical model can also capture this 'fracture' phenomenon in this low shear rate regime. Hence it is necessary to employ some other technique to determine if the fluid may still be unstable to fluctuations in this low shear rate and strain regime.

The procedure to be employed here will be to consider a base state made of the quantities in Equation (4.17) which have been constrained to be homogeneous in space. Then at every time step during the evolution of this base state, a linear

stability analysis will be performed to determine if this base state will permit growth of infinitesimal fluctuations if shearing is stopped at that time. This linear stability analysis will reveal if the fluid could develop this fracture-like behaviour when shearing is stopped at some time t_0 such that $\gamma_0 < \gamma^*$ for the applied shear rate. The linear stability analysis will also reveal if the fluid could develop fracture-like behaviour for low applied shear rates. This comes from the fact that a fluid which permits growth of infinitesimal fluctuations at any time t_0 for any applied shear rate may develop fracture-like behaviour after shearing is stopped at t_0, as long as the fluctuations have sufficient time to grow and initiate 'strain localisation' in the bulk of the fluid before other nonlinear effects suppress the growth of these fluctuations.

7.5.1 Linearized Equations

The base state $\mathbf{u} \equiv [\widehat{\dot{\gamma}}, \overline{\Delta}_{xx}, \overline{\Delta}_{xy}, \overline{\Delta}_{yy}]$ which has been constrained to be homogeneous in space can be constructed from Equation (4.17) as

$$\partial_t \overline{\Delta}_{xx} = 2\overline{\Delta}_{xy}\widehat{\dot{\gamma}} - \overline{\Delta}_{xx} - \frac{2\tau_d}{\tau_R}\left[1-\overline{A}\right]\left[\left(\beta\overline{A}+1\right)\overline{\Delta}_{xx}+1\right] \tag{7.17a}$$

$$\partial_t \overline{\Delta}_{xy} = \widehat{\dot{\gamma}} + \widehat{\dot{\gamma}}\,\overline{\Delta}_{yy} - \overline{\Delta}_{xy} - \frac{2\tau_d}{\tau_R}\left[1-\overline{A}\right]\left(\beta\overline{A}+1\right)\overline{\Delta}_{xy} \tag{7.17b}$$

$$\partial_t \overline{\Delta}_{yy} = -\overline{\Delta}_{yy} - \frac{2\tau_d}{\tau_R}\left[1-\overline{A}\right]\left[\left(\beta\overline{A}+1\right)\overline{\Delta}_{yy}+1\right] \tag{7.17c}$$

$$\overline{A} = \left(1 + \frac{\mathrm{Tr}\overline{\boldsymbol{\Delta}}}{3}\right)^{-1/2}. \tag{7.17d}$$

At time t_0 an inhomogeneous perturbation $\delta\mathbf{u}(t, y)$ is imposed on this base state. The inhomogeneous perturbation can be separated into a time varying function

$\delta\mathbf{u}(t)$ and fluctuations in the velocity gradient direction as [58, 59]

$$\begin{aligned}\delta\mathbf{u}(t,y) &= \sum_k \delta\mathbf{u}_k(t)\exp(iky), \quad t \geq t_0 \\ k &= n\pi, \quad n \in [0,+\infty).\end{aligned} \tag{7.18}$$

Then the quantity $\widetilde{\mathbf{u}}(t,y)$ describing the evolution of the perturbation can then be written as

$$\widetilde{\mathbf{u}}(t,y) = \mathbf{u}(t_0) + \delta\mathbf{u}(t,y), \quad t \geq t_0, \tag{7.19}$$

which can be obtained from Equation (4.17). Substituting Equations (7.19) and (7.18) into Equation (4.17) gives

$$\begin{aligned}\partial_t\delta\Delta_{xx,k}(t) =& 2\overline{\Delta}_{xy}\delta\dot{\gamma}_k(t) + 2\overline{\dot{\gamma}}\delta\Delta_{xy,k}(t) - \delta\Delta_{xx,k}(t) - \frac{\tau_d}{3\tau_R}\left[(\overline{A}^3\delta\Delta_{xx,k}(t) + \right. \\ & \left.\overline{A}^3\delta\Delta_{yy,k}(t))\right] + \frac{\tau_d}{3\tau_R}\overline{\Delta}_{xx}\left[(\beta-1)\left(\overline{A}^3\delta\Delta_{xx,k}(t) + \overline{A}^3\delta\Delta_{yy,k}(t)\right)\right] \\ & - \frac{2\tau_d}{\tau_R}\delta\Delta_{xx,k}(t)\left[1+(\beta-1)\,\overline{A}\right] - \frac{2}{3}\beta\overline{\Delta}_{xx}\left(\overline{A}^4\delta\Delta_{xx,k}(t) + \overline{A}^4\delta\Delta_{yy,k}(t)\right) \\ & 2\overline{A}^2\beta\delta\Delta_{xx,k}(t) - \widehat{\mathscr{D}}k^2\delta\Delta_{xx,k}(t)\end{aligned} \tag{7.20a}$$

$$\begin{aligned}\partial_t\delta\Delta_{xy,k}(t) =& -\delta\Delta_{xy,k}(t) + \delta\dot{\gamma}_k(t) + \overline{\dot{\gamma}}\delta\Delta_{yy,k}(t) + \overline{\Delta}_{yy}\delta\dot{\gamma}_k(t) + \frac{\tau_d}{3\tau_R}\overline{\Delta}_{xy}\left[(\beta-1)\left(\overline{A}^3\times\right.\right. \\ & \left.\left.\delta\Delta_{xx,k}(t) + \overline{A}^3\delta\Delta_{yy,k}(t)\right)\right] - \frac{2\tau_d}{\tau_R}\delta\Delta_{xy,k}(t)\left[1+(\beta-1)\,\overline{A}\right] \\ & - \frac{2\beta\tau_d}{3\tau_R}\overline{\Delta}_{xy}\left(\overline{A}^4\delta\Delta_{xx,k}(t) + \overline{A}^4\delta\Delta_{yy,k}(t)\right) + \overline{A}^2\frac{2\beta\tau_d}{\tau_R}\delta\Delta_{xy,k}(t) \\ & - \widehat{\mathscr{D}}k^2\delta\Delta_{xy,k}(t)\end{aligned} \tag{7.20b}$$

$$\begin{aligned}\partial_t\delta\Delta_{yy,k}(t) =& -\delta\Delta_{yy,k}(t) - \frac{\tau_d}{3\tau_R}\left[\left(\overline{A}^3\delta\Delta_{xx,k}(t) + \overline{A}^3\delta\Delta_{yy,k}(t)\right)\right] + \\ & \frac{\tau_d}{3\tau_R}\overline{\Delta}_{yy}\left[(\beta-1)\left(\overline{A}^3\delta\Delta_{xx,k}(t) + \overline{A}^3\delta\Delta_{yy,k}(t)\right)\right] - \frac{2\tau_d}{\tau_R}\delta\Delta_{yy,k}(t)\,[1+ \\ & (\beta-1)\,\overline{A}] + \frac{2\beta\tau_d}{\tau_R}\overline{\Delta}_{yy}\left(-\frac{1}{3}\overline{A}^4\delta\Delta_{xx,k}(t) - \frac{1}{3}\overline{A}^4\delta\Delta_{yy,k}(t)\right) + \\ & \frac{2\beta\tau_d}{\tau_R}\overline{A}^2\delta\Delta_{yy,k}(t) - \widehat{\mathscr{D}}k^2\delta\Delta_{yy,k}(t)\end{aligned} \tag{7.20c}$$

$$\partial_t\delta\dot{\gamma}_k(t) = -\frac{k^2}{\rho}\delta\Delta_{xy,k}(t) - \frac{k^2\epsilon}{\rho}\delta\dot{\gamma}_k(t). \tag{7.20d}$$

Rearranging Equations (7.20) gives

$$\begin{aligned}
\partial_t \delta\Delta_{xx,k}(t) = &\left[\frac{\tau_d}{3\tau_R}\overline{\Delta}_{xx}\left(\beta-1\right)\overline{A}^3 - 1 - \frac{\tau_d}{3\tau_R}\overline{A}^3 - 2\frac{\tau_d}{\tau_R}\left[1+\left(\beta-1\right)\overline{A}\right] - \frac{2}{3}\beta\overline{\Delta}_{xx}\overline{A}^4\right.\\
&\left.+2\beta\overline{A}^2 - k^2\widehat{\mathcal{D}}\right]\delta\Delta_{xx,k}(t)\\
&+ 2\widehat{\dot{\overline{\gamma}}}\delta\Delta_{xy,k}(t)\\
&+ \left[\left(\beta-1\right)\frac{\tau_d}{3\tau_R}\overline{\Delta}_{xx}\overline{A}^3 - \frac{\tau_d}{3\tau_R}\overline{A}^3 - \frac{2}{3}\beta\overline{\Delta}_{xx}\overline{A}^4\right]\delta\Delta_{yy,k}(t)\\
&+ 2\overline{\Delta}_{xy}\delta\widehat{\dot{\gamma}}_k(t) \qquad (7.21a)\\
\partial_t \delta\Delta_{xy,k}(t) = &\left[\left(\beta-1\right)\frac{\tau_d}{3\tau_R}\overline{\Delta}_{xy}\overline{A}^3 - \frac{2}{3}\beta\frac{\tau_d}{\tau_R}\overline{A}^4\overline{\Delta}_{xy}\right]\delta\Delta_{xx,k}(t)\\
&+ \left[2\beta\frac{\tau_d}{\tau_R}\overline{A}^2 - 1 - 2\frac{\tau_d}{\tau_R}\left[1+\left(\beta-1\right)\overline{A}\right] - k^2\widehat{\mathcal{D}}\right]\delta\Delta_{xy,k}(t)\\
&+ \left[\widehat{\dot{\overline{\gamma}}} + \left(\beta-1\right)\frac{\tau_d}{3\tau_R}\overline{\Delta}_{xy}\overline{A}^3 - \frac{2}{3}\beta\frac{\tau_d}{\tau_R}\overline{\Delta}_{xy}\overline{A}^4\right]\delta\Delta_{yy,k}(t)\\
&+ \left[1+\overline{\Delta}_{yy}\right]\delta\widehat{\dot{\gamma}}_k(t) \qquad (7.21b)\\
\partial_t \delta\Delta_{yy,k}(t) = &\left[\left(\beta-1\right)\frac{\tau_d}{3\tau_R}\overline{\Delta}_{yy}\overline{A}^3 - \frac{\tau_d}{3\tau_R}\overline{A}^3 - \frac{2}{3}\beta\frac{\tau_d}{\tau_R}\overline{\Delta}_{yy}\overline{A}^4\right]\delta\Delta_{xx,k}(t)\\
&+ \left[\frac{\tau_d}{3\tau_R}\left(\beta-1\right)\overline{\Delta}_{yy}\overline{A}^3 - 1 - \frac{\tau_d}{3\tau_R}\overline{A}^3 - 2\frac{\tau_d}{\tau_R}\left[1+\left(\beta-1\right)\overline{A}\right] - \frac{2}{3}\beta\frac{\tau_d}{\tau_R}\overline{\Delta}_{yy}\overline{A}^4\right.\\
&\left.+2\beta\frac{\tau_d}{\tau_R}\overline{A}^2 - k^2\widehat{\mathcal{D}}\right]\delta\Delta_{yy,k}(t) \qquad (7.21c)\\
\partial_t \delta\widehat{\dot{\gamma}}_k(t) = &-\frac{k^2}{\widehat{\rho}}\delta\Delta_{xy,k}(t) - \frac{k^2\epsilon}{\widehat{\rho}}\delta\widehat{\dot{\gamma}}_k(t), \qquad (7.21d)
\end{aligned}$$

where

$$\epsilon = \frac{\eta}{G\tau_d} \qquad (7.22a)$$

$$\widehat{\rho} = \frac{\rho L^2}{G\tau_d^2}. \qquad (7.22b)$$

In the zero Reynolds number limit $\hat{\rho} \to 0$ Equation (7.21) reduces to

$$\begin{aligned}
\partial_t \delta\Delta_{xx,k}(t) = &\left[\frac{\tau_d}{3\tau_R}\overline{\Delta}_{xx}(\beta-1)\overline{A}^3 - 1 - \frac{\tau_d}{3\tau_R}\overline{A}^3 - 2\frac{\tau_d}{\tau_R}\left[1+(\beta-1)\overline{A}\right] - \frac{2}{3}\beta\overline{\Delta}_{xx}\overline{A}^4 + 2\beta\overline{A}^2\right. \\
&\left. -k^2\widehat{\mathcal{D}}\right]\delta\Delta_{xx,k}(t) \\
&+ 2\left[\widehat{\dot{\overline{\gamma}}} - \frac{\overline{\Delta}_{xy}}{\epsilon}\right]\delta\Delta_{xy,k}(t) \\
&+ \left[(\beta-1)\frac{\tau_d}{3\tau_R}\overline{\Delta}_{xx}\overline{A}^3 - \frac{\tau_d}{3\tau_R}\overline{A}^3 - \frac{2}{3}\beta\overline{\Delta}_{xx}\overline{A}^4\right]\delta\Delta_{yy,k}(t) \qquad (7.23a) \\
\partial_t \delta\Delta_{xy,k}(t) = &\left[(\beta-1)\frac{\tau_d}{3\tau_R}\overline{\Delta}_{xy}\overline{A}^3 - \frac{2}{3}\beta\frac{\tau_d}{\tau_R}\overline{A}^4\overline{\Delta}_{xy}\right]\delta\Delta_{xx,k}(t) \\
&+ \left[2\beta\frac{\tau_d}{\tau_R}\overline{A}^2 - 1 - 2\frac{\tau_d}{\tau_R}\left[1+(\beta-1)\overline{A}\right] - \frac{1+\overline{\Delta}_{yy}}{\epsilon} - k^2\widehat{\mathcal{D}}\right]\delta\Delta_{xy,k}(t) \\
&+ \left[\widehat{\dot{\overline{\gamma}}} + (\beta-1)\frac{\tau_d}{3\tau_R}\overline{\Delta}_{xy}\overline{A}^3 - \frac{2}{3}\beta\frac{\tau_d}{\tau_R}\overline{\Delta}_{xy}\overline{A}^4\right]\delta\Delta_{yy,k}(t) \qquad (7.23b) \\
\partial_t \delta\Delta_{yy,k}(t) = &\left[(\beta-1)\frac{\tau_d}{3\tau_R}\overline{\Delta}_{yy}\overline{A}^3 - \frac{\tau_d}{3\tau_R}\overline{A}^3 - \frac{2}{3}\beta\frac{\tau_d}{\tau_R}\overline{\Delta}_{yy}\overline{A}^4\right]\delta\Delta_{xx,k}(t) \\
&+ \left[\frac{\tau_d}{3\tau_R}(\beta-1)\overline{\Delta}_{yy}\overline{A}^3 - 1 - \frac{\tau_d}{3\tau_R}\overline{A}^3 - 2\frac{\tau_d}{\tau_R}\left[1+(\beta-1)\overline{A}\right] - \frac{2}{3}\beta\frac{\tau_d}{\tau_R}\overline{\Delta}_{yy}\overline{A}^4\right. \\
&\left. +2\beta\frac{\tau_d}{\tau_R}\overline{A}^2 - k^2\widehat{\mathcal{D}}\right]\delta\Delta_{yy,k}(t) \qquad (7.23c)
\end{aligned}$$

Equation (7.21d) allows $\delta\widehat{\dot{\gamma}}_k(t)$ to be calculated from $\delta\Delta_{xy,k}(t)$ as

$$\delta\widehat{\dot{\gamma}}_k(t) = -\frac{\delta\Delta_{xy,k}(t)}{\epsilon} \qquad (7.24)$$

Equation (7.23) shows that the k dependence of the perturbations only come from the diffusivity $\widehat{\mathcal{D}}$. Equation (7.23) is just a homogeneous system of linear ordinary differential equations which can be written more conveniently as

$$\begin{aligned}
\frac{d\delta\Delta_{xx,k}}{dt} &= \alpha_1\delta\Delta_{xx,k}(t) + \alpha_2\delta\Delta_{xy,k}(t) + \alpha_3\delta\Delta_{yy,k}(t) \qquad (7.25a) \\
\frac{d\delta\Delta_{xy,k}}{dt} &= \alpha_4\delta\Delta_{xx,k}(t) + \alpha_5\delta\Delta_{xy,k}(t) + \alpha_6\delta\Delta_{yy,k}(t) \qquad (7.25b) \\
\frac{d\delta\Delta_{yy,k}}{dt} &= \alpha_7\delta\Delta_{xx,k}(t) + \alpha_8\delta\Delta_{yy,k}(t), \qquad (7.25c)
\end{aligned}$$

where

$$\alpha_1 = \frac{\tau_d}{3\tau_R}\overline{\Delta}_{xx}\left(\beta-1\right)\overline{A}^3 - 1 - \frac{\tau_d}{3\tau_R}\overline{A}^3 - 2\frac{\tau_d}{\tau_R}\left[1+\left(\beta-1\right)\overline{A}\right] - \frac{2}{3}\beta\overline{\Delta}_{xx}\overline{A}^4 + 2\beta\overline{A}^2 - k^2\widehat{\mathcal{D}} \tag{7.26a}$$

$$\alpha_2 = 2\left[\widehat{\dot{\overline{\gamma}}} - \frac{\overline{\Delta}_{xy}}{\epsilon}\right] \tag{7.26b}$$

$$\alpha_3 = \left(\beta-1\right)\frac{\tau_d}{3\tau_R}\overline{\Delta}_{xx}\overline{A}^3 - \frac{\tau_d}{3\tau_R}\overline{A}^3 - \frac{2}{3}\beta\overline{\Delta}_{xx}\overline{A}^4 \tag{7.26c}$$

$$\alpha_4 = \left(\beta-1\right)\frac{\tau_d}{3\tau_R}\overline{\Delta}_{xy}\overline{A}^3 - \frac{2}{3}\beta\frac{\tau_d}{\tau_R}\overline{A}^4\overline{\Delta}_{xy} \tag{7.26d}$$

$$\alpha_5 = 2\beta\frac{\tau_d}{\tau_R}\overline{A}^2 - 1 - 2\frac{\tau_d}{\tau_R}\left[1+\left(\beta-1\right)\overline{A}\right] - \frac{1+\overline{\Delta}_{yy}}{\epsilon} - k^2\widehat{\mathcal{D}} \tag{7.26e}$$

$$\alpha_6 = \widehat{\dot{\overline{\gamma}}} + \left(\beta-1\right)\frac{\tau_d}{3\tau_R}\overline{\Delta}_{xy}\overline{A}^3 - \frac{2}{3}\beta\frac{\tau_d}{\tau_R}\overline{\Delta}_{xy}\overline{A}^4 \tag{7.26f}$$

$$\alpha_7 = \left(\beta-1\right)\frac{\tau_d}{3\tau_R}\overline{\Delta}_{yy}\overline{A}^3 - \frac{\tau_d}{3\tau_R}\overline{A}^3 - \frac{2}{3}\beta\frac{\tau_d}{\tau_R}\overline{\Delta}_{yy}\overline{A}^4 \tag{7.26g}$$

$$\alpha_8 = \frac{\tau_d}{3\tau_R}\left(\beta-1\right)\overline{\Delta}_{yy}\overline{A}^3 - 1 - \frac{\tau_d}{3\tau_R}\overline{A}^3 - 2\frac{\tau_d}{\tau_R}\left[1+\left(\beta-1\right)\overline{A}\right] - \frac{2}{3}\beta\frac{\tau_d}{\tau_R}\overline{\Delta}_{yy}\overline{A}^4 + 2\beta\frac{\tau_d}{\tau_R}\overline{A}^2 - k^2\widehat{\mathcal{D}}. \tag{7.26h}$$

Equation (7.25) can be written in matrix form as

$$\frac{d\delta\widetilde{\mathbf{w}}}{dt} = \mathsf{M}\cdot\delta\widetilde{\mathbf{w}}(\mathbf{t}), \tag{7.27}$$

where $\widetilde{\mathbf{w}} = [\Delta_{xx}, \Delta_{xy}, \Delta_{yy}]$. The matrix M is given as

$$\mathsf{M} = \begin{pmatrix} \alpha_1 & \alpha_2 & \alpha_3 \\ \alpha_4 & \alpha_5 & \alpha_6 \\ \alpha_7 & 0 & \alpha_8 \end{pmatrix} = \begin{pmatrix} \alpha_1' - k^2\widehat{\mathcal{D}} & \alpha_2 & \alpha_3 \\ \alpha_4 & \alpha_5' - k^2\widehat{\mathcal{D}} & \alpha_6 \\ \alpha_7 & 0 & \alpha_8' - k^2\widehat{\mathcal{D}} \end{pmatrix}, \tag{7.28}$$

where

$$\alpha_1' = \alpha_1 + k^2\widehat{\mathcal{D}} \tag{7.29a}$$

$$\alpha_5' = \alpha_5 + k^2\widehat{\mathcal{D}} \tag{7.29b}$$

$$\alpha_8' = \alpha_8 + k^2\widehat{\mathcal{D}}. \tag{7.29c}$$

Then Equation (7.28) can be written as

$$\mathsf{M} = \widetilde{\mathsf{M}} - k^2\widehat{\mathcal{D}}\mathbf{I}, \tag{7.30}$$

where

$$\widetilde{\mathsf{M}} = \begin{pmatrix} \alpha_1' & \alpha_2 & \alpha_3 \\ \alpha_4 & \alpha_5' & \alpha_6 \\ \alpha_7 & 0 & \alpha_8' \end{pmatrix}, \tag{7.31}$$

and $\mathbf{I}$ is the identity matrix of order 3.

Using the operator

$$D \equiv \frac{d}{dt} \tag{7.32}$$

in Equation (7.25) gives

$$\delta\Delta_{xx} = \frac{1}{\alpha_7}\left[D\delta\Delta_{yy} - \alpha_8\delta\Delta_{yy}\right] \tag{7.33a}$$

$$\delta\Delta_{xy} = \frac{1}{\alpha_2\alpha_7}\left[D^2\delta\Delta_{yy} - (\alpha_1+\alpha_8)D\delta\Delta_{yy} + (\alpha_1\alpha_8 - \alpha_3\alpha_7)\delta\Delta_{yy}\right], \tag{7.33b}$$

which together with Equation (7.25) gives

$$D^3\delta\Delta_{yy} - \widetilde{\alpha}_1 D^2\delta\Delta_{yy} + \widetilde{\alpha}_2 D\delta\Delta_{yy} + \widetilde{\alpha}_3\delta\Delta_{yy} = 0, \tag{7.34}$$

where

$$\widetilde{\alpha}_1 = \alpha_1 + \alpha_5 + \alpha_8 \tag{7.35a}$$

$$\widetilde{\alpha}_2 = \alpha_1\alpha_5 + \alpha_5\alpha_8 + \alpha_1\alpha_8 - \alpha_3\alpha_7 - \alpha_2\alpha_4 \tag{7.35b}$$

$$\widetilde{\alpha}_3 = \alpha_2\alpha_4\alpha_8 + \alpha_3\alpha_5\alpha_7 - \alpha_2\alpha_6\alpha_7 - \alpha_1\alpha_5\alpha_8. \tag{7.35c}$$

Equation (7.34) is just a linear homogeneous ordinary differential equation whose solution can be obtained from the solution of the characteristic equation [63]

$$m^3 - \widetilde{\alpha}_1 m^2 + \widetilde{\alpha}_2 m + \widetilde{\alpha}_3 = 0. \tag{7.36}$$

If the solutions of the cubic Equation (7.36) are ω_1, ω_2 and ω_3, then the solution of Equation (7.34) is given as [63]

$$\delta\Delta_{yy} = k_1 e^{\omega_1 t} + k_2 e^{\omega_2 t} + k_3 e^{\omega_3 t}, \tag{7.37}$$

where k_1, k_2 and k_3 are arbitrary integration constants. Using Equations (7.37) and (7.33) give

$$\delta\Delta_{xx} = \frac{1}{\alpha_7}\left[k_1(\omega_1 - \alpha_8)e^{\omega_1 t} + k_2(\omega_2 - \alpha_8)e^{\omega_2 t} + k_3(\omega_3 - \alpha_8)e^{\omega_3 t}\right] \tag{7.38a}$$

$$\begin{aligned}\delta\Delta_{yy} = \frac{1}{\alpha_2\alpha_7}\Big[&\left(k_1\omega_1^2 - (\alpha_1 + \alpha_8)k_1\omega_1 + (\alpha_1\alpha_8 - \alpha_3\alpha_7)k_1\right)e^{\omega_1 t} + \left(k_2\omega_2^2 - \right.\\ &\left.(\alpha_1 + \alpha_8)k_2\omega_2 + (\alpha_1\alpha_8 - \alpha_3\alpha_7)k_2\right)e^{\omega_2 t} + \left(k_3\omega_3^2 - (\alpha_1 + \alpha_8)k_3\omega_3 + \right.\\ &\left.(\alpha_1\alpha_8 - \alpha_3\alpha_7)k_3\right)e^{\omega_3 t}\Big].\end{aligned} \tag{7.38b}$$

Hence, the perturbation $\delta\widetilde{\mathbf{w}}(t)$ in Equation (7.27) can be written as

$$\delta\widetilde{\mathbf{w}}(t) = \sum_{i=1}^{3} \widetilde{\mathbf{v}}_i e^{\omega_i t}, \tag{7.39}$$

where

$$\widetilde{\mathbf{v}}_1 = \begin{pmatrix} \frac{1}{\alpha_7} k_1(\omega_1 - \alpha_8) \\ \frac{1}{\alpha_2\alpha_7}\left(k_1\omega_1^2 - (\alpha_1+\alpha_8)k_1\omega_1 + (\alpha_1\alpha_8 - \alpha_3\alpha_7)k_1\right) \\ k_1 \end{pmatrix} = \begin{pmatrix} \widetilde{v}_{1xx} \\ \widetilde{v}_{1xy} \\ \widetilde{v}_{1yy} \end{pmatrix}, \tag{7.40}$$

$$\widetilde{\mathbf{v}}_2 = \begin{pmatrix} \frac{1}{\alpha_7} k_2(\omega_2 - \alpha_8) \\ \frac{1}{\alpha_2\alpha_7}\left(k_2\omega_2^2 - (\alpha_1+\alpha_8)k_2\omega_2 + (\alpha_1\alpha_8 - \alpha_3\alpha_7)k_2\right) \\ k_2 \end{pmatrix} = \begin{pmatrix} \widetilde{v}_{2xx} \\ \widetilde{v}_{2xy} \\ \widetilde{v}_{2yy} \end{pmatrix} \tag{7.41}$$

and

$$\widetilde{\mathbf{v}}_3 = \begin{pmatrix} \frac{1}{\alpha_7} k_3(\omega_3 - \alpha_8) \\ \frac{1}{\alpha_2\alpha_7}\left(k_3\omega_3^2 - (\alpha_1+\alpha_8)k_3\omega_3 + (\alpha_1\alpha_8 - \alpha_3\alpha_7)k_3\right) \\ k_3 \end{pmatrix} = \begin{pmatrix} \widetilde{v}_{3xx} \\ \widetilde{v}_{3xy} \\ \widetilde{v}_{3yy} \end{pmatrix}. \tag{7.42}$$

Substituting Equation (7.39) into Equation (7.27) gives

$$\frac{d\delta\widetilde{\mathbf{w}}}{dt} = \sum_{i=1}^{3} \omega_i \widetilde{\mathbf{v}}_i e^{\omega_i t} = \mathsf{M}\delta\widetilde{\mathbf{w}}(\mathbf{t}) = \sum_{i=1}^{3} \mathsf{M}\widetilde{\mathbf{v}}_i e^{\omega_i t}, \tag{7.43}$$

so that

$$\widetilde{\mathbf{v}}_i\omega_i = \mathsf{M}\widetilde{\mathbf{v}}_i. \tag{7.44}$$

Hence, the roots of the characteristic Equation (7.36) are the eigenvalues of the matrix M (stability matrix), and $\widetilde{\mathbf{v}}_i$ are the corresponding eigenvectors. Thus the perturbations $\delta\Delta_{xx}$, $\delta\Delta_{xy}$ and $\delta\Delta_{yy}$ can be written as linear combinations of the

eigenvectors as

$$\delta\Delta_{xx} = \widetilde{v}_{1xx}e^{\omega_1 t} + \widetilde{v}_{2xx}e^{\omega_2 t} + \widetilde{v}_{3xx}e^{\omega_3 t} \tag{7.45a}$$

$$\delta\Delta_{xy} = \widetilde{v}_{1xy}e^{\omega_1 t} + \widetilde{v}_{2xy}e^{\omega_2 t} + \widetilde{v}_{3xy}e^{\omega_3 t} \tag{7.45b}$$

$$\delta\Delta_{yy} = \widetilde{v}_{1yy}e^{\omega_1 t} + \widetilde{v}_{2yy}e^{\omega_2 t} + \widetilde{v}_{3yy}e^{\omega_3 t}. \tag{7.45c}$$

The growth or decay of these perturbations will then be determined by the nature of the eigenvalues. Since these eigenvalues are solutions of a cubic equation, then at least one of them is real. If complex eigenvalues occur, then they must be complex conjugates. If the largest real part of an eigenvalue ω_{max} just becomes positive then the perturbations in Equation (7.45) will grow unbounded. This will happen for any infinitesimal perturbation.

Equation (7.30) shows that the eigenvalues of M are just the eigenvalues of $\widetilde{\mathsf{M}}$ with $k^2\widehat{\mathcal{D}}$ subtracted from them. Hence the fluid is more stable to perturbations with higher wavenumbers k since the wavenumbers have a stabilising effect. Thus the $k = 0$ mode is the most unstable mode in the system.

7.5.2 Dispersion Relation

The dispersion relation is obtained by sweeping through the constitutive curve shown by the red circles in Figure 7.13(a) using a spectrum of Fourier modes of different wave numbers $k = n\pi$, $n = 0, \ldots, L/a_d$, where L is the gap size between the plates and a_d is the tube diameter discussed in Chapter 4. The wavenumbers correspond to waves whose wavelengths range from values below the tube diameter, through the gap size between the plates and up to several orders of magnitude larger than the tube diameter. The fluctuations in the system will be a superposition of these modes. In this case, the perturbation $\delta\mathbf{u}(t, y)$ is imposed on the base state

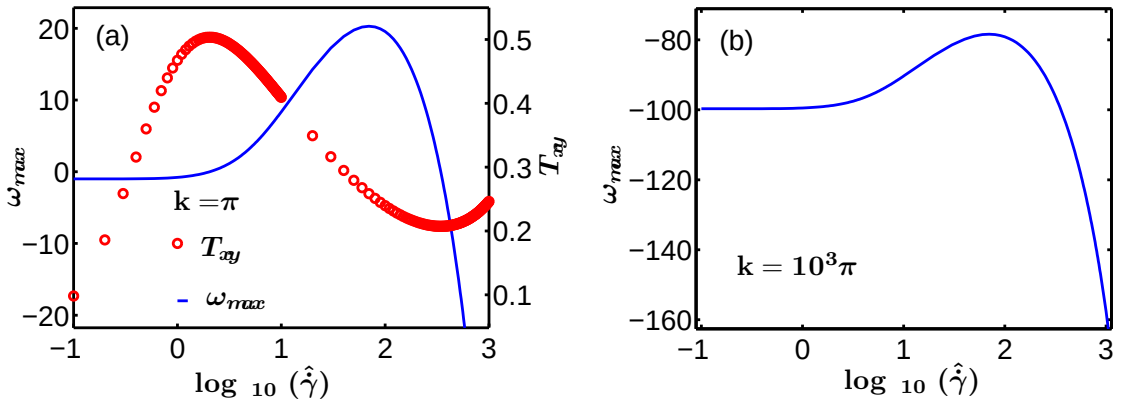

Figure 7.13: (a) Maximum real part ω_{max} of eigenvalues of stability matrix M for $k = \pi$ (solid line) for different shear rates. Steady state constitutive curve (red circles) for the same range of shear rates. (a) Same as the solid line in (a) for the mode number $k = 10^3\pi$.

u after the base state has evolved for a very long time such that it reaches steady state. The largest real part of the eigenvalues obtained for different values of $\langle\hat{\dot{\gamma}}\rangle$ for modes with $k = \pi$ and $k = 10^3\pi$ are shown in Figures 7.13(ab).

For the low wavenumber $k = \pi$, the fluid is stable at low and high shear rates, but unstable at intermediate shear rates as shown by the solid line in Figure 7.13(a). The range of shear rates where the fluid goes unstable at steady state nearly matches the range of shear rates where the steady state constitutive curve decreases with increasing shear rate as shown by the red circles in Figure 7.13(a). However, the fluid is stable at all shear rates for the mode with large wavenumber $k = 10^3\pi$ as in Figure 7.13(b). This is due to the stabilising effect of k in Equation 7.30.

Although the $k = 0$ mode is the most unstable according to Equation (7.30), the gap size between the plates is equal to 1. Hence the smallest mode which can fit between the plates is the $k = \pi$ mode. Thus all subsequent analysis in this Chapter will be performed with the $k = \pi$ mode.

7.6 Spinodal

Figure 7.13(a) shows that the fluid goes unstable at steady state for intermediate shear rates. However, this instability does not show up immediately from startup. The fluid needs to be sheared for some time at the imposed shear rate before the instability shows up. In other words, the instability shows up after some critical strain is reached for the applied shear rate in this intermediate regime. Also, for the high shear rate regime where the fluid is stable at steady state (Figure 7.13(a)), it is not always stable from startup to steady state. It goes unstable at some intermediate strains before regaining stability at large strains.

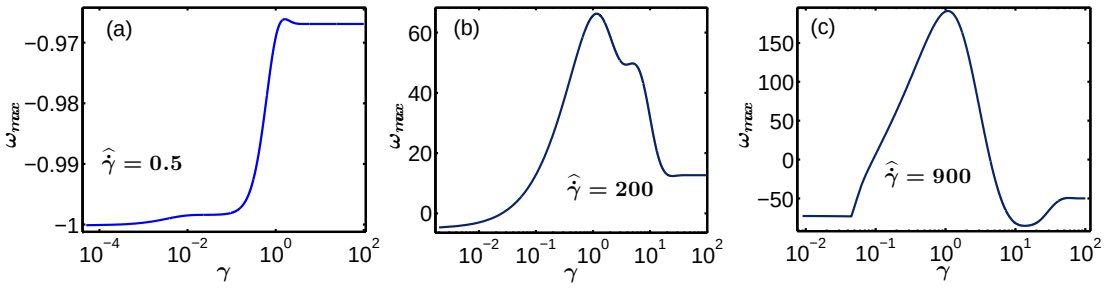

Figure 7.14: (abc) Largest real part of eigenvalues ω_{max} for the mode with $k = \pi$ as a function of strain for the applied shear rates indicated in the Figures.

This situation is shown in Figures 7.14(abc). For the applied shear rate $\dot{\hat{\gamma}} = 0.5 < 1$, the fluid remains stable at all strains as in Figure 7.14(a). However, for the intermediate shear rate $\dot{\hat{\gamma}} = 200 > 1$, the fluid is initially stable from startup before going unstable as the strain increases as in Figure 7.14(b). The fluid then remains unstable at higher strains until it reaches the steady state as in Figures 7.13(a) and 7.14(b). In the case of the high shear rate regime where $\dot{\hat{\gamma}} = 900 \gg 1$, the fluid is initially stable from startup, before going through a regime of instability at intermediate strains, and finally regaining stability at high strain until it reaches steady state as in Figures 7.13(a) and 7.14(c). The corresponding shear stresses at the critical strains at which the fluid goes unstable for different applied shear rates are shown by the blue diamonds in Figure 7.15. The locus of

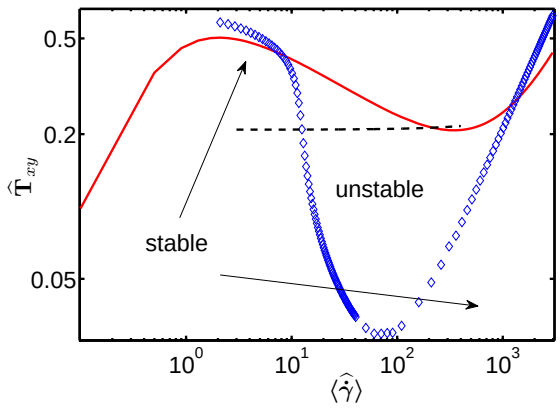

Figure 7.15: Blue diamonds: Spinodal (shear stress at which the homogeneous state goes unstable). Red solid line: Constitutive curve. Black dashed line: Stress plateau for the DRP model with $\beta = 0$, $Z = 72$.

these stresses is referred to as the spinodal [58, 59]. The range of shear rates at which the fluid goes unstable nearly matches the range of shear rates where the steady state constitutive curve decreases with increasing shear rate as shown by the red solid line in Figure 7.15. This is similar to the situation in Figure 7.13(a). The range of shear rates where the fluid goes unstable also nearly matches the range of shear rates where the shear stress from the same fluid (with non zero stress diffusivity) forms a plateau at steady state. The stress plateau is shown by the dashed lines in Figure 7.15. The intermediate shear rate regime where $\widehat{\dot{\gamma}} > 1$, where the fluid remains unstable (for $k = \pi$) until the steady state lies in the region where Equation (7.6) is satisfied as seen in Figure 7.13(a). This is an indication of a viscous contribution to the instability [18].

7.7 Viscous contribution to instability

Figures 7.14(abc) show that the fluid only shows a regime of instability when the applied shear rate $\widehat{\dot{\gamma}} > 1$. In particular, the intermediate shear rate regime where the instability persists until the steady state is reached is the regime where Equation (7.6) is satisfied. This indicates that there is a viscous contribution to the

instability that gives rise to the 'fracture' phenomenon. It is for this reason that the 'fracture' phenomenon is still realisable for intermediate shear rates such that $\langle\widehat{\dot{\gamma}}\rangle > 1$ and $\langle\widehat{\dot{\gamma}}\rangle\tau_R < 1$ as in Case III of Chapter 6 as shown in Figure 7.16(c). In Figures 7.16(abc), the black dots in ω_{max} are the stable part of the eigenvalue, while the red dashed lines in ω_{max} are the unstable part of the eigenvalue. Figures 7.16(abc) show that the fluid has already moved into the unstable regime before shear cessation for the three Cases I, II and III discussed in Chapter 6. For Cases I and III, the applied shear rates put the shear stress in the regime where viscous effect is significant as specified in Equation (7.6), and seen in Figure 7.15. However, for Case II, the applied shear rate does not satisfy Equation (7.6), but the applied strain of $\gamma_0 = 2.5$ lies in the unstable regime as seen in Figures 7.14(c) and 7.16(b). Also, the applied shear rate satisfies $\langle\widehat{\dot{\gamma}}\rangle\tau_R > 1$. Hence there may still be contributions from both viscous and elastic effects. It is not clear at this stage where the boundaries between the viscous and elastic effects lie.

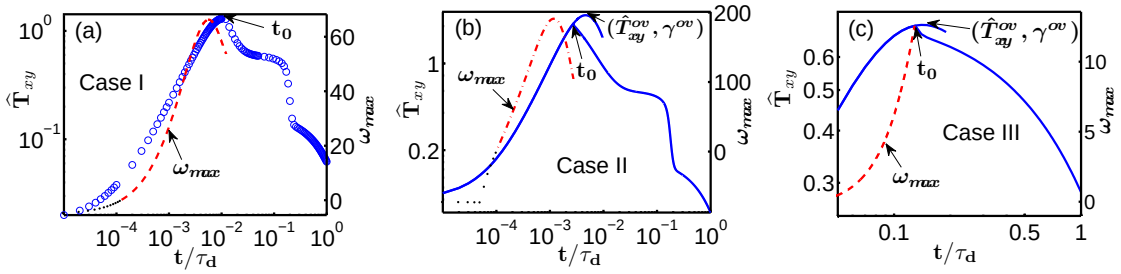

Figure 7.16: Shear stresses from startup to shear cessation at t_0 and beyond for applied shear rate and strain (a) $(\langle\widehat{\dot{\gamma}}\rangle, \gamma_0) = (200, 2.5)$, (b) $(\langle\widehat{\dot{\gamma}}\rangle, \gamma_0) = (900, 2.5)$ and (c) $(\langle\widehat{\dot{\gamma}}\rangle, \gamma_0) = (10, 1.3)$. The largest real parts of the eigenvalues ω_{max} for the stability matrices constructed at each time step are shown. The times at which $\omega_{max} < 0$ are indicated by the black dots, while $\omega_{max} > 0$ are indicated by the red dashed lines.

The relaxation of stress at the end of stretch relaxation is strictly due to reptation in the absence of any internal slip. If there is a growing perturbation, this relaxation by reptation competes with it. To determine the region in space where the instability grows fastest, consider the base state $\mathbf{u}$ at each point in space. Then

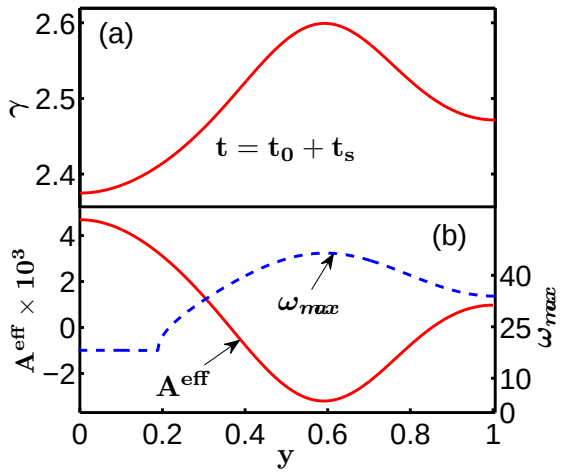

Figure 7.17: Spatial profiles of (a) Strain and (b) Effective curvature and ω_{max} for $\widetilde{\mathbf{u}}$ just after stretch relaxation. For $\beta = 0$, $Z = 72$, $\langle\hat{\dot{\gamma}}\rangle = 200$, $\gamma_0 = 2.5$.

an eigenvalue analysis can be carried out at each point in space. The eigenvalues of the stability matrices (at a particular time) at each point in space will then contain information regarding where in space a particular mode is growing fastest. The region in space where the unstable mode grows fastest is dictated by the strain. This is shown in Figures 7.17(ab) which shows that the instability grows fastest in the region where a local maximum in strain occurs. This matches the region where the local minimum in the effective curvature occurs as seen in Figure 7.17(b). Hence both the elastic and viscous contributions to the instability are most significant in the same region in space as dictated by the strain profile. This then determines the physical location of 'fracture'.

7.8 Eigenvectors

The linear stability analysis also gives insight into the behaviour of the system when the quantities $\dot{\gamma}$, Δ_{xx}, Δ_{xy} and Δ_{yy} are perturbed separately. Consider the base state $\mathbf{u}$ at the point in space where the shear rate is maximum at the end of stretch relaxation. The eigenvector $\widetilde{\mathbf{v}}_m$ corresponding to the largest real eigenvalue is heavily dominated by the Δ_{xx} and Δ_{yy} components. The result is

Table 7.1: Components of most unstable eigenvector $\widetilde{\mathbf{v}}_m$ for 15 different initial conditions, for $\langle\hat{\dot{\gamma}}\rangle = 200$, $\gamma_0 = 2.5$.

Initial Condition	$\widetilde{v}_{mxx}$	$\widetilde{v}_{mxy}$	$\widetilde{v}_{myy}$
1	0.9657	-0.0115	-0.2594
2	0.9767	-0.0131	-0.2144
3	0.9678	-0.0118	-0.2516
4	0.9730	-0.0125	-0.2304
5	0.9632	-0.0112	-0.2687
6	0.9667	-0.0117	-0.2555
7	0.9678	-0.0118	-0.2513
8	0.9636	-0.0113	-0.2672
9	0.9739	-0.0127	-0.2266
10	0.9683	-0.0119	-0.2496
11	0.9675	-0.0118	-0.2524
12	0.9742	-0.0127	-0.2255
13	0.9666	-0.0116	-0.2562
14	0.9613	-0.0110	-0.2753
15	0.9596	-0.0109	-0.2812

consistent for 15 different initial conditions that give fracture-like profile. The components of $\widetilde{\mathbf{v}}_m$ corresponding to Δ_{xx} ($\widetilde{\mathbf{v}}_{mxx}$), Δ_{xy} ($\widetilde{\mathbf{v}}_{mxy}$) and Δ_{yy} ($\widetilde{\mathbf{v}}_{myy}$) are shown in Table 7.1. The Table shows why the fluid does not 'fracture' when Δ_{xy} is perturbed separately. Since $\widetilde{\mathbf{v}}_m$ is heavily weighted by $\widetilde{\mathbf{v}}_{mxx}$ and $\widetilde{\mathbf{v}}_{myy}$, then $\delta\Delta_{xx}$ or $\delta\Delta_{yy}$ will grow much more for a positive eigenvalue and perturbation amplitude due to the representation of the perturbations in Equation (7.45). Hence perturbing the components Δ_{xy} separately does not induce 'fracture' (as in Figure 7.3) as compared with perturbing the components Δ_{xx} and Δ_{yy} separately at the same amplitude (as in Figures 7.1 and 7.2).

7.9 Growth of Perturbations

Some insights into the development of the fracture-like profile can be obtained by looking at the growth of the perturbations obtained from the linearized Equa-

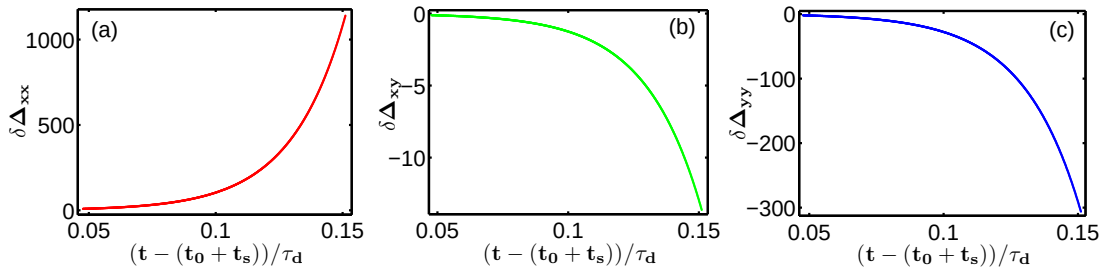

Figure 7.18: Growth of perturbations (a) $\delta\Delta_{xx}$, (b) $\delta\Delta_{xy}$ and (c) $\delta\Delta_{yy}$ for $\nu = 0.01$ predicted by the linear stability analysis. Parameters: $\langle\widehat{\dot{\gamma}}\rangle = 200$, $\gamma_0 = 2.5$ and $Z = 72$.

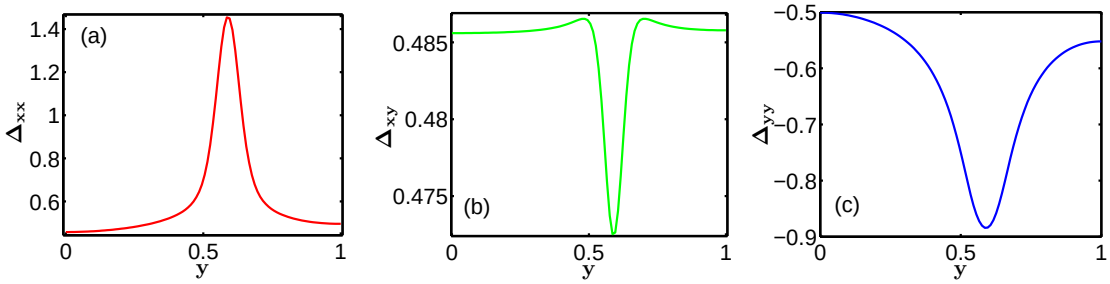

Figure 7.19: Spatial profiles of the stress components (a) Δ_{xx}, (b) Δ_{xy} and (c) Δ_{yy} at the peak of 'fracture' for $\nu = 0.01$. Parameters: same as in Figure 7.19.

tions (7.23). This is achieved by analysing the base state $\mathbf{u}$ at the point in space where the shear rate is maximum at the end of stretch relaxation. The time evolution of any perturbation given to $\mathbf{u}$ is described by Equation (7.45). For $\langle\widehat{\dot{\gamma}}\rangle = 200$ and $\gamma_0 = 2.5$, Figures 7.18(abc) show that these perturbations grow unbounded for $\nu = 0.01$ in Equation (7.1). The direction of growth of the perturbations are consistent with the shapes of the stress components at the peak of 'fracture' as shown in Figures 7.19(abc). This leads to the shear stress profile in Figure 7.20(a) which shows the unusual fast relaxation at intermediate times associated with 'fracture'. However, for $\nu = 0.005$ and $\langle\widehat{\dot{\gamma}}\rangle = 200$, $\gamma_0 = 2.5$, Figures 7.21(abc) show that the perturbation still grow unbounded, but the shear stress only relaxes quiescently as in Figure 7.20(b). This shows that the perturbation amplitude needs to reach some critical amount for the perturbation to win the competition against reptation. This nonlinear effect is not contained contained in the linearized Equations (7.23).

This linear stability analysis also throws some light into why the 'induction

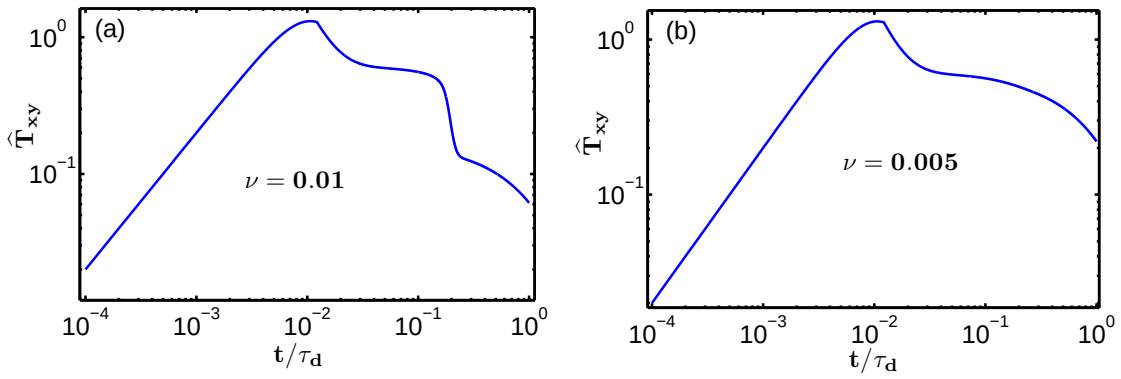

Figure 7.20: Shear stress evolution for (a) $\nu = 0.01$ and (b) $\nu = 0.005$. Parameters: same as in Figure 7.19.

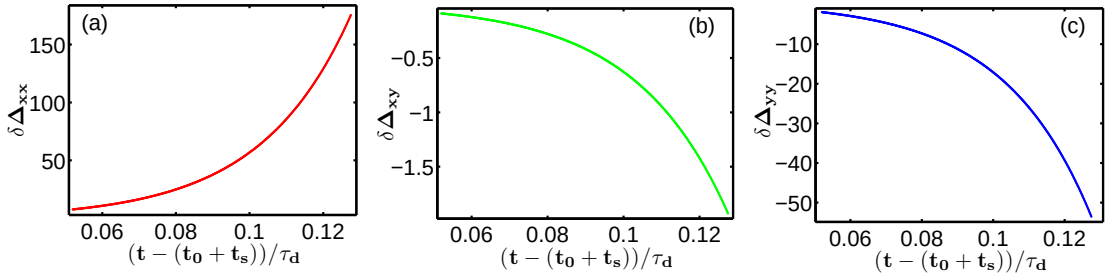

Figure 7.21: Same as Figure 7.15 for $\nu = 0.005$.

time' decreases with increasing Z as discussed in the previous Chapter. The perturbations grow faster as Z increases as shown in Figures 7.22(abc). The faster these perturbations grow, the faster they induce 'strain localisation', so that 'fracture' develops more quickly. This leads to the reduction in the 'induction time' as Z is increased as shown in Figure 7.23.

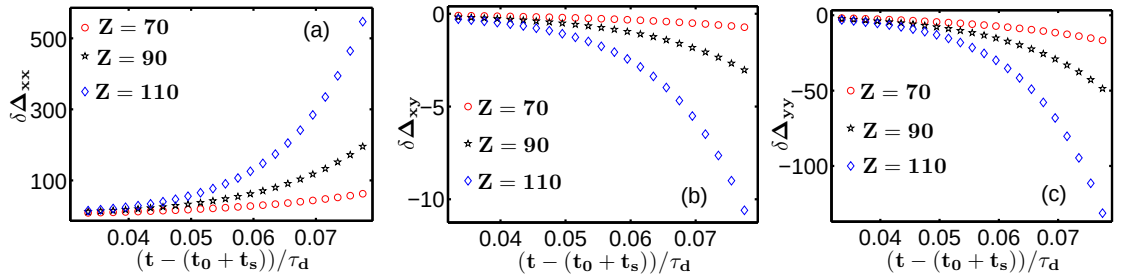

Figure 7.22: Same as Figure 7.15 for different values of Z indicated in the Figures.

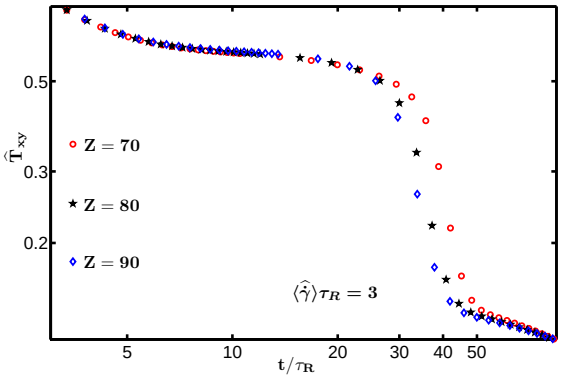

Figure 7.23: Stress relaxation after step shear for different values of Z, and $\langle\hat{\dot{\gamma}}\rangle\tau_R \approx 3$ as indicated in the Figure. Parameters: $\langle\hat{\dot{\gamma}}\rangle = 200$, $\gamma_0 = 2.5$ and $\nu = 0.01$.

7.10 Mechanism of Fracture

The mechanism of the 'fracture' phenomenon will now be summarized in this Section based on the calculations which have been presented so far. Although it is not so clear where the boundaries between the elastic and viscous contributions lie, there will be an attempt to discuss both contributions separately.

7.10.1 Elastic Contribution

The elastic contribution to 'fracture' is easier to understand by considering the Case I described in the previous Chapter, where $\langle\hat{\dot{\gamma}}\rangle\tau_R \simeq 1$ and $\partial T_{xy}/\partial\gamma < 0$ at t_0. The deformation in this regime is sufficiently strong for the chains to suffer significant stretch and the contribution I to Equation (7.9) has become negative. The strain amplitude of $\gamma_0 = 2.5$ imposed in the Case I lies in the region where $d^2\mathcal{F}/d\gamma^2 < 0$ as seen in Figure 7.6. In this regime where the free energy curvature is negative, the system has the possibility to undergo a 'phase separation' of strain but with the total strain conserved [16]. This 'phase separation' of strain will not occur if the separation of timescales between reptation and stretch relaxation is not large enough, and if there are no inhomogeneities in the system.

In the absence of inhomogeneities stress relaxation occurs by stretch relaxation

and reptation. At the end of stretch relaxation, the remaining stress is relaxed by reptation, which causes the tube segments to lose their orientation, and this process occurs uniformly in space. The tube segments gradually become isotropic and the fluid becomes less elastic and more viscous, but with a uniform viscosity in space.

However, in the presence of inhomogeneities the perturbation has a possibility to grow and induce a 'phase separation' of strain if it can compete with the underlying reptation. The initial perturbation which had already grown to some extent at the time of shear cessation at t_0, continues to grow until the end of stretch relaxation. Whether this perturbation will continue to grow after stretch relaxation depends on the amount of reptation which had occurred at the end of stretch relaxation. If the amount of reptation which had occurred at the end of stretch relaxation is small enough, then the system remains unstable to the growing perturbation. This favourable environment allows the perturbation to keep growing and induce a region where the tube segments are still aligned in the flow direction. This situation 'prevents' reptation from relaxing these aligned tube segments along with other tube segments which are already on their way to becoming isotropic. This then creates a situation of non uniform viscosity in the material which then leads to slippage in the bulk of the fluid. This slip which resembles fracture in a solid relaxes most of the stress but comes to an abrupt end as the underlying reptation continues to undermine the instability. The remaining stress is then relaxed by reptation at the end of the internal slip.

The validity of this idea of 'phase separation' of strain comes from the agreement of Figure 7.7 with the criteria given by MG [16] for the occurrence of this phenomenon. The MG theory [16] predicts that the 'phase separation' will occur for strain amplitude $\gamma_0 \gtrsim 2$ and materials of sufficient molecular weight and concentration. This 'phase separation' does not occur for materials whose product of molecular weight and concentration fall below the critical value regardless of

strain amplitude. This is in excellent agreement with Figure 7.7(a) which shows a left cut-off of $\gamma_0 \simeq 2$ and a lower cut-off for Z. This lower cut-off for Z agrees with the MG theory since Z is proportional to the product of concentration and molecular weight. The MG theory also states that in cases where $\mu \neq 1$ a second region of stability is created at large strains, so that this 'phase separation' is not possible at large strain amplitudes. This causes the right cut-off in γ_0 seen in Figure 7.7(a). It is also responsible for the negligible 'induction time' at $\gamma_0 = 4.5$ seen in Figure 7.7(b). The experimental investigation by Morrison and Larson [19] to check the correctness of the MG theory involved using polystyrene solutions with bi-disperse distribution of molecular weights, with the short chains acting as solvent for the long chains. As more short chains are added to the mixture, the amount of reptation which occurs after stretch relaxation increases and hence μ decreases. Morrison and Larson [19] found qualitative agreement with the MG theory for materials whose number of chain entanglements $M_w/M_e > 60$. The agreement came from the fact that as the fraction of short chain polymers in the mixture is increased, the type C 'anomaly' first disappears at large imposed strains. The type C 'anomaly' eventually disappears at strains of around 2 as the short chain fraction is increased as predicted by the MG theory. However, the fraction of short chains required to remove the type C 'anomaly' was higher than the MG predicted value of about 0.1 [19]. The number $M_w/M_e > 60$ is close to the lower cut-off for Z in Figure 7.7(a). Also, the left cut-off for strain in Figure 7.7(a) is close to 2.

7.10.2 Viscous Contribution

The discussion in the previous Subsection described the role of the elastic instability which sets in when Equation (7.7) is satisfied. However, since real step strain experiments are not ideal, then the criterion given in Equation (7.7) is not sufficient to describe the instabilities that arise during startup. The viscous contribution

allows instability to arise before the stress overshoot is reached when Equation 7.6 is satisfied [18].

The viscous contribution to the instability is clearly seen in the behaviour of the eigenvalues, which shows that the fluid goes unstable before the critical strain of $\gamma_0 \approx 2$. However, the growth rate of the instability due to viscous effects increases with the applied shear rate as seen in the Case II of the previous chapter which gives a stronger 'fracture' compared with the Case III which only gives a weak 'fracture'. This is because the growth rate of the instability ω_{max} is nearly one order of magnitude higher for case II than Case III at the time of shear cessation t_0, as seen in Figure 7.16(bc).

Although the applied shear rate of $\langle\widehat{\dot{\gamma}}\rangle = 900$ for Case II lies outside the regime where Equation (7.6) is satisfied. The strain amplitude of $\gamma_0 = 2.5$ lies in the intermediate region where the fluid is unstable as seen in Figures 7.14(c) and 7.16(b). This allows the 'fracture' phenomenon to be realised in this Case where $\gamma_0 = 2.5 < \gamma^{ov} \approx 4.2$. Also, the applied shear rate satisfies $\langle\widehat{\dot{\gamma}}\rangle\tau_R > 1$ for this Case. Thus there is a combination of both viscous and elastic effects which give rise to 'fracture' in this Case, but the boundary between them is not clear.

7.11 Remarks

The foregoing discussion shows the important role played by spatial inhomogeneities in inducing this 'fracture' phenomenon. The experimental data in [4] suggest that 'fracture' is more robust than what the current calculations show, and this could be because the perturbations were only used to initialise the system. No attempt has been made to include a time dependent perturbation as this will be more involved, but this may increase the percentage of 'fracture' seen in the simulations.

This discussion will now conclude with a quick summary of the key results from the current study, and a review of outstanding issues which future workers

in this field may find interesting to examine. Also, a quick summary of assumptions/approximations made during the calculations shall be given.

Chapter 8

Discussions

This treatise will now conclude with a brief discussion of the key findings during the study. This will be followed by a brief outline of some outstanding issues related to the current work. Finally, there will be a quick outline of approximations/assumptions made during the current work.

8.1 Summary of Key Findings

One of the motivations for this work as discussed in Chapter 1 was to determine if new physics was necessary to demonstrate the experimental data outlined in Chapter 3. The Calculations presented in this thesis give excellent qualitative and close quantitative match to the experimental data as outlined below:

I The range of Z (number of entanglements per chain) within which 'fracture' occurs in Figure 6.12 lies in the range of Z (53 - 160) reported in [4]. Also, the values of γ_0 (strain amplitude) in Figure 6.12 are close to the applied strains in Figures 6.2(b), 6.3, 6.8(b) and 6.9(b).

II The calculated velocity profiles during 'fracture' in Figures 6.2(a) and 6.9(a) show very good qualitative match with the experimentally determined velocity profiles in Figures 6.2(b) and 6.9(b).

III Similarly, the calculated shear stresses in Figures 6.6(a), 6.8(a) and 6.10(a) show very good qualitative match with the experimentally determined shear stresses in Figures 6.6(b), 6.8(b) and 6.10(b).

IV The velocity profiles just before shear cessation in the inset of Figure 6.2(a) appears to be homogeneous. This agrees with the experimental data of the inset of Figure 6.3 where the velocity profile appears homogeneous just before shear cessation.

V The calculations show that the 'fracture' phenomenon is not realisable when the strain amplitude is insufficient as in Figure 6.6(a). This agrees with the experimental data of Figures 6.6(b) and 6.8(b).

VI The calculated data shows that the 'induction time' before 'fracture' decreases as Z increases as seen in Figure 6.15(a) in agreement with the inset of Figure 6.15(b).

VII The calculations in Figure 6.16(a) show that the 'fracture' phenomenon is not realisable when the strain amplitude takes the shear stress further beyond the overshoot. This agrees with the experimental data of Figure 6.16(b).

VIII The 'failure planes' in the 'fracture' profiles indicated by the dashed circles in Figures 7.1, 7.2 and 7.5 occur in different locations in the gap between the two plates, but the stress relaxation profiles are always similar to the blue circles in Figure 6.6(a). This agrees with the report in [4] that the stress relaxation profiles are always similar to the green squares in Figure 6.6(b) regardless of the location of the 'failure plane' in different runs of the experiment.

The overwhelming evidence outlined above clearly shows that the 'fracture' phenomenon **does not require new physics** to be demonstrated. In fact, it is actually the 'Type C' behaviour [15, 19] which has since been known to the

community. The association of 'Type C' behaviour to this 'fracture' phenomenon is clearly supported by Figure 6.14. Further support is given by the agreement of Figure 6.12(b) with the MG theory [16] to explain the 'Type C' behaviour. The MG theory predicts a lower cut-off for Z and a bound for γ_0 for which 'Type C' behaviour is realisable.

However, the current theoretical model shows a discrepancy with the experimental data as seen in Figure 6.19. The reason for this discrepancy is not clear at this stage. Also, the theoretical model does not give an exact quantitative match to the experimental data. The theoretical model will require some refinements in order to give an exact quantitative match with the experimental data. The exact nature of these refinements is not clear at this stage.

The MG theory and linear stability analysis outlined in Chapter 7 show that the 'fracture' phenomenon is due to the unstable nature of the fluid when it is put in some flow regime. This instability allows fluctuations in the material to grow and induce 'strain localisation' in the bulk. This then leads to slippage in the bulk of the material which resembles a solid undergoing fracture.

8.2 Further Considerations

A quick discussion of issues related to the current work now follows.

8.2.1 Stress Maximum?

There has been lots of controversy surrounding the existence of the stress maximum predicted by the DE theory. Early experiments [31] suggested the stress maximum did not exist. The existence of a stress maximum can be inferred from a plot of steady state viscosity versus shear rate. The steady state viscosity is defined as

$$\eta(\dot{\gamma}) = \frac{\sigma_{xy}}{\dot{\gamma}}, \tag{8.1}$$

where σ_{xy} is the steady state total shear stress. If the shear stress forms a plateau as in the region between $\dot{\gamma}_1$ and $\dot{\gamma}_2$ in Figure 8.1(a), then the total shear stress is a constant value σ_{pl} in this region as in Figure 8.1(a). Then Equation (8.1) becomes

$$\eta(\dot{\gamma}) = \frac{\sigma_{pl}}{\dot{\gamma}}. \tag{8.2}$$

In this case, the occurrence of a slope of -1 in a plot of $\eta(\dot{\gamma})$ versus $\dot{\gamma}$ on a logarithmic scale will indicate a plateau stress. However, if the total shear stress is increasing slowly with shear rate as shown by the dashed dotted line in Figure 8.1(a), then it will increase with some power law as

$$\sigma_{xy} = \widetilde{\sigma}\dot{\gamma}^{\varphi}, \tag{8.3}$$

where $\widetilde{\sigma}$ is a constant and φ is a positive exponent. In this case, Equation (8.1) becomes

$$\eta(\dot{\gamma}) = \widetilde{\sigma}\dot{\gamma}^{-(1-\varphi)}. \tag{8.4}$$

Hence, a slope of $-(1-\varphi) > -1$ on a plot of $\eta(\dot{\gamma})$ versus $\dot{\gamma}$ on a logarithmic scale will indicate a slowly increasing steady state shear stress with shear rate. This is the situation shown in Figure 8.1(b) which has a slope ≈ -0.7.

The situation shown in Figure 8.1(b) led theorists [32, 33, 34] working with tube based models to incorporate the mechanisms of convective constraint release and chain stretch (which were acknowledged but ignored in the original tube model) into the tube model. These mechanisms removed the 'anomaly' of stress maximum from the tube model, giving a better match for the experimentally measured shear stress [34].

The observation of shear banding [24, 27, 30] in polymer solutions led Hu *et al.* [64] to question the monotonicity of the constitutive relation for entangled polymers. Moreover, the Marrucci Grizzuti (MG) [16] explanation for the Type C

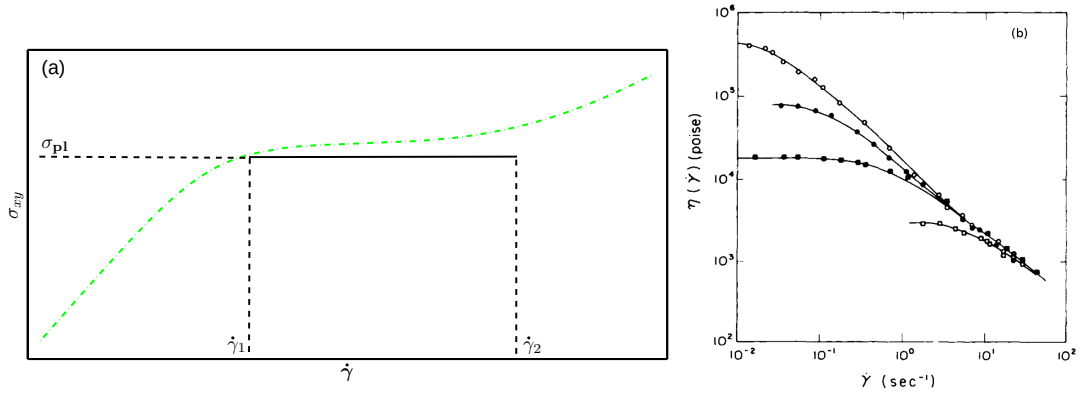

Figure 8.1: (a) Cartoon of total shear stress as a function of shear rate showing two possible behaviours. (b) Steady state viscosity versus shear rate for linear polybutadiene samples of different molecular weights. Open squares: 200,000 g mol^{-1}, filled squares: 350,000 g mol^{-1}, filled circles: 517,000 g mol^{-1} and open circles: 813,000 g mol^{-1}. Figure from [31].

'anomaly' is based on the existence of this stress maximum. The current work on 'fracture' also depends on the nonmonotonicity of the constitutive relation for polymers, which gives striking qualitative and close quantitative agreement with the experiments of [4]. This then reinforces the original question by Hu *et al.* [64], **is the constitutive relation for entangled polymers monotonic?**

The stress maximum may not be directly observable in an experiment, but its signatures of shear banding and fracture-like behaviour can be clearly observed. Doi and Edwards pointed out that the stress maximum may disappear if τ_R and τ_d are not well separated [13]. This factor seems to be at play in this 'fracture' phenomenon which disappears at low Z. A seemingly related observation has been made in shear banding experiments with polymer solutions. In their experiments with polybutadiene solutions under steady shear, Ravindranath *et al.* [30] found steady state shear banding only for solutions with $Z \geq 40$ [30].

Despite the strong indications for nonmonotonicity of the constitutive relation for entangled polymers, there is an alternative view that the shear banding phenomenon is actually due to a breakdown of the entanglement network [1, 55, 65] of the polymer solutions during strong flows. The observation of this fracture-like

behaviour [4, 39] was supposed to confirm the idea of a 'cohesive failure' of the entanglement network. This phenomenon of a 'cohesive failure' is said to occur when the 'retractive forces' in the chains exceed their 'cohesive forces' [3]. The subsequent proposal that the fluid remains in a state of inhomogeneous shear to prevent further loss of entanglements during shear banding [30], suggests that this 'cohesive failure' may be restricted to a narrow region in the material. If the 'cohesive failure' is restricted to a narrow region in the material, then it does not necessarily contradict the tube theory. There is a possibility that some entanglements could be lost as the chains get aligned in the flow direction. If this is the case, then the loss of entanglements should not be so severe as to render the continuum picture of the tube model invalid.

This is reinforced by Figure 6.13(b) which shows that the 'fracture' width δx lies in the range $0.02 \lesssim \delta x \lesssim 0.06$. For a gap of 1 mm, this corresponds to $20\mu\text{m} \lesssim \delta x \lesssim 60\mu\text{m}$ which is much larger than the tube diameter $a \simeq 3 - 4\text{nm}$ and also consistent with the width $\leq 40\mu\text{m}$ reported in [4]. The fact that δx is much larger than the tube diameter indicates that the 'fracture' layer contains a significant number of tube entanglements which fits the picture of strong alignment of tube segments in the flow direction during 'fracture' as discussed earlier in this thesis. If there was a complete loss of entanglements, then it will be out of place for the 'fracture' width to exceed the tube diameter. It is left for experimentalists to come up with new data at finer spatial resolution to determine whether the 'fracture' width is smaller than the tube diameter.

8.2.2 Hydrodynamic Boundary Condition (HBC)

In all the calculations presented so far the zero slip boundary condition was imposed on the fluid velocity and a corresponding zero gradient boundary condition on the polymer stress, following Experiment I discussed in Section 3.2. The 'fracture'

phenomenon discussed here is only a part of a more general set of problems reported in different experiments all involving either wall slip or bulk slip or both [4, 1, 66]. In the case of 'fracture', this slip (bulk slip in this case) is accompanied by an unusual (or abnormal) fast stress relaxation, but this is not always present [4, 1, 66]. The key experimental findings can be grouped broadly into the following two categories: No wall Slip HBC and Wall Slip HBC.

Case I: No Wall Slip HBC

The key experiments demonstrating the behaviour of highly entangled polymeric liquids under this HBC have been described in Section 3.2. During the course of this discussion, it has been shown that the fracture-like behaviour exhibited by these liquids under strong deformation is a consequence of their unstable nature. This instability allows inhomogeneities in the material to grow when the chains are sufficiently entangled and the strain amplitude is sufficient. The growing instability then induces nonuniform viscosities in the material which leads to an internal or bulk slip. This fracture-like behaviour had been interpreted to be due to a 'cohesive failure' of the entanglement network [4], but the current calculations suggest that such a process, if present, is not dominant. It is now left for future workers in this field to examine the possible role of wall slip in changing the relaxation behaviours of these highly entangled polymeric liquids under strong deformation. One of the key experiments related to wall slip and fracture-like behaviour is discussed in the next Subsection.

Case II: Wall Slip HBC

In their experiments with polystyrene solutions, Archer *et al.* [66] reported a 'delayed slip' phenomenon with an associated 'kink' in the shear stress. The material was placed between two flat glass plates with the upper plate moving and the lower plate stationary, and the displacement of tracked 1.5μm diameter spherical

particles dispersed in the polystyrene solution was measured.

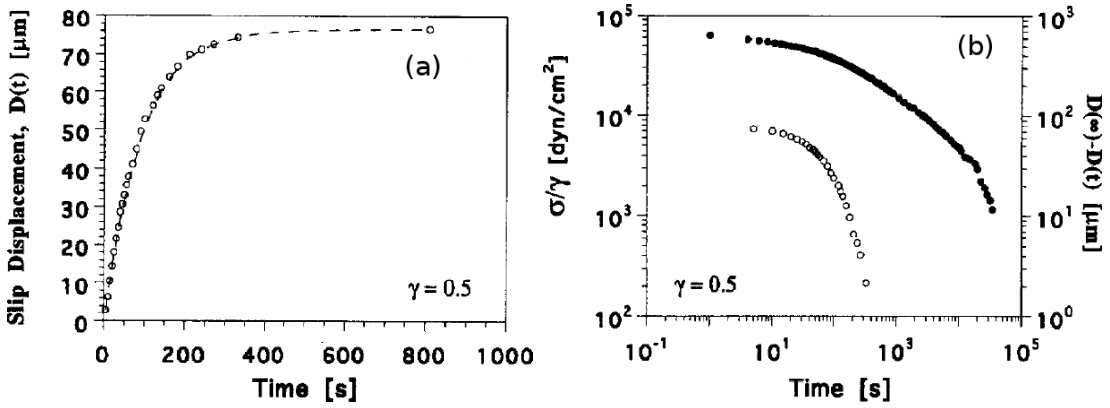

Figure 8.2: (a) Displacement of tracked particles dispersed in a polystyrene solution after shear cessation for strain amplitude $\gamma = 0.5$. (b) Shear stress relaxation (filled symbols) and particle displacement in form of a 'relaxation' (open symbols) after shear cessation for $\gamma = 0.5$. Figures from [66].

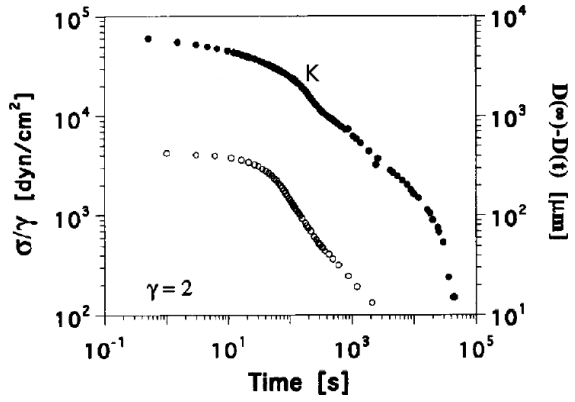

Figure 8.3: Similar to Figure 8.2(b) for $\gamma = 2$. Figure from [66].

They observed that after shear cessation, particles near the upper glass plate 'recoiled' in a direction opposite the prior movement of the plate. Similarly, particles near the stationary lower plate were also displaced by the same amount but in the opposite direction [66]. For strains $\gamma < 5$ most of the particle displacement was restricted to within 1μm from the plates, with particles in the center plane remaining nearly stationary. The displacement of particles at long times after shear cessation $D(\infty) \leq 100\mu$m for $\gamma < 2$, but exceeded 400μm for $\gamma \geq 2$. The time evolution of particle displacement $D(t)$ for $\gamma = 0.5$ is shown in Figure 8.2(a), while

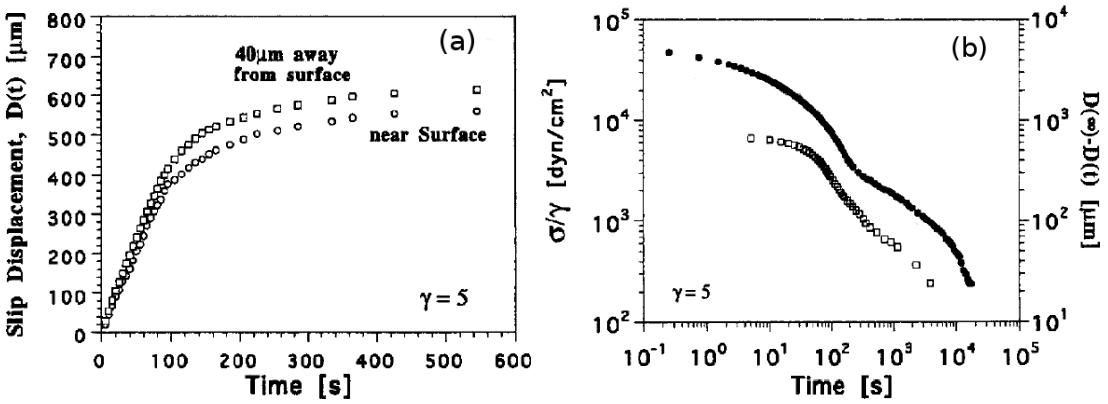

Figure 8.4: (a) Similar to Figure 8.2(a) but with displacements near the surface of the initially moving wall and 40μm away from it for $\gamma = 5$. (b)Similar to Figure 8.2(b) for $\gamma = 5$. Figures from [66].

the filled symbols in Figure 8.2(b) show the relaxation modulus for this strain amplitude. The open symbols in Figure 8.2(b) are the particle displacements represented as a form of 'relaxation' $D(\infty) - D(t)$. The relaxation modulus shown in Figure 8.2(b) shows a nearly uniform slope in time even with the associated particle displacement near the glass surfaces. This 'apparent slip' [66] of particles at about 1μm from the glass surfaces will be referred to as wall slip for the purpose of this discussion.

However, the relaxation modulus shows a sudden change in slope at intermediate times as the strain amplitude is increased to 2. This region where the sudden change of slope occurs which is referred to as a 'kink' [66] is indicated as K in Figure 8.3. The occurrence of this 'kink' is associated with an increase in $D(\infty)$ which then exceeds 400μm. As the strain amplitude increases to 5, significant particle displacement at about 40μm from the glass plates accompany the particle displacement near the plates at about 1μm. Figure 8.4(a) shows that initially after shear cessation at $\gamma = 5$, the particle displacement at 1μm from the glass surface (1μm particles) was nearly the same as that of particle displacement at 40μm away from the surface (40μm particles). However, at about 100 s after shear cessation, the 40μm particles begin to exhibit a much larger displacement than the 1μm par-

ticles. The shear modulus also develops a 'kink' at about this time of 100 s as shown by the filled symbols in Figure 8.4(b). The open symbols in Figure 8.4(b) is the quantity $D(\infty) - D(t)$. Ultimately, the 40μm particles suffer the greatest displacement. This time delay before the 40μm particles show a sudden increase in displacement was described as a 'delayed slip' in [66].

This 'delayed slip' phenomenon bears some resemblance to the facture-like behaviour observed in Case I of no wall slip HBC. The delay before the 40μm particles begin to show a sudden increase in displacement is similar to the delay before the fast stress relaxation occurs in Case I which is accompanied by particle displacement in the bulk of the material. Similarly, there is always a fast stress relaxation (indicated by the 'kink' in the relaxation modulus) whenever strain amplitude is sufficient. However, this fast stress relaxation is not observed at low strain amplitudes even with particle displacement near the wall.

There have been similar reports with polybutadiene [1, 49] solutions, where different degrees of particle displacement in the bulk or near the plates produce different stress relaxation behaviours. Then it becomes necessary for future workers in this field to examine how the position and degree of particle displacement affect the stress relaxation behaviour.

8.2.3 State of Chain Entanglement

One way to address the issue of a possible 'cohesive failure' in the entanglement network during strong deformations is for future workers in this field to do a direct visualization of the entanglement network. This will allow the state of chain entanglements during shear banding and fracture-like bulk slip to be determined. This can be achieved by means of coarse-grained molecular dynamics (MD) simulations. It has recently been shown that coarse-grained simulations are capable of capturing the shear banding phenomenon with just a few entanglements [67]. Hence it may

be possible to capture these different 'fracture' phenomena with sufficient number of entanglements and appropriate HBC.

8.2.4 Non Bonded Interactions

In the DE theory and subsequent modifications of it, the polymer stress is calculated solely from bonded interactions along the chain backbone. That is, the stress is assumed to come from the covalent bonds linking the monomers and these bonds are treated more or less like elastic springs. However, DE introduced Equation (4.2) ($\mathbf{T} = \boldsymbol{\sigma} + \eta(\boldsymbol{\kappa} + \boldsymbol{\kappa}^T) - p\boldsymbol{\delta}$) to describe the total stress in a polymer solution as being the contribution from the polymer and its solvent. The contributions from the polymer is due to bonded interactions along the chain backbone, while the contribution from the solvent is due to momentum transfer from inter molecular collisions. For highly concentrated solutions, DE assumed that the 'Newtonian' contribution becomes negligible and the total stress comes solely from the polymer. However, some workers have shown from Molecular dynamics simulations [41, 68] that the non bonded interactions dominate the total stress at very high shear rates. Although it is not certain what form this 'Newtonian' contribution should take. Adams et al. [26] in their study using the Rolie-Poly model showed that the 'Newtonian' term in Equation (4.2) was suitable for capturing the behaviour of the shear stress at very high shear rates. Hence Equation (4.2) is not only suitable for dilute solutions, but can also be used for concentrated solutions and melts. This approach of adding a 'Newtonian' term to the polymer contribution to make up the total stress has been applied in the calculations presented in this thesis. However, the issue of the exact form of these non bonded interactions is yet to be addressed.

8.3 Approximations/Assumptions

The calculations presented in this thesis made use of a number of assumptions/approximations which are enumerated below:

Continuum Approximation:– While it is appropriate to model polymeric liquids by the continuum hypothesis when the chains are uniformly distributed, it becomes a bit strained if there is 'massive loss of chain entanglements' as claimed in [4], and it occurs at the continuum level. However, the data in [4] shows that the 'fracture' layer contains significant tube segments, so that the application of the continuum hypothesis is consistent with the data so far.

Non Bonded Interactions:– Equation (4.2) used a 'Newtonian stress' to approximate the fast modes in polymeric liquids at high shear rates. While the exact form of these fast modes is not known at the moment, it has been shown in [26] that this treatment is a good approximation.

Constant Chain Entanglements:– This 'fracture' phenomenon suggests that the number of chain entanglements may not be uniform in space. But to a first approximation, the number of chain entanglements has been treated as a constant in the calculations presented here. This approach has been able to capture the key features of the relevant experiments. Even if the number of chain entanglements is not uniform in space, its average value should not change so much. Besides, the manner in which chain entanglements change during strong flows is not fully understood at the moment. In a recent calculation [69], three different assumptions where made about the state of chain entanglements, but the rheological response was the same qualitatively.

Zero Inertia:– The calculations presented here have been made in the zero inertia limit. This is appropriate since the polymeric liquids under consideration are sluggish with inertia playing a very little role in their dynamics. The inertia term in Equation (4.1) is of the order 10^{-10} which is negligible.

References

[1] Sham Ravindranath and Shi-Qing Wang. What are the origins of stress relaxation behaviors in step shear of entangled polymer solutions? *Macromolecules*, 40:8031–8039, 2007.

[2] P. E. Boukany and S. Wang. Exploring origins of interfacial yielding and wall slip in entangled linear melts during shear or after shear cessation. *Macromolecules*, 42:2222–2228, 2009.

[3] S. Wang, S. Ravindranath, Y. Wang, and P. Boukany. New theoretical considerations in polymer rheology: Elastic breakdown of chain entanglement network. *J. Chem. Phys.*, 127:064903, 2007.

[4] Pouyan E. Boukany, Shi-Qing Wang, and Xiaorong Wang. Step shear of entangled linear polymer melts: New experimental evidence for elastic yielding. *Macromolecules*, 42:6261–6269, 2009.

[5] M. Doi and S. F. Edwards. *The Theory of Polymer Dynamics*. Oxford University Press, New York, United States, 1986.

[6] G. K. Batchelor. *An Introduction to Fluid Dynamics*. Cambridge University Press, Edinburgh, United Kingdom, 1967.

[7] R. G. Larson. *Constitutive equations for polymer melts and solutions*. AT & T Bell Laboratories, Incorporated, United States, 1988.

[8] R. B. Bird, R. C. Armstrong, and O. Hassager. *Dynamics of Polymeric Liquids, Fluid Mechanics Vol. 1.* John Wiley & Sons, Inc., New York, United States, 1987.

[9] M. Doi and S. F. Edwards. Dynamics of concentrated polymer systems. part 1.-brownian motion in the equilibrium state. *J. Chem. Soc., Faraday Trans. 2*, 74:1789–1801, 1978.

[10] P. G. DE GENNES. Reptation of a polymer chain in the presence of fixed obstacles. *J. Chem. Phys.*, 55(2):572–579, 1971.

[11] M. Doi and S. F. Edwards. Dynamics of concentrated polymer systems. part 2.-molecular motion under flow. *J. Chem. Soc., Faraday Trans. 2*, 74:1802–1817, 1978.

[12] M. Doi and S. F. Edwards. Dynamics of concentrated polymer systems. part 3.-the constitutive equation. *J. Chem. Soc., Faraday Trans. 2*, 74:1818–1832, 1978.

[13] M. Doi and S. F. Edwards. Dynamics of concentrated polymer systems. part4-rheological properties. *J. Chem. Soc., Faraday Trans. 2*, 75:38–54, 1979.

[14] K. Osaki, K. Nishizawa, and M. Kurata. Material time constant characterizing the nonlinear viscoelasticity of entangled polymeric systems. *Macromolecules*, 15:1068–1071, 1982.

[15] K. Osaki. On the damping function of shear relaxation modulus for entangled polymers. *Rheol. Acta*, 32:429–437, 1993.

[16] G. Marrucci and N. Grizzuti. The free energy function of the doi-edwards theory: Analysis of the instabilities in stress relaxation. *J. Rheol.*, 27(5):433–450, 1983.

[17] Richard A. L. Jones. *Soft Condensed Matter*. Oxford University Press, Oxford, United Kingdom, 2002.

[18] R. L. Moorcroft and S. M. Fielding. Criteria for shear banding in time-dependent flow of complex fluids. arXiv1201.6259, 2012.

[19] F. A. Morrison and R. G. Larson. A study of shear-stress relaxation anomalies in binary mixtures of monodisperse polystyrenes. *J. Polym. Sci.: B*, 30:943–950, 1992.

[20] P. Español, X. F. Yuan, and R. C. Ball. Shear banding flow in the Johnson-Segalman fluid. *J. Non-Newt. Fl. Mech.*, 65:93–109, 1996.

[21] F. Greco and R. C. Ball. Shear band formation in a non-Newtonian fluid model with a constitutive instability. *J. Non-Newt. Fl. Mech.*, 69:195–206, 1997.

[22] Peter D. Olmsted. Perspectives on shear banding in complex fluids. *Rheol. Acta*, 47:283–300, 2008.

[23] J. M. Adams, S. M. Fielding, and P. D. Olmsted. The interplay between boundary conditons and flow geometries in shear banding: Hysteresis, band configurations, and surface transitions. *J. Non-Newt. Fl. Mech.*, 151:101–118, 2008.

[24] Y. T. Hu. Steady-state shear banding in entangled polymers? *J. Rheol.*, 54(6):1307–1323, 2010.

[25] J. M. Adams and P. D. Olmsted. Non monotonic models are not necessary to obtain shear banding phenomena in entangled polymer solutions. *Phys. Rev. Lett.*, 102:067801, 2009.

[26] J. M. Adams, S. M. Fielding, and P. D. Olmsted. Transient shear banding in entangled polymers: A study using the rolie-poly model. *J. Rheol.*, 55(5):1007, 2011.

[27] P. Tapadia, S. Ravindranath, and S. Wang. Banding in entangled polymer fluids under oscillatory shearing. *Phys. Rev. Lett.*, 96:196001, 2006.

[28] Y. T. Hu and A. Lips. Kinetics and mechanism of shear banding in an enatngled micellar solution. *J. Rheol.*, 49(5):1001–1027, 2005.

[29] P. E. Boukany and S. Wang. A correlation between velocity profile and molecular weight distribution in sheared entangled polymer solutions. *J. Rheol.*, 51(2):217–233, 2007.

[30] S. Ravindranath, S. Wang, M. Olechnowicz, and R. Quirk. Banding in simple steady shear of entangled polymer solutions. *Macromolecules*, 41:2663–2670, 2008.

[31] E. V. Menezes and W. W. Graessley. Nonlinear rheological behavior of polymer systems for several shear-flow histories. *J. Polym. Sci.: B*, 20:1817–1833, 1982.

[32] G. Ianniruberto and G. Marrucci. Convective orientational renewal in entangled polymers. *J. Non-Newtonian Fluid Mech.*, 95:363–374, 2000.

[33] S. T. Milner, T. C. B. McLeish, and A. E. Likhtman. Microscopic theory of convective constraint release. *J. Rheol.*, 45(2):539–563, 2001.

[34] R. S. Graham, A. E. Likhtman, T. C. B. McLeish, and S. T. Milner. Microscopic theory of linear, entangled polymer chains under rapid deformation including chain stretch and convective constraint release. *J. Rheol.*, 47:1171–1200, 2003.

[35] Y. T. Hu, P. Boltenhagen, Eric Matthys, and D. J. Pine. Shear thickening in low-concentration solutions of wormlike micelles. I. direct visualization of transient behavior and phase transitions. *J. Rheol.*, 42(5):1185–1208, 1998.

[36] Shi-Qing Wang. Molecular transitions and dynamics at polymer/wall interfaces: Origins of flow instabilities and wall slip. *Advances in Polymer Science*, 138:227–275, 1999.

[37] F. Brochardt and P. G. de Gennes. Shear-dependent slippage at a polymer/solid interface. *Langmuir*, 8:3033–3037, 1992.

[38] Shi-Qing Wang and Patrick Drda. Molecular instabilities in capillary flow of polymer melts: interfacial stick-slip transition, wall slip and extrudate distortion. *Macromol. Chem. Phys.*, 198:673–701, 1997.

[39] Xin Li and Shi-Qing Wang. Elastic yielding after step shear and during laos in the absence of meniscus failure. *Rheol Acta*, 49:985–991, 2010.

[40] Yuye Fang, Guanglin Wang, Nan Tian, Xiao Wang, Xiangyang Zhu, Panpan Lin, Guanglei Ma, and Liangbin Li. Shear inhomogeneity in poly(ethylene oxide) melts. *J. Rheol.*, 55(5):939–949, 2011.

[41] Alexei E. Likhtman. Whither tube theory: From believing to measuring. *J. Non-Newtonian Fluid Mech.*, 157:158–161, 2009.

[42] A. E. Likhtman and R. S. Graham. Simple constitutive equation for linear polymer melts derived from molecular theory: Rolie-poly equation. *J. Non-Newt. Fl. Mech.*, 114:1–12, 2003.

[43] Ronald G. Larson. *The Structure and Rheology of Complex Fluids*. Oxford University Press, New York, United States, 1999.

[44] C-Y. David Lu, Peter D. Olmsted, and R. C. Ball. Effects of nonlocal stress on the determination of shear banding flow. *Phys. Rev. Lett.*, 84(4):642–645, 2000.

[45] P. D. Olmsted and O. Radulescu. Johnson-Segalman model with a diffusion term in cylindrical Cuoette flow. *J. Rheol.*, 44:257–275, 2000.

[46] Ardith W. El-Kareh and L. Gary Leal. Existence of solutions for all deborah numbers for a non-newtonian model modified to include diffusion. *J. Non-Newt. Fl. Mech.*, 33:257–287, 1989.

[47] M. W. Johnson and D. Segalman. A model for viscoelastic fluid behaviour which allows non affine deformation. *J. Non-Newt. Fl. Mech.*, 2:255–270, 1977.

[48] L. J. Fetters, D . J. Lohse, D. Richter, T . A. Witten, and A. Zirkel. Connection between polymer molecular weight, density, chain dimensions, and melt viscoelastic properties. *Macromolecules*, 27(17):4639–4647, 1994.

[49] Sham Ravindranath, Shi-Qing Wang, M. Olechnowicz, V. S. Chavan, and R. P. Quirk. How polymeric solvents control shear inhomogeneity in large deformations of entangled mixtures. *Rheol Acta*, 50:97–105, 2011.

[50] C. Grand, J. Arrault, and M.E. Cates. Slow transients and metastability in wormlike micelle rheology. *J. Phys. II France*, 7:1071–1086, 1997.

[51] J. Bent, L. R. Hutchings, R. W. Richards, T. Gough, R. Spares, P. D. Coates, I. Grillo, O. G. Harlen, D. J. Read, R. S. Graham, A. E. Likhtman, D. J. Groves, T. M. Nicholson, and T. C. B. McLeish. Neutron-mapping polymer flow: Scattering, flow visualization, and molecular theory. *SCIENCE*, 301:1691, 2003.

[52] M. A. Noor and M. Waseem. Some iterative methods for solving a system of nonlinear equations. *Computers and Mathematics with Applications*, 57:101–106, 2009.

[53] R. J. Leveque. *Finite Difference Methods for Ordinary and Partial Differential Equations: Steady-State and Time Dependent Problems*. The Society for Industrial and Applied Mathematics, Philadelphia, United States, 2007.

[54] Leon Lapidus and George F. Pinder. *Numerical Solution of Partial Differential Equations in Science and Engineering*. John Wiley & Sons, Inc., New York, United States, 1999.

[55] P. Tapadia and S. Wang. Yieldlike constitutive transition in shear flow of entangled polymeric fluids. *Phys. Rev. Lett.*, 91(19):198301, 2003.

[56] advanced research computing (arc) infrastructure of the university of leeds. https://hec.wiki.leeds.ac.uk/bin/view/Documentation/ArcOne.

[57] O. S. Agimelen and P. D. Olmsted. Apparent fracture in polymeric fluids under step shear. arXiv:1204.4169v2, 2012.

[58] S. M. Fielding and P. D. Olmsted. Early stage kinetics in a unified model of shear-induced demixing and mechanical shear banding instabilities. *Phys. Rev. Lett.*, 90(22):224501, 2003.

[59] S. M. Fielding and P. D. Olmsted. Kinetics of the shear banding instability in startup flows. *Phys. Rev. E*, 68:036313, 2003.

[60] D. W. Mead and R. G. Larson. A molecular theory for fast of entangled polymers. *Macromolecules*, 31:7895–7914, 1998.

[61] R. L. Moorcroft, M. E. Cates, and S. M. Fielding. Age-dependent transient shear banding in soft glasses. *Phys. Rev. Lett.*, 106:055502, 2011.

[62] Granino A. Korn and Theresa M. Korn. *Mathematical Handbook for Scientists and Engineers*. McGraw-Hill, Inc., United States, 1961.

[63] Dennis G. Zill. *A First Course in Differential Equations with Applications, Fourth Edition*. PWS-KENT Publishing Company, Boston, United States, 1989.

[64] Y. Thomas Hu, Larry Wilen, Amy Philips, and Alex Lips. Is the constitutive relation for entangled polymers monotonic? *J. Rheol.*, 51(2):275–295, 2007.

[65] Y. Wang and S. Wang. Exploring stress overshoot phenomenon upon startup deformation of entangled linear polymeric liquids. *J. Rheol.*, 53(6):1389–1401, 2009.

[66] L. A. Archer, Y.-L. Chen, and R. G. Larson. Delayed slip after step strains in highly entangled polystyrene solutions. *J. Rheol.*, 39(3):519–525, 1995.

[67] Jing Cao and Alexei E. Likhtman. Shear banding in molecular dynamics of polymer melts. *Phys. Rev. Lett.*, 108:028302, 2012.

[68] M. Fixman. Stress relaxation in polymer melts and concentrated solutions. *J. Chem. Phys.*, 95(2):1410–1413, 1991.

[69] Joontaek Park, David W. Mead, and Morton M. Denn. Stochastic simulation of entangled polymeric liquids in fast flows: Microstructure modification. *J. Rheol.*, 56:1057–1081, 2012.